**Carlos Alberto de Oliveira Henriques**

# Study of atomic energy shifts induced by Casimir cavities

Dissertation submitted in partial fulfilment for the degree of Master of Science in Engineering Physics, Faculty of Science and Technology, University of Coimbra in Portugal.

Supervisor:
Doctor Luís Manuel Panchorrinha Fernandes

Co-supervisor:
Doctor Fernando Domingues Amaro

MASTER IN ENGINEERING PHYSICS IN FACULTY OF SCIENCE AND TECHNOLOGY OF UNIVERSITY OF COIMBRA

Coimbra – Portugal
September / 2014

*“Only those who attempt the absurd will achieve the impossible.”*

*Albert Einstein*

# Resumo

A Eletrodinâmica Estocástica (SED) é uma versão moderna da Eletrodinâmica Clássica, cuja principal inovação é a inclusão de um fundo eletromagnético aleatório à temperatura zero. Esta teoria tem descrito alguns fenómenos atómicos, até agora apenas explicados pela Mecânica Quântica. A SED sugere que as energias dos níveis atómicos são pré-determinadas pelo campo de ponto zero (ZPF). Assim, uma vez que as cavidades de Casimir suprimem alguns dos modos do ZPF, os átomos dentro dessas cavidades poderão sofrer desvios energéticos quer no estado fundamental quer no excitado. Desse modo, a comutação de átomos entre o espaço livre e cavidades de Casimir poderá levar à emissão de radiação ou a um ganho em energia nas suas propriedades radiativas. Este excesso de energia é fornecido pelo ZPF, que á saída da cavidade devolve aos átomos o desvio inicialmente sofrido conferindo-lhes as orbitas características do espaço livre. Com base nesta hipótese, começamos a nossa investigação estudando computacionalmente a interação do átomo de Hidrogénico clássico com ZPF, caracteristico do espaço livre e de uma cavidade de Casimir. Para isso, integramos numericamente o movimento do eletrão na sua orbita utilizando um modelo em duas dimensões já documentado, e desenvolvemos nós próprios um modelo em três dimensões. Estimamos também, o desvio do estado fundamental do átomo de Hidrogénio dentro de uma cavidade de Casimir, fazendo para isso uma aproximação ao oscilador harmónico. Feitos estes estudos teóricos e computacionais, propusemos um método experimental para medir o desvio energético nos níveis atómicos de átomos ao passarem por cavidades de Casimir. Projetamos e montamos um sistema experimental que permitiu passar gases através de cavidades de Casimir constituídas por membranas nano-porosas evaporadas com alumínio. O sistema, feito de aço-inox, foi conectado a dois monocromadores que nos permitiram irradiar o gás com uma frequência específica, e também, usando um PMT, fazer uma análise espectroscopia da radiação emitida. De seguida, fizemos uma análise espectroscópica de 150 a 550 nm, registando a radiação emitida por átomos de Xe ao passarem por membranas nano-porosas, onde algumas evidências de radiação foram observadas, no entanto, é necessário um estudo mais cuidadoso no futuro. Por ultimo, também testamos algumas hipóteses alternativas, excitando previamente os átomos de Xe, no entanto, não fomos capazes de distinguir qualquer radiação imitida do ruido de fundo. Concluímos ainda que o sistema não é suficientemente sensível nos comprimentos de onda desejados, maioritariamente devido ao PMT usado. Finalmente, concluímos o nosso trabalho sugerindo algumas melhorias.

# Abstract

Stochastic Electrodynamics (SED) is a modern version of classic electrodynamics whose principal innovation is the inclusion of a random electromagnetic zero-point field background. This theory has described some atomic effects, until now only explained by quantum mechanics. The SED suggests that the atomic level energies are predetermined by the zero-point field (ZPF). Since a Casimir cavity suppresses some ZPF modes, the atoms inside such cavity could undergo level shifts in their ground and exited states. Switching ground or excited atoms between Casimir cavities and the free space can lead to the hypothetical detection of radiation or an energetic gain in their radiative properties. This excess of energy comes from the ZPF which returns the shifted energy of the atomic orbits to the initial values when the atoms return to the free space. Based on this hypothesis, we start our investigation by studding the classic hydrogen atom interaction with the free space and with the ZPF cavity by computational means. We numerically integrate the electron motion in its orbit using an already documented two-dimensional model and developed ourselves a three-dimensional model. We also estimate the shift in the ground state of the hydrogen atom inside a Casimir cavity, approximating it to the harmonic oscillator. After this theoretical and computational evaluation, we propose an experimental method to measure the energy shift in the atomic levels of an atom of gas when flowing through a Casimir cavity. We projected and mounted an experimental apparatus which allows passing gases through Casimir cavities constituted by nano-porous metal coated membranes. The system, made of stainless steel, was connected to two monochromators which allow irradiating the gas with a specific wavelength and making a spectroscopic analysis of the emitted radiation using a Photomultiplier tube. We performed a spectroscopic analysis for wavelengths ranging from 150 to 550 nm, recording the radiation emitted by Xe atoms passing through nano-porous membranes, where some radiation evidences were observed, however a more careful study is required in the future. We also tested some alternative hypothesis, exciting the Xenon atoms, but we could not distinguish the expected radiation emitted from the background noise. We conclude that the system is not sensitive in the required wavelength, mostly due to the PMT used. Finally, we conclude our work suggesting some improvements.

# Acknowledgments

To my supervisor, Dr. Fernando Amaro, who was the responsible for the concretisation of this work. Thank you for all the knowledge, manly in the experimental part, and for the dedication during all the investigation, including in the revision of this document.

To Dr. Joaquim dos Santos, who gave me the opportunity and the means to advance with this investigation. Thank you for all the support, credit, and suggestions in the elaboration of this document.

To my co-supervisor, Dr Luís Fernandes, for the revision of this document.

To all the GIAN team, including the workshop technicians, who warmly receive me, and help me in a variety of questions relative to my investigation. Besides the quality of the investigation developed in this group, I'm grateful by the friendship and cooperation environment.

To Dr. António Paixão, by the help in the initial computational simulations and the availability and use of the electronic microscope.

To Bruno Galhardo, by the help in the computational simulations on the cluster and to the implementation of my code in C++.

To LIP and Dr. Vitaly Tchepel, by the availability of a monochromator. And to Dr. Maria Fraga, by the clarification of some doubts relativity to the atomic transitions.

To Dr. José Lopes, by the availability of a monochromator and some of the vacuum equipment.

To Dr. Francisco Gil, by the clarification of some doubts relativite to the monochromators operation.

To Dr. Thomas Valone who suggested to make an investigation in this area. And to Dr. Garret Moddel who was the first to make a similar investigation and that gave me some helpful initial suggestions.

To Dr. David Rodríguez by the collaboration in the computational investigations and for all the clarifications about the SED.

To Dr. Kaled Dechoum, by the theoretical clarifications relativite to the SED.

To GE Healthcare Life Sciences, for the free supply of the nano-porous membranes.

To my family, friends and girlfriend, for all the support during this investigation.

# List of abbreviations

| | |
|---|---|
| SED | Stochastic Electrodynamics |
| ZPF | Zero-Point Field |
| QM | Quantum Mechanics |
| QED | Quantum Electrodynamics |
| FWHM | Full Width at Half Maximum |
| LAR | Least absolute residuals |
| PMT | Photomultiplier tube |
| MC | Monochromator |
| MCA | Multi-Channel Analyser |
| SEDS | SED which includes the spin |
| $r_b$ | Bohr radius |

# Table of Contents

# 1. Introduction

In the XVII century it was believed that if we extract all the solid material and gases contained in a volume we would have a completely empty space, the vacuum. Over time the vacuum concept changed and, in the XIX century, it was noticed that the thermic radiation would persist. So the vacuum concept got one more requisite, zero temperature, and then the problem was solved. However, in the XX century it was proven theoretical and experimentally that even at zero Kelvin there was still energy. For that reason this energy was named Zero-Point Energy (ZPE). ZPE takes the form of field fluctuations, known Zero-Point Field[1] (ZPF) and could be considered the ground state of the vacuum. Nikola Tesla was likely the first to propose the existence of such kind of energy and the possibility of its use for industrial purposes [1]. After in the end of the XIX century this proposal could seem to be inconsistent, nowadays more and more researches are looking into this possibility.

At the realm of Quantum Mechanics (QM), the ZPF existence is often attributed to the Heisenberg Uncertainty Principle. According to this principle, if we are interested in the measurement of any two conjugate observables (such as the position and the momentum), A and B, they must obey to the commutation relation $[A, B] = i\hbar$ (where $\hbar$ is the reduced Planck's constant). Being $\Delta A$ and $\Delta B$ respectively the A and B observable variances, their uncertainty relation will be $\Delta A \Delta B \geq \hbar/2$. If we measure A with high precision then the measurement of B will be less precise. Thereby there cannot be a state in which the system sits motionless at the bottom of its potential well, for which its position and momentum would both be determined with great precision. Hence the ground state of a system must have a distribution in position and momentum satisfying the uncertainty principle ($\Delta x \Delta p \geq \hbar/2$). This implies that the system must have energy greater than the minimum of the potential well, being this ground state energy the ZPE [2].

In addition to these theoretical predictions of the existence of the ZPF, some experimental evidences, such as the spontaneous emission, the Lamb shift, and the Casimir forces, seem also to be a consequence of the ZPF [3]. For example, the Casimir

---

[1] The term ZPF is related to all the field fluctuations, even with forces other than the electromagnetic. However in this document whenever we refer to the ZPF we are only considering the electromagnetic ZPF since we only deal with electromagnetic forces.

force, which was studied in detail in the last years [4], is often related with the perturbation induced in the ZPF by two conductive parallel plates. According to such scenario, some modes of the ZPF's electromagnetic fluctuations are suppressed by the boundary conditions imposed by the plates, inducing an attractive force between them, due to the difference between the outer and inner electromagnetic pressures. The possibility of extracting energy and heat from the ZPF by means of the Casimir force was theoretically demonstrated, without the violation of any thermodynamic law [5]. However, a symmetric attractive force between two objects cannot be used to continually extract ZPF energy since the same amount of energy is needed to separate again the objects. For now it is pure speculation the existence of a functional method to use this energy in a recycling cycle.

Early in the last century, personalities such as Einstein and Planck made efforts to study the interaction between the electromagnetic oscillator and the radiation. However, over the years the attentions were diverted to QM. Still, in the second half of the XX century, the classical treatment was reviewed, at this time including a missing key point in the previous formulations: the existence of a random electromagnetic background identical to MQ's ZPF. This original classical theory is known by Stochastic Electrodynamics (SED) and has solved some atomic problems such as the orbital instability, the particle motion at zero temperature, the Casimir and van der Waals forces, among others [6]. While for QM the ZPF is a derived result, for SED it is a direct consequence of a fundamental assumption. Thus, and mathematically speaking, SED is nothing more than the use of the relativistic version of the motion classic laws (Newton second law) with an electromagnetic random background described by Maxwell's equations.

From the point of view of SED, the electron in a classic orbit around the nucleus radiates (Larmor radiation) constantly, consequence of its self-reaction. However it also absorbs power from the ZPF, being therefore possible that the atom has a stable averaged-orbit. In other words, it is the spectral ZPF's form which determines the ground state energy of the atomic systems (and possibly determines also the energy levels of the excited states too) [7]. Hence, it is reasonable to think that, if we somewhat change the ZPF (for example suppressing some resonant modes using a Casimir cavity[2]), the atoms will undergo a level shift. This is the main idea studied in our work. Based on these level

---

[2] A Casimir cavity is in this document understood as a region in space where the ZPF is modified often by the presence of some kind of conductive boundary, which suppress some ZPF's modes.

shifts, it could be possible to use a method to extract energy from the ZPF in a continuous cycle, as already proposed in other documents [2] [8]. In this work, we propose a more elaborated concept, exploring also the shifts in excited states and their related atomic transitions.

Until now, the reader could still have a fundamental question: “If there is a ZPF, why don’t we detect this radiation?” The answer is simple: if this background is homogeneous, isotropic and is everywhere, even inside our measuring devices, they can’t distinguish this radiation from some internal reference. For example, according to SED all the atoms are constantly radiating Larmor radiation, however we don’t detect this radiation because all the atoms are also absorbing the same radiation and no net energy transference exists across a surface [6].

SED being more intuitive for our purposes than Quantum Electrodynamics[3] (QED), it will be our theoretical basis. Since it is a very immature theory, we were forced to attempt making some theoretical predictions related with our experimental method by means of computational simulation. However, some effects explored in this work can be seen from a QM point of view, usually related to the well-known Casimir-Polder/van der Waals forces (these ones were also successfully explained in the SED framework [9][10]). For a deeper study of this subject, the reader can use the following references: for theoretical and computational studies about atom-surface interaction potential see [11][12][13][14][15][16][17]; for experimental Casimir-Polder/van der Waals forces, measurements and detection of modifications in radiative properties induced by boundary conditions, see [18][19][20][21][22][23][24]; and for some reviews about the Casimir-Polder/van der Waals theory and experiments see [25][26][4].

In the present work, after making a brief review of the literature, we were able to implement some computational methods already documented, replicating the same results. Furthermore, we found some conceptual and computational failures of these methods, never reported until now in the literature (at least from our knowledge). We tried to improve these methods developing, for example, a full 3D computational model of the hydrogen atom in the SED framework. We adapted algorithms already existent and our own algorithms to study the electron behaviour in the hydrogen atom immersed in a modified ZPF, since we cannot find such study in the literature. For the hydrogen atom, approximating it to the harmonic oscillator, we first study its equilibrium radius for the

---

[3] QED treats the electromagnetic ZPF as virtual photons, while in the SED realm these fluctuations are seen as real electromagnetic waves, making this concept more intuitive.

free space by numerical means, obtaining the same result (already documented) as using analytical means. Next, we make the same for a modified ZPF cavity, being possible to confirm the expected equilibrium radius decreasing for smaller cavities. Despite the previous advances (discovers and algorithm improvements which can be used in future works to study new atomic systems) in the literature, we also contribute to science with experimental investigation:

1) we make a qualitative analysis of the radiation emitted from ground-state atoms passing through Casimir cavities for higher energies, in contrast with the quantitative analysis for lower energies already made in the past;
2) we propose and implement experimentally a new concept, which involves the excitation of the previous atoms, to study the radiative shifts in level transitions induced by Casimir cavities.

In chapter 2 we introduce SED with special focus on the Hydrogen atom. In that chapter, we attempt to treat the Hydrogen atom in the SED framework by means of numerical integration using a one-dimensional ZPF. Next, in chapter 3, we discuss the ZPF computational generation methods focusing in a 3D ZPF topology. With this more credible method to generate the ZPF, and using approximations related with the harmonic oscillator, we estimate the averaged ground-state radius variation induced by the immersion of a Hydrogen atom in a modified ZPF cavity. Lastly in chapter 3, we develop and test a 3D model of the Hydrogen atom in the SED realm, using a 3D ZPF. In chapter 4, we schematize a conceptual method to extract energy from the ZPF taking into account the effects studied in the previous chapters. There we make some references to previous works, propose possible improvements and discuss different hypothesis and correspondent application ideas. In the end of the chapter we present some experimental limitations which can influence the theoretical methods. In chapter 5, we propose an experimental apparatus to study the hypothesis presented in the previous chapter. We give some details about the experiment instrumentation and finish the chapter with some simulations of physical effects which take place in the experiment. In chapter 6, we present the experimental results: from the preliminary tests to the main experiment. Finally we discuss the results and suggest future improvements and new experiments.

## 1.1. Objectives

In this work we intend to study the remote possibility of extracting energy from the vacuum. We do not intend to project an industrial system but only to develop an experimental method and apparatus to validate our hypothesis, which have their foundations in SED [6].

We intend to study ground-state shifts in atoms induced by Casimir cavities. For this we will force the flow of gases (monoatomic and polyatomic) through metal-coated membranes with pores of the order of a few tens of nanometres. At the same time, we will make a spectral analysis of the radiation emitted in the UV and part of the visible regions. To study some radiative shifts in atomic transitions, we also intend to excite the gases with UV radiation and analyse the radiation emitted from those that pass through the porous membrane. Lastly we will study the shift in the molecular ground state induced by the Casimir cavity. For this, we intend to dissociate the molecules before they enter the membrane and analyse the radiation emitted by the ones that recombine inside the pores.

## 1.2. Motivation

The conceptual importance of the development of SED is in itself great since this model intends to be a unified theory. It is even more fundamental than QM since SED is a dynamical description of the atomic systems while QM is seen as an averaged description [27][28]. This consequently means also a better understanding of the QM which could lead to advances in technologic areas as quantum computation and superconductive materials, among others.

Despite this, our main motivation is to study the possibility of developing a method to extract energy from an almost inexhaustible source, available everywhere. If we integrate all the ZPF’s modes until the Planck frequency ($10^{43}$ Hz), the computed energy density of the vacuum is in the $10^{113}\ \mathrm{J/m^3}$ order of magnitude, greater than any known energy source and also greater than the actual technological requirements [2].

The rising needs of energy in our society, the ending of the oil reservoirs and the dangers of nuclear power plants may lead to an energetic crisis. It‘s clear the enormous need to study new energy sources capable of satisfying the requirements of future generations.

Even this hypothesis being a remote possibility, the science is made of attempts, with only a small part of them having success. In this case, the risk is justified by the achievement.

## 1.3. State of art

In the literature, scientific works about energy extraction from the ZPF are rare. However we attempted to collect some information about what was done in this area and resume here the most relevant aspects.

An extensive review was made by Valone and published in the book with ref. [1]. This work resumes some of the last attempts to harness the Zero-Point Energy (ZPE), either in theoretical concepts or engineering machines. There are also some references made to SED and the basic concept explored in the present study.

Another review about experimental concepts to extract energy from the ZPF was made in ref. [2]. There we find also some information about the use of gases in Casimir cavities. The main idea is to use the hypothetical ground-state shift (studied in more detail in chapter 3 of the present document) of the atoms when they are inside a cavity. As the ground-state energy level is predetermined by the ZPF, inside a cavity the new ground state of the atom will be different from the one outside and this way it could be possible to collect the corresponding energy difference. An attempt to explore this hypothesis was carried out by Puthoff et al. (2001) but, according to ref. [2], such investigation was not completed. The experimental apparatus allowed passing $H_2$ gas through a 1 $\mu$m Casimir cavity suppressing the frequencies resonant with the ground state molecule vibrations. It was suggested that, in this scenario, the molecule dissociation energy would increase. To prove this hypothesis, the experiment was planned in the Synchrotron Radiation Center at the University of Wisconsin (Madison, USA), where an intense UV beam used to disassociate the gas molecules could be generated. However, a problem with the synchrotron beam made the conclusion of the experiment to be impossible.

In ref. [29], Puthoff et al., in addition to some exotics concepts about a propulsion system to interstellar travels based on ZPF, also mention the shifts in atoms when they are inside a Casimir cavity. They also claim to lead experimental investigations about this subject in their laboratories but without success so far.

More recently, in 2012, an attempt was made to detect radiation from ground-state gases flowing through porous gold-coated membranes (forming the Casimir cavities). This work [8] was not conclusive. However, it presents some interesting results. Because of the importance of this work to our study, we will describe it in detail in section 4.1.1. Related with this last investigation, there is also a patent [30].

# 2. Stochastic electrodynamics

In this chapter, we introduce Stochastic Electrodynamics (SED) with special focus in its description of the Hydrogen atom. Then we describe an algorithm for computational simulation of this system and, finally, we present results of the implementation of this algorithm.

Here, using a method described in the literature for the first time, we computed the orbit radius of the hydrogen atom for longer times and found some inconsistences with the theory.

## 2.1. Introduction to Stochastic Electrodynamics

Stochastic Electrodynamics, also named Random Electrodynamics, is basically a modern extension of the classic electron theory of Lorentz, and also a continuation of the investigations of Einstein, Planck, Nernst and Stern, but with different choices of the boundary conditions and the inclusion of the relativity theory [3].

According to the SED formulation, particles are described classically as point charges interacting with a background of random classical electromagnetic zero-point field[4] (ZPF) with the energy spectrum described in equation (1), equal to the one used in QM [7].

$$\rho(\omega) = \frac{\hbar\omega^3}{2\pi^2 c^3} \tag{1}$$

In equation (1), $\omega$ is the angular frequency[5] of the waves, $c$ the ligth speed in vacuum and $\hbar$ the reduced Planck constant. This particular spectrum (proportional to $\omega^3$) is the only one that is Lorentz invariant [7]. The proportionality constant was calculated from comparison with experiments on the van der Waals forces, yielding an energy per normal mode of $\frac{1}{2}\hbar\omega$. Then $\hbar$ does not have any relation with QM or quantization, it is only a scale factor [3][31]. Consequently, the ZPF waves can be obtained from the Maxwell's equations as a non-zero homogeneous solution.

---

[4] When we refer to ZPF, it is the zero point field at temperature zero, we are not considering thermal radiation effects.

[5] Throughout this document the symbol $\omega$ will be always associated to the angular frequency, the reader shouldn't confuse it with frequency.

Even not comparable with the QED success, SED has solved and predicted several effects before only explained in the QED realm. Some examples are the Casimir and van der Waals forces, the Planck blackbody radiation and the thermal effects of acceleration through the vacuum [7]. SED also produced great results in linear systems such as the harmonic oscillator. Boyer has shown that the moments $\langle x^n \rangle$ of a harmonic oscillator immersed in the ZPF have the same behaviour than the quantum harmonic oscillator in the ground state [32]. That is the same to say that the Heisenberg uncertainty relation is satisfied for the SED harmonic oscillator, being its probability distribution the same than the QM harmonic oscillator in the ground state [32]. This remarkable result suggests that the random character of ZPF leads to the familiar probabilistic behaviour of QM, making SED a good candidate to expand our comprehension of the nature fundamentals. QM also predicts for the harmonic oscillator a discrete multi-resonance spectrum at the harmonics of the oscillator natural frequency [33], while the ordinary classical harmonic oscillator supports however a single resonance frequency corresponding to its natural frequency. Fortunately, an investigation using a computational method similar to the one explored in the present work showed that the addition of the ZPF to the classical description of the oscillator gives rise to a discrete excitation spectrum equal to the one predicted by QM [33]. This result suggests that even the quantization seems to be a natural consequence of the ZPF addition to the classic mechanics, while in the QM case the quantization seems to be an imposed non-intuitive characteristic.

A very famous classical problem, the Bohr atom stability, was also treated with success by SED, whereby the electron according to the Rutherford planetary model would absorb energy from the ZPF, which would balance the energy lost by radiation damping, known characteristic of an accelerated charge. This mechanism was demonstrated with success for the Hydrogen atom ground state [6][7].

For a better understanding of this physical model (SED), the reader can consult, in ref. [6], an extensive paper of Boyer (1975) with the most important SED foundations or, for more recent reviews, refs. [34] [40].

Along the years, some investigators have abandoned SED since it failed for non-linear systems [35]. However, others persisted and presently there is still investigation being done in this area. The advances in computational simulation represented a new hope for the SED development. The numerical integration allows solving the SED equations, before hard to solve analytically. Some recent works, as the ones performed by Cole et al. for the Hydrogen atom [35][36], and by Huang and Batelaan for the harmonic oscillator [33][32], have demonstrated the great potential of SED. These classical simulations related with the interaction of a planetary-like orbiting electron with radiation represent not only a development for SED, but can also have practical implications such as the understanding of Rydberg atoms interacting with radiation [35]. Herewith, there is the possibility of controlling the chemical and atomic proprieties of the atoms by means of irradiation or resonant cavity confinement [36][37].

A modern version of SED that includes the spin (SEDS) seems to be very promising since it solves some of the SED failures such as the non-linear potentials [38]. This modification drastically changes the motion equation of electrically charged particles in the ordinary SED realm, because the spin addition reaffirms the influence of the special relativity. SEDS was also able to derivate the Bohr's complete condition, including the excited states. SEDS can even explain some phenomena presently unexplainable by QED, namely:

1) the physical origin of the ZPF, and its natural upper cut-off;
2) an anomaly in experimental studies of neutrino rest mass;
3) the origin and quantitative studies of 1/f noise;
4) the origin of the high-energy tail of cosmic radiation.

This success is due to the fact that SEDS (like SED) consider a real ZPF in contrast with QED, which makes the ZPF renormalization [38].

Other variations of SED were suggested in recent investigations with emphasis to Rodríguez [28], who demonstrates that SED needs some feedback mechanism for the particles to store energy across their random motion in order to maintain their averaged equilibrium. It was suggested that the inner structure of the particles could have the freedom degrees necessary to store energy from ZPF when it is in excess and to release it for the atomic system when it is in defect. This new view of SED could bring new advances, as in the angular momentum quantization and in the excited states of the atoms, among others [28].

## 2.2. Hydrogen atom according to stochastic electrodynamics

Since the main goal of our work is to study the influence of the ZPF in atoms and the perturbations in their energy levels induced by modifications on ZPF, we start with the simplest scenario, the Hydrogen (H) atom.

As it is known since long time, the classical description of the H atom is not consistent with the reality. Any charged particle in an accelerated motion emits Larmor radiation losing progressively its energy [8]. Then, despite of the Coulomb force that maintains the electron in a circular orbit, the Abraham-Lorentz force (product of the radiation reaction) makes the electron quickly collapsing in a spiral orbit towards the nucleus [35][36], whose decay rate is shown in figure 1.

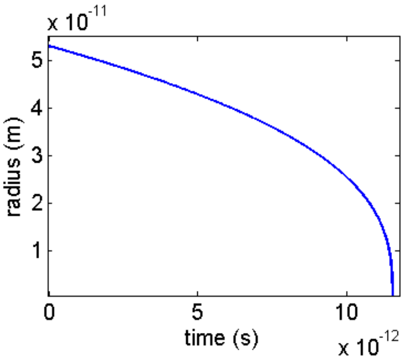

Figure 1: The electron orbit radius of an H atom as a function of time according to the classical theory. Computed with the explicit Runge-Kutta method (ode45 MATLAB's internal function with absolute error tolerance $9 \times 10^7$).

SED solves this orbital instability problem with the addition of a random electromagnetic background even at zero Kelvin, the ZPF [6][7]. This ZPF is the classical description of the one predicted by QM.

The energy lost by the electron in the form of Larmor radiation is by these means compensated by the energy absorbed from the ZPF's electric and magnetic fields [8]. This equilibrium is not static but dynamical instead, due to the random character of ZPF, which causes the electron orbit to acquire a radius distribution in time instead of a static radius, as it will be shown in the next sections. Then, when we refer to stability it is not about a fixed orbit but stability over time, which converges to a fixed orbit radius when we compute the average over all orbit radii for a time long enough. Some authors claim that QM is a static description of property averages but in reality these systems have a frenetic random behaviour induced by ZPF [28]. Hence, SED or some SED version could be a more fundamental theory of the nature than QM.

Looking for the SED's fundamentals, it is reasonable to think that ZPF determines the orbit radius distribution of an electron in the atom, and consequently the ground state energy level is imposed by the ZPF. It then could be possible to influence the atom properties by means of the manipulation of ZPF.

SED has been successful for linear systems such as the harmonic oscillator and for linear fields in Casimir/van der Waals type simulations [6]. However, for non-linear systems, the results seem not to converge with the ones generated by QM [35]. It has been suggested that this discrepancy was due to the difficulties to deal analytically with non-linear differential equations, and then that non-linear systems (such as the Coulomb potential in the H atom) can be successfully solved using numeric simulations [35][36]. In this chapter, we review, replicate and comment some of the work done regarding the electron motion in the H atom by means of numerical integration, with special focus on ref. [35].

### 2.2.1. Motion of the electron in the H atom according to SED

In this section we based mostly on the paper of Cole and Zou [35], however other important works are complementary to this, as refs. [31][36]. In the present work, we tried to replicate the results achieved in ref. [35], related to the electron radius distribution in the classic H atom, using the same terminology and similar approximations. We were still able to make some simulations for longer times relative to the simulations reported in the bibliography. In these simulations, we found for the first time some unexpected orbital behaviours, such as extremely elliptic orbits and a continuous tendency of the electron orbit to outer radius. This observation may arise some doubts concerning the model or even the theory stability.

In order to simplify the H atom model, we made some approximations. Since the proton is much heavier than the electron, we considered the proton mass infinite and the H nucleus motionless in the origin of our referential. We also considered the non-relativist approximation since the electron speed is much lower than the speed of light (approximately two orders of magnitude lower as we will show in the results section). Thus, the Newton's second law of motion is given by equation 2 (in SI units) [35].

$$m\frac{d^2\boldsymbol{r}}{dt^2} = -\frac{e^2\boldsymbol{r}}{4\pi\varepsilon_0|\boldsymbol{r}|^3} + \frac{2e^2}{3c^3}\frac{1}{4\pi\varepsilon_0}\frac{d^3\boldsymbol{r}}{dt^3} - e\left\{\boldsymbol{E}[\boldsymbol{r}(t),t] + \frac{d\boldsymbol{r}}{dt}\times\boldsymbol{B}[\boldsymbol{r}(t),t]\right\} \qquad (2)$$

In equation (2), $e$ and $m$ are respectively the electron charge and mass, $\boldsymbol{r}$ is the electron position vector, $\varepsilon_0$ the vacuum permittivity, $c$ the light speed in vacuum and, finally, $\boldsymbol{E}$ and $\boldsymbol{B}$ are respectively the electric and magnetic field vectors of the ZPF [35]. The first term in the right side of equation (2) is the Coulomb force and the second term is the radiation reaction, a force that is characteristic of all accelerated charge systems. Since the Coulomb attractive force is the dominating force in the electron orbit, the third order derivate of the radiation reaction term can be approximated by equation (3).

$$\frac{d^3\boldsymbol{r}}{dt^3} \approx \frac{d}{dt}\left(-\frac{1}{m}\frac{e^2\boldsymbol{r}}{4\pi\varepsilon_0|\boldsymbol{r}|^3}\right) \approx \frac{e^2}{m}\left[\frac{\frac{d\boldsymbol{r}}{dt}}{|\boldsymbol{r}|^3} - \frac{3\boldsymbol{r}(\boldsymbol{r}\cdot\frac{d\boldsymbol{r}}{dt})}{|\boldsymbol{r}|^5}\right] \tag{3}$$

In order to complete equation (2), we must define the ZPF electric and magnetic fields. However, once again some considerations are required since it is impossible to generate numerically the infinite number of modes of the ZPF. For each ZPF mode, a wave number was associated, in the form of a vector $\boldsymbol{k}$ that defines the propagation direction of each wave. It is also possible to associate to $\boldsymbol{k}$ an angular frequency ($\omega$) given by $\omega = c|\boldsymbol{k}|$. In the free space all the modes are allowed, thus ZPF takes the integral form making the numerical modes generation impossible. However, in a bounded space, such as a box of perfectly reflective walls at zero potential, not all the $\boldsymbol{k}$ modes are allowed [35][32]. The bound conditions impose that all the waves have two nodes coincident with the walls, thus the wavelengths can only be integers of half the box dimension. Hence we can simulate the H atom inside a big cubic box and still have a good approximation to the free space. Consequently, the electric part of the ZPF can be described by a plane wave expansion, as shown in equation (4), solution of the homogeneous Maxwell's equations in a bounded space [35][32].

$$\begin{aligned}\boldsymbol{E}_{ZPF}(\boldsymbol{r},t) = \frac{1}{\sqrt{(L_xL_yL_z)}}\sum_{n_x,n_y,n_z=-\infty}^{\infty}\sum_{\lambda=1,2}\hat{\boldsymbol{\varepsilon}}_{\boldsymbol{k_n},\lambda}\big[A_{\boldsymbol{k_n},\lambda}\cos(\boldsymbol{k_n}\cdot\boldsymbol{r}-\omega_{\boldsymbol{n}}t)\\ + B_{\boldsymbol{k_n},\lambda}\sin(\boldsymbol{k_n}\cdot\boldsymbol{r}-\omega_{\boldsymbol{n}}t)\big]\end{aligned} \tag{4}$$

In equation (4), $\boldsymbol{r}$ is the electron position vector and $t$ the time. Since the waves are related with integer multiples of the box dimensions, it was convenient to associate each wave to the index $\boldsymbol{n}$, so $n_x, n_y$ and $n_z$ take only integer values. The wave number of each wave is then given by $\boldsymbol{k_n} = 2\pi\left(\frac{n_x}{L_x}\hat{\boldsymbol{x}} + \frac{n_y}{L_y}\hat{\boldsymbol{y}} + \frac{n_z}{L_z}\hat{\boldsymbol{z}}\right)$, where $L_x, L_y$ and $L_z$ are the box dimensions [35]. We can also define for future references the box volume by $V = L_x\, L_y\, L_z$. Each wave frequency can be computed from $\omega_{\boldsymbol{n}} = c|\boldsymbol{k_n}|$. According to SED, the waves don't have a preferential polarization, so each wave contains two polarization components orthogonal to the propagation direction [35]. The symbol $\lambda$ represents each of these polarizations and consequently we have $\boldsymbol{k_n}\cdot\hat{\boldsymbol{\varepsilon}}_{\boldsymbol{k}_n,\lambda} = 0$ and $\hat{\boldsymbol{\varepsilon}}_{\boldsymbol{k}_n,\lambda}\cdot\hat{\boldsymbol{\varepsilon}}_{\boldsymbol{k}_n,\lambda'} = 0$ for $\lambda \neq \lambda'$. The constants $A_{\boldsymbol{k_n},\lambda}$ and $B_{\boldsymbol{k_n},\lambda}$ are real numbers generated randomly in the beginning of each simulation [35]. The algorithm to generate these random numbers was designed so that the numbers are generated according to a Gaussian distribution with centroid at zero and second moment equal to $\langle A^2_{\boldsymbol{k_n},\lambda}\rangle = \langle B^2_{\boldsymbol{k_n},\lambda}\rangle = \frac{\hbar\omega_{\boldsymbol{n}}}{2\varepsilon_0}$ ,which corresponds to the spectral distribution of the ZPF, described by the equation (1) [35].

Alternatively, we can represent the ZPF in another form, this new representation being used in chapter 3. In equation 4 the random character of the ZPF appears in the form of random generated amplitudes in two trigonometric functions, however this is equivalent to one fixed amplitude trigonometric function with random generated phase [6]. And thus we can express $\boldsymbol{E}_{ZPF}(\boldsymbol{r},t)$ as in equation 5 [32].

$$\boldsymbol{E}_{ZPF}(\boldsymbol{r},t) = \frac{1}{\sqrt{(L_x L_y L_z)}} \sum_{n_x,n_y,n_z=-\infty}^{\infty} \sum_{\lambda=1,2} \hat{\boldsymbol{\varepsilon}}_{\boldsymbol{k_n},\lambda} \left[\sqrt{\frac{\hbar\omega_{\boldsymbol{n}}}{\varepsilon_0}} \cos(\boldsymbol{k_n}\cdot\boldsymbol{r} - \omega_{\boldsymbol{n}} t + \theta_{\boldsymbol{n}})\right] \tag{5}$$

Even being equation (4) a discrete sum of waves, since the index $\boldsymbol{n}$ takes infinite values (positive and negative), to limit the number of waves it is then required to define a minimum ($\omega_{min}$) and maximum ($\omega_{max}$) frequencies. The minimum frequency may correspond to the largest wave allowed in the box and the maximum frequency will determine the minimum radius for which the simulation is valid [35].

The magnetic part of the ZPF is easily generated from the electric part. Thus $\boldsymbol{B}_{ZPF}(\boldsymbol{r},t)$ is obtained from equation (4) by replacing $\hat{\boldsymbol{\varepsilon}}_{\boldsymbol{k_n},\lambda}$ by $\frac{1}{c}\hat{\boldsymbol{k}}_{\boldsymbol{n}} \times \hat{\boldsymbol{\varepsilon}}_{\boldsymbol{k_n},\lambda}$ [35].

We are now capable of integrating the differential equation (2) and in that way tracking the electron in the H atom.

### 2.2.2. Approximations and algorithm implementation

An exact implementation of the method described in the last section would be computationally very heavy and the integration of equation (2) would be very slow. Some more approximations are then required, as proposed in ref. [35]. The starting point is restricting the electron motion to a single plane ($xy$ plane) and then eliminating the number of possible waves. Since we forced the electron motion in the $xy$ plane, we need to eliminate the waves which can induce a force in the $z$ axis[6], yet preserving the validity of the relevant physical effects. For this we made the box in such a way that the

---

[6] As in simulations, these waves don't make any difference in the electron motion, they will only waste CPU time.

dimensions in the $x$ and $y$ axis are so small that there are not any waves travelling in these directions, so there are only waves travelling in the direction orthogonal to the plane $xy$. Of course in reality there will always be waves of higher frequencies travelling in these directions ($x$ and $y$) but these ZPF frequencies are too high to influence an electron whose frequency is much lower, so it is not necessary to generate these waves. This approximation is just the same as to make $n_x$ and $n_y$ equal to zero in equation (4). Consequently, for the simulated radius range, the electron will only interact with the waves propagating in the $z$ direction (positive and negative). And by definition, the electric fields $\boldsymbol{E}_{ZPF}(\boldsymbol{r},t)$ of such waves (and the related forces) have components only in the $xy$ plane. The magnetic fields $\boldsymbol{B}_{ZPF}(\boldsymbol{r},t)$ of these waves and the electron speed vector have components only in the $xy$ plane, so the resulting force will only have a component in the $z$ direction, making the interaction of the electron with $\boldsymbol{B}_{ZPF}(\boldsymbol{r},t)$ absent in the 2D approximation. Thereby only the electric part of the ZPF remains, enabling a decrease to half the number of waves that would be present in the free space. Furthermore, as we generate only the waves in the $z$ direction, we decrease the total number of waves to the cubic root.

Now we define the box size, as in ref. [35], $L_x = L_y = 37{,}4$ Å (much longer than the Bohr radius $\approx 0.529$ Å ) and $L_z = 40\,850\,000$ Å $= 0{,}41$ cm.

As mentioned before, we also need to define $\omega_{max}$ and $\omega_{min}$. The relation between each frequency and each $n_x$ is easily obtained from equation (6). And the relation between a radius and its resonant frequency is given by equation (7) that was obtained equalising the centripetal and Coulomb forces.

$$\omega_{n_x} = \frac{2\pi c}{L_z} n_x \tag{6}$$

$$\omega = \sqrt{\frac{e^2}{4\pi\varepsilon_0 m r^3}} \tag{7}$$

The minimum frequency allowed in the box is the one for which $n_x = 1$. This $\omega_{min}$ is also the orbiting frequency of a circular orbit of radius $r_{max} = 1{,}06 \times 10^{-7}\ m$, which is the maximum radius the electron can achieve. If this value is exceeded, the simulation is not valid; in that case no wave would influence the electron, and it would be the same as the inexistence of ZPF. We have chosen $r_{min} = 1 \times 10^{-11}\ m$, and therefore$\omega_{max}$ to be generated is $5{,}03 \times 10^{17} s^{-1}$. The box size ($L_x$ and $L_y$) was also made in such way that $\omega_{min}$ of the waves traveling in the plane $xy$ is $5{,}04 \times 10^{17} s^{-1}$, thus for the electron radius there are no resonant waves travelling in the plane $xy$.

Even after all these approximations, the time required to track the electron, during for example $1 \times 10^{-11}\ s$ in a personal computer, could be much longer than 1 month. One more important approximation is therefore needed. Since the electron absorbs energy mostly from waves in resonance with its orbital frequency, we will use a window of frequencies at each iteration of the integration. This window ($\Delta\omega$) is defined by a minimum and a maximum frequencies that are related with a maximum and a minimum radius, respectively. As suggested by Cole et al. in ref. [35], $\Delta\omega$ should include all the waves between two frequencies, which correspond to the two radius, $r_- = r - 0{,}03r$ and $r_+ = r + 0{,}03r$, where $r$ is the instantaneous radius at each iteration. This window is not static, instead it changes its width and centroid as the electron is closer or further away from the nucleus. The aim is to compute in each integration the resulting force of all the waves near the electron resonance frequency since the other waves wouldn't have a significant influence in the electron motion.

### 2.2.3. Results of the simulations

We ran our code (implemented in MATLAB) in three personal computers. We made several simulations during several months. It was interesting to notice that some simulations were taking much longer times than others. The reason is the difference in time that the algorithm takes to integrate small and large orbits, the last ones being quickly integrated.

The initial conditions of the electron were the Bohr radius ($\sim 5.3 \times 10^{-11}\ m$) and the correspondent velocity ($\sim 2.2 \times 10^{6}\ m/s$).

The approximations taken are the same as explained in the last section, except that we generated only waves travelling in the positive direction. However, due to the random character of the waves' amplitude, we expect similar results. We then integrated the electron motion for 32 independent atoms, each one for a unique ZPF generated at the beginning of each run.

The outputs of each run are the electron position and velocity (saved in time intervals of $6 \times 10^{-17}\ s$) as a function of time. From this information, in order to visualize the "electronic cloud", we can plot all the positions that the electron took. We can also plot the orbit radius as a function of time or the absolute frequency histogram of the electron radius. As example, the electron radius as a function of time is plotted in figure 2, where we can see a stochastic variation of the electron radius.

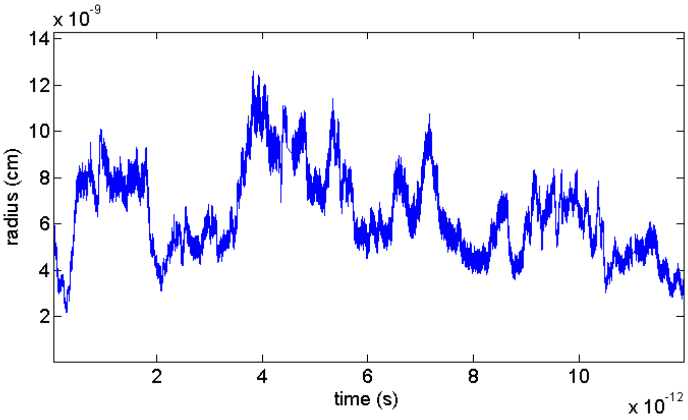

Figure 2: Plot of the electron orbit radius variation with time for one simulation.

As an attempt to replicate the results of Cole and Zou [35], we made for each simulation a frequency histogram and then we summed all the histograms to accumulate statistic. The resulting histogram is the orbit radius distribution of the electron according to SED. We didn't take into account the first $5 \times 10^{-13}$ seconds to reduce the initial conditions influence in the histogram. To visualise the histogram variation with the amount of statistics accumulated, we plotted four histograms computed for increasing times, the results being shown in figure 3. We denote by $N_{sum}$ the amount of entries in each histogram, the sum of all the absolute frequencies (the curve integral). To compare the electron orbit radius distribution in the SED framework with the correspondent QM prediction, we also plotted the radial density curve $P(r)$, from the Schrodinger's wave equation for the ground state of the H atom. This last curve was normalised to the histogram in such a way that the areas under the two curves are the same. $P(r)$ is given (in CGS units) by equation (8):

$$P(r) = A\frac{4r^2}{a_B^3}\exp(-\frac{2r}{a_B}) \tag{8}$$

where $a_B = \frac{\hbar^2}{me^2}$, and A is the normalization constant [35].

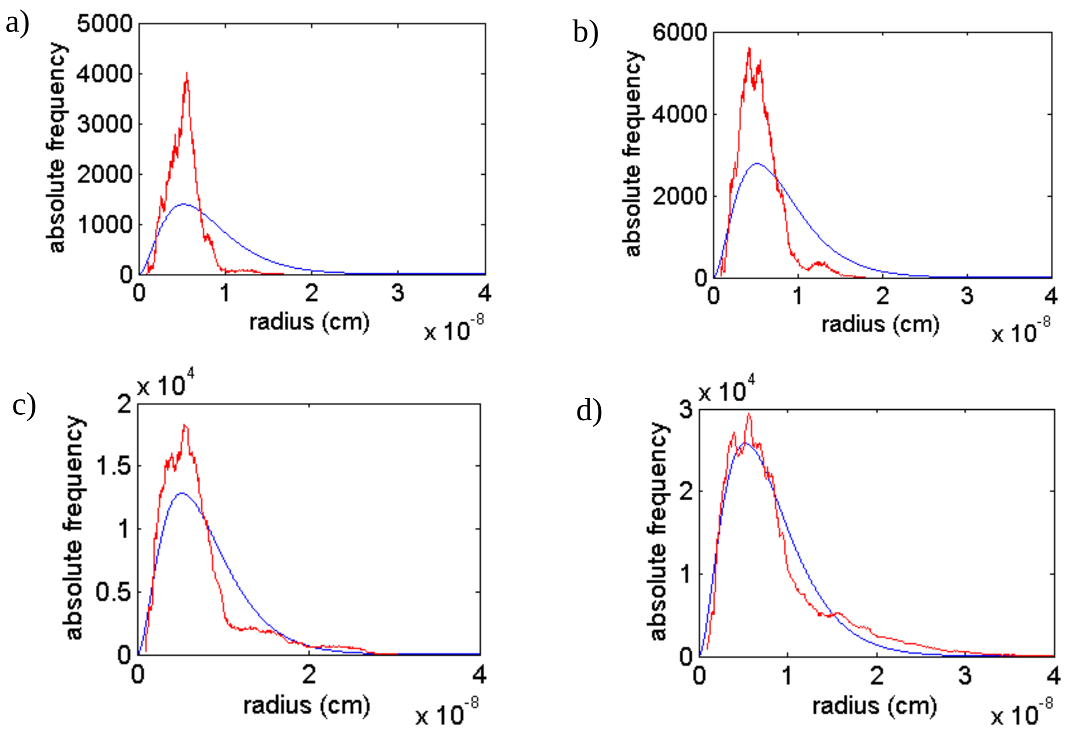

Figure 3: Electron orbit radius distribution (in red ) computed for increasing time ranges. The amount of histogram entries $N_{sum}$ is: a) $5.2 \times 10^5$; b) $9.6 \times 10^5$; c) $25.6 \times 10^5$; d) $36.2 \times 10^5$. Each histogram is composed by 600 divisions. The normalized $P(r)$ curve obtained by the Schordinger's wave equation is also shown (in blue). The maximum simulated time for each run was $1.4 \times 10^{-11}\ s$.

As we can see from the figure 3, the radius distribution computed by our algorithm seems to converge to the QM prediction, and this notable remark was first observed by Cole and Zou [35]. This result validates our algorithm and thus we can use the code for other proposes, such as simulations with other initial conditions, research for excited states or even adapt it for multi-electron models as the He atom.

After this test, we performed additional tests with the same model for an atom inside a smaller cavity. We started to decrease only $L_z$, however since $L_x$ and $L_y$ are already too small the increment of the normalization constant in equation (4), which depends on the box dimensions, gives higher amplitudes to the waves. These very intense waves induced colossal variations in the electron orbit radius, always kicking it for growing elliptic orbits. We still tried to manipulate $L_x$ and $L_y$ to decrease the wave amplitudes, yet it resulted again in strong resonant effects (now of lower amplitude), where the electron could maintain an immutable elliptic orbit for a long time without significant random fluctuations. We suspect these results are due to the large spacing between adjacent frequencies (characteristic of the small box) in addition to the fact that, for this one-dimensional ZPF, there are few waves of similar frequencies. Using a full three-dimensional ZPF, the number of waves is cubed, yielding much more waves of similar frequencies even for a small box. Anyway, the one-dimensional ZPF doesn’t seem to us a credible approximation, as we will explain better in the beginning of the next chapter.

Fortunately we had access to a computer cluster and during this time we tried to evaluate the model stability. According to SED, the electron orbit should be stable, so if the model is stable the electron orbit radius should not have a tendentious behaviour along time, but instead it would always have a random motion without colliding against the nucleus or ionize, whatever the simulation time. In addition to this, for a long enough time, the radius distribution of a single simulation should be similar to the Schrodinger equation prediction, without the need of accumulating statistics from other simulations.

We run the previous 2D-algorithm (this time implemented in C++) for longer times, generating waves travelling in positive and negative directions. We made a set of 16 simulations up to $10^{-9}\ s$. Some of them didn’t reach the end time because the electron crossed the radius limits ($r_{max}$ and $r_{min}$), forcing the simulation to stop. To validate the implementation of this algorithm in C++, we computed the radius distribution (of the 16 simulations summed up) accounting for shorter times only. The solution seems also to converge with the QM prediction, as shown in figure 4. However, for longer times the result seems to deviate from the QM prediction, as shown in figure 5. From the various plots we often see a tendentious motion, either to outer orbits or to the nucleus direction. However, we don’t know what would happen for radius shorter than $r_{min} = 10^{-11}\ m$, maybe the electron can collide with the nucleus, or can return to outer orbits, thus keeping the atomic stability. Thus, the growth towards outer orbits for longer times (figure 5) is in part due to the stopped simulations, remaining only the simulations that never reached the minimum radius. This aspect can be improved in the future by decreasing the minimum radius, however there will always be a computational limitation. For example, if we decrease by half the actual minimum radius, the number of ZPF generated modes will be doubled. In addition, in some cases we also observe a continuous tendency towards outer orbits with extremely elliptic behaviours, an effect shown, for example, in figure 6.

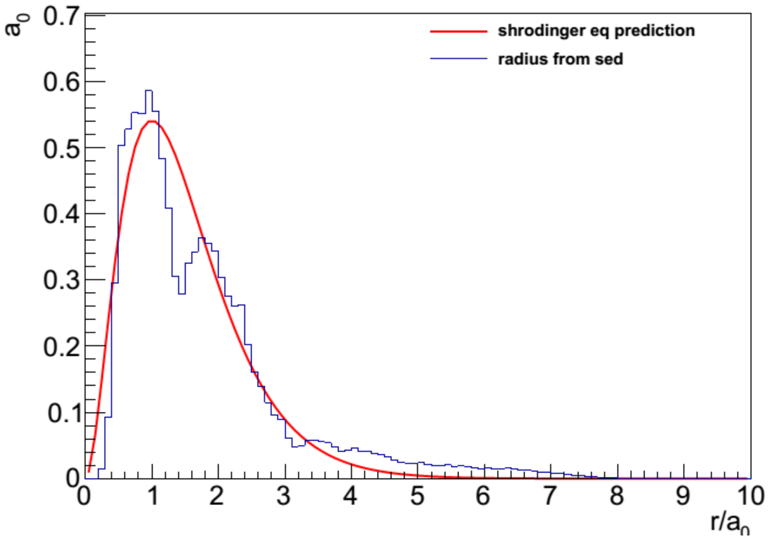

Figure 4: In blue, the electron radius distribution (histogram) computed from all the 16 simulations summed up ($5 \times 10^{-12}\ s$), accounting for shorter times. In red, the normalized $P(r)$ curve obtained by the Schordinger's wave equation. The axis units are normalised to the Bohr radius, represented by a$_{0}$.

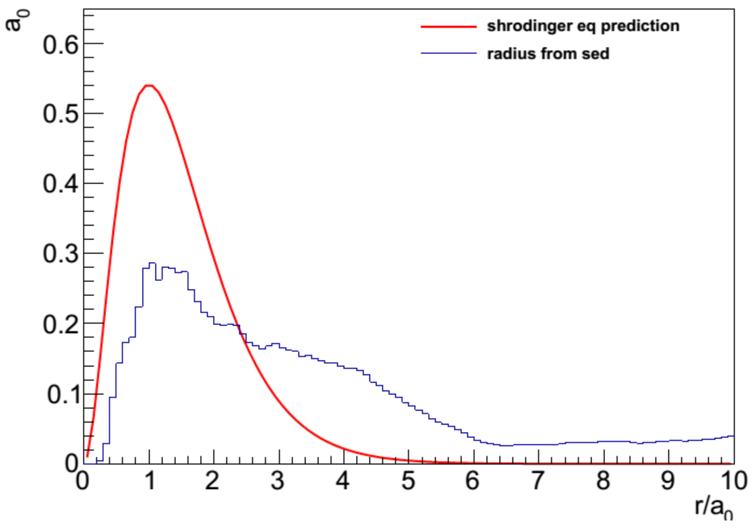

Figure 5: In blue, the electron radius distribution (histogram) computed from all the 16 simulations summed up ($10^{-9}\ s$), accounting for longer times. In red, the normalized $P(r)$ curve obtained by the Schordinger's wave equation. The axis units are normalised to the Bohr radius, represented by a$_{0}$.

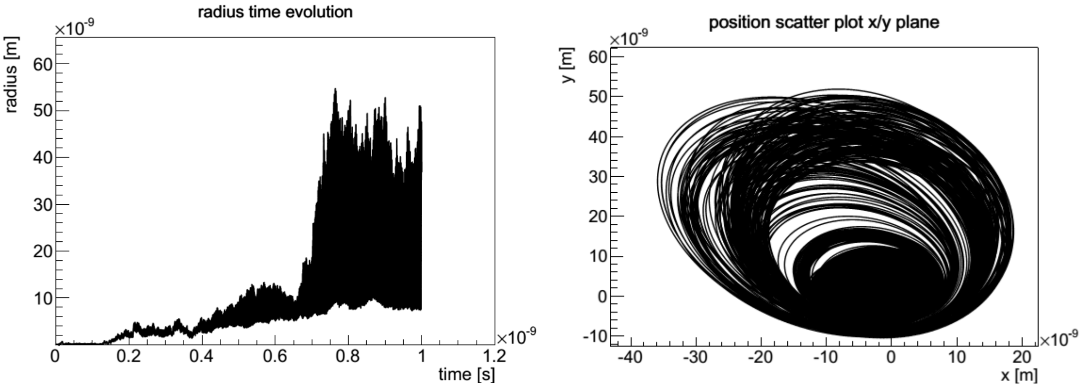

Figure 6: The left plot is the radius variation with time. The right plot is the correspondent electron position in the xy plane.

Despite the notarial tendentious behaviour in some cases, no simulation alone was able to reproduce a radius distribution similar to the one predicted by QM. Thus, we can conclude that, for longer times, either this method is not stable or the approximations used are not suitable, or still SED is incomplete.

# 3. Three-dimensional ZPF

Although it was used in the past, the one-dimensional representation of ZPF is not realistic. Even if we consider a parallelepiped box as Cole and Zou [35], where one dimension is much bigger than the others, it's not a good approximation of the free space. To evaluate this affirmation we can consider the model described by Cole and Zou, explained in sections 2.2.1 and 2.2.2 [35]. If we make *Lx* and *Ly* small enough to suppress all the waves in resonance[7] with the electron radius down to $10^{-11}\ m$, the only ones that contribute to the radius fluctuations are the waves propagating in the *z* direction. Then we can make *Lz* big enough to consider the *H* atom in free space. However, the normalization factor $\left(\frac{1}{\sqrt{Lz\times Ly\times Lx}}\right)$ in equation (4) depends not only on the *Lz* dimension but also on *Ly* and *Lx*, so the box size (*Lz*, *Lx* and *Ly*) dictates the waves' amplitude. Consequently, although we fix *Lz*, which preserves the number of modes inside the box, by changing *Lx* and/or *Ly* the resulting electron behaviour induced by the ZPF will be different, since the normalization factor influences the waves' amplitude. In conclusion, if the purpose is to simulate the free space, a model that gives us different results to the same problem cannot be fully right.

An alternative is to use a cubic cavity with the three dimensions large enough to consider the atom in free space. Thus ***k*** is distributed uniformly in a cubic mesh. This method is nothing more than the direct application of equation (4). However, as Cole et al. noticed, it can be computationally very hard. As the number of waves present in the box is raised to the cube, while in the previous method we dealt with approximately $10^6$ elements in a matrix, now in a cubic box there will be $10^{18}$ elements in a matrix.

In this chapter, we treat the ZPF in a cubic box, meaning that the propagation vector of the waves will have three-dimensional components. We started with a method, which will be called "Spherical Method", to generate a 3D ZPF. In the annexe 8.1 we refer two works that introduced this method. There, we also implement some of these ideas using MATLAB and replicate with success some effects. In section 3.1, we develop our own method, the Perfect Box Method, and an algorithm that better satisfies the requirements of this work. Aiming to make a preliminary estimation of the shift of the averaged radius

---

[7] The term "waves in resonance" is used for the waves whose frequency is close to the electron angular frequency.

of the bounded H atom, we start by resuming what is relevant in the literature and, in section 3.2, we perform some calculations for the H atom in free space. In section 3.4, we introduce the perturbations induced in the averaged radius of the H atom when ZPF is modified. Finally, in sections 3.4 and 3.5, we try to compute the shift on the equilibrium radius of the H atom induced by a ZPF modification, using the Spherical Method and the Perfect Box Method.

The reader should take in account that in this chapter, up to section 3.6, we only deal with the electric field. However, for future works, the magnetic part of the ZPF can be easily obtained (as explained in the previous chapter) from the electric part of the ZPF.

## 3.1. Perfect box method

As discussed in annex 8.1, the spherical method can be unreliable when used in small boxes where the density of ***k***-vectors in the ***k***-space is too low (corresponding to a small number of waves *N*), a situation for which the spherical method does not work so well also, since it does not preserve real geometrical ***k***-vector characteristics. Therefore, we need to find a more realistic description of ZPF to simulate the effects of bounded ZPF, the main purpose of this work. The simplest, realistic and computational achievable form of representing the waves inside a cubic box is to generate a set of ***k***-vectors in a perfect cubic mesh between a maximum and minimum frequencies. This method is also important to generate a trusty ZPF for future simulations where accuracy is the main requirement, as it is in our case.

Since we have not found in the literature an algorithm to generate such ZPF, we developed one and implemented it in MATLAB. This algorithmic is described in the following paragraphs.

First, a set of points is generated, each point described by three coordinates, represented by a matrix of integers. These points correspond to a perfect cubic mesh in a Cartesian space. The maximum possible integer ($n_{max}$) generated is computed from the maximum frequency, which is related with the defined maximum radius of the electron orbit, according to equation (9).

$$n_{max} = \frac{L\omega_{max}}{2\pi c} \tag{9}$$

After that, an iterative algorithm removes the points whose frequency is greater than $\omega_{max}$ or lower than $\omega_{min}$. The iterative algorithm also creates new points between the original points, increasing the number of points in the matrix by a factor of 8 in each iteration and always eliminating the points outside the frequency window. We have made this iterative method because it was computationally too heavy to create all the points in the beginning (since the quantity would be huge) and then cut out the ones outside $\Delta\omega$. Therefore, we refine the mesh iteratively cutting always the edges (i.e. the points outside $\Delta\omega$) at each iteration. The result is a 3D spherical layer of integer points (each one described by 3 coordinates) whose width is proportional to the difference between the maximum and minimum frequencies. As an example, a slice on the plane $z = 0$ of these points (integer version of $\boldsymbol{k}$-vectors) is plotted in figure 7, where the cubic disposition of the points is perceptible.

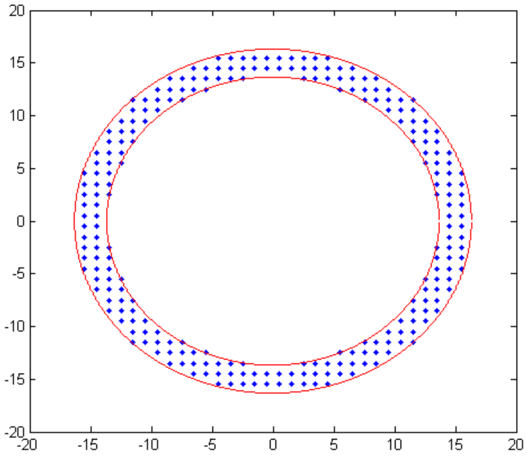

Figure 7: 2D representation of the integer points (blue dots) related to $\boldsymbol{k}$-vectors in the plane $z = 0$. The points outwards the two limits (red circles), related to a maximum and a minimum frequency, were taken out. This sample was generated for the Bohr radius, for a box of side ($L$) equal to 400 μm.

This spherical layer of integer points is saved together with 2 more random numbers associated to each point, completing all we need to describe the ZPF according to our approximations. Each of these random numbers was generated uniformly between 0 and $2\pi$. They will constitute the random phase for each polarization of the wave described by each $\boldsymbol{k}$-vector. Finally the correct $\boldsymbol{k}$-vector matrix is obtained from the multiplication of the integer points saved by the space between adjacent $\boldsymbol{k}$-vectors ($\Delta k$), which in turn is related with the box volume and described by equation (10).

$$\Delta k = \frac{2\pi}{L} \tag{10}$$

It’s important to note the difficulties of a trusty generation of the ZPF in free space. For example, the number of $\boldsymbol{k}$-vectors generated for a cubic box of $L = 400\ \mu m$ for all the frequencies resonating with the radius between $R_{min} = 10^{-11}\ m$ and $R_{max} = 1{,}06 \times 10^{-5}\ m$ (the dimensions used by Cole et al. in Ref. [35]) is about $9\times10^{18}$. Accounting the two polarizations of the electric fields, this matrix will be doubled. As we can see, for a personal computer, a matrix with such number of elements is impossible to save in the RAM memory. The solution we found was to create and save the ZPF (the $\boldsymbol{k}$-vectors and the random numbers) into data files for different intervals of $\Delta\omega$. Thus, when we make the simulation of the electron motion (or other kind of simulation) we load into RAM memory the corresponding ZPF file that contains the waves resonating with the present orbit radius of the electron. This operation of constant opening and closing the files and writing to RAM memory will make the simulation time much longer.

## 3.2. Equilibrium radius evaluation in the free space

Boyer [6] and other authors [7] have suggested that the atomic stability (as the harmonic oscillator stability) is the result of the equilibrium between the power absorbed and the power radiated by the electrons. Let us consider the simple case of a one-dimensional harmonic oscillator of natural frequency $\omega_0$ immersed in the ZPF, located in the origin and with its motion in the $x$ axis. In these conditions, the motion equation is given by equation (11), where we use the non-relativistic Newton motion law for all the forces applied in the oscillating charge [7].

$$\ddot{x} = -{\omega_0}^2 x + \Gamma \dddot{x} + \frac{e}{m} E_x^{ZPF}(0,t) \qquad (11)$$

As we are considering an oscillating electron, the constants $e$ and $m$ are respectively the electron charge and mass. $E_x^{ZPF}(0,t)$ is the $x$ component of the ZPF electric part in the referential origin. The first term in the right side of equation (10) is the restoring force characteristic of the harmonic oscillator, the third term is the force induced by the ZPF spectrum, and the second term is the self-reaction term, where the constant $\Gamma$ is related to the radiation damping. This characteristic damping of an accelerated charge is created by the Abraham–Lorentz force. In SI units, $\Gamma$ takes the form shown in equation 12 [7],

$$\Gamma = \frac{e^2}{6\pi\varepsilon_0 mc^3} \tag{12}$$

where $\varepsilon_0$ is the permittivity of the vacuum and $c$ the speed of light in vacuum.

As explained in refs. [7], [32] and [36], in the case where the Coulomb force is predominant, we can simplify the self-reaction term, resulting equation (13).

$$\ddot{x} = -{\omega_0}^2 x - \Gamma {\omega_0}^2 \dot{x} + \frac{e}{m} E_x^{ZPF}(0, t) \tag{13}$$

With equation (13) and the ZPF spectrum distribution described by equations (4) or (5), both describing the ZPF, it is possible to deduce the average power absorbed from the ZPF by the electron, as shown in equation (14) [7].

$$\langle P^{abs} \rangle = \langle \boldsymbol{F} \cdot \boldsymbol{v} \rangle = \frac{e^2 \hbar {\omega_0}^3}{12\pi\varepsilon_0 mc^3} \tag{14}$$

Now, for the H atom system, we can consider the Bohr model, in which the ground state is described by a circular orbit of radius $r_0$, as two one-dimensional harmonic oscillators in quadrature. Taking this argument into account, the quantity in equation (14) will be doubled in the case of a circular orbit. As a result, according to our approximation to the circular orbit, the power absorbed will be twice the power absorbed by a single harmonic oscillator [7].

Considering circular orbits, since a Coulomb central force is applied to an electron by a point size proton whose mass is considered infinite, the radius of the circular orbits is related with its angular frequency by the equation (14)[8].

$$\omega_0 = \frac{e}{\sqrt{4\pi\varepsilon_0 m {r_0}^3}} \tag{15}$$

Substituting $\omega_0$ from equation (15) in equation (14), we obtain equation (16), which gives us the average power absorbed as function of the electron radius.

$$\langle P^{abs} \rangle_{circ} = \frac{e^5 \, \hbar}{48 \, c^3 (\pi m \varepsilon_0)^{\frac{5}{2}} \, {r_0}^{\frac{9}{2}}} \tag{16}$$

---

[8] Equation (14) can be obtained by equalling the centripetal and Coulomb forces.

To deduce the average radiated power as function of the electron radius for the H atom, we start by calculating the power radiated by an electron with acceleration A in a circular orbit. It is given by equation (17) [7].

$$\langle P^{rad} \rangle_{circ} = \frac{e^2\, A^2}{6\pi\varepsilon_0 c^3} = \frac{e^2\, (r_0 {\omega_0}^2)^2}{6\pi\varepsilon_0 c^3} \tag{17}$$

Again, for the $H$ atom, we can use equation (15) to obtain the radiated power as a function of the radius, as shown in equation (18).

$$\langle P^{rad} \rangle_{circ} = \frac{e^6}{96 m^2 (\pi c \varepsilon_0)^3 {r_0}^3} \tag{18}$$

It is perceptible that the average powers absorbed and radiated by the electron have different dependences on the electron radius. As we can see from the plot of figure 8, the power absorbed is predominant for smaller radius, while for bigger radius the radiated power is predominant. This behaviour suggests the existence of an equilibrium radius, since for shorter radius the electron absorbs more energy from the ZPF than the one it radiates, leading to bigger orbits, and for larger radius the radiated energy is greater making it to decay to smaller orbits. According to this hypothesis, the average radius will be obtained by equalling equations (16) and (18) or by the intersection of the two curves (power radiated and absorbed), as represented in figure 8. For the free space approximation, this intersection yields exactly the Bohr radius ($r_b$) [7].

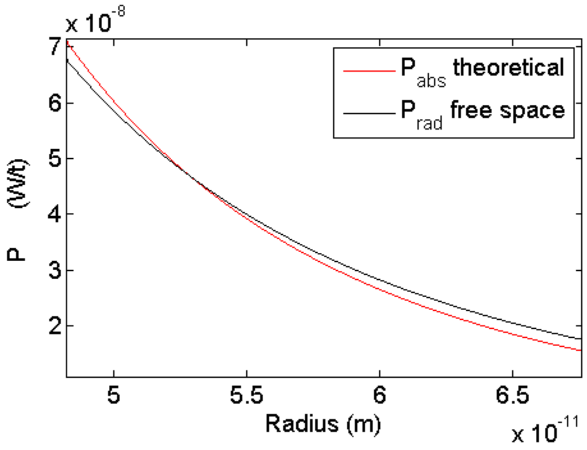

Figure 8: Plot of $P^{rad}$ and $P^{abs}$ computed from equations (16) and (18) for radius between $4.8 \times 10^{-11}\, m$ and $6.8 \times 10^{-11}\, m$. The interception of the two curves is exactly $r_b$.

We have considered the power radiated by an electron in a circular orbit as independent on ZPF, at least when described by equation (18). On the other hand, according with our approximations, ZPF plays a crucial rule in the absorbed power. In this work, we are considering the hypothesis that the atom stability is due to the equilibrium between $P^{rad}$ and $P^{abs}$. Then, as $P^{abs}$ depends on ZPF, it is reasonable to assume that a different ZPF could result in a different equilibrium state that can change the energies of the ground and excited states of the atomic systems. It's now clear the need to study $P^{abs}$ when ZPF is changed as in the case of a cubic box of perfect metallic neutral walls. To the best of our knowledge, such study is absent in the literature.

### 3.3. Equilibrium radius evaluation in a reflective box

Equation (14) was deduced for the free space where the frequency spectrum is continuum, while in a box the frequencies take discrete values. From refs. [7] and [40], it is possible to deduce in SI units $\langle P^{abs}\rangle_{circ}$ for a discrete ZPF spectrum, as seen in equation (19).

$$\langle P^{abs}\rangle_{circ} = \frac{e^2}{m}\sum_{\boldsymbol{k}} a^2(\omega)\ \frac{\Gamma\,\omega^4}{({\omega_0}^2 - \omega^2)^2 + \Gamma^2\omega^6}\left(1 - \frac{k_x^2}{|\boldsymbol{k}|^2}\right) \tag{19}$$

In equation (18), a sum is made over all waves associated to the $\boldsymbol{k}$-vectors and to frequencies $\omega$. As seen before in section 2.2.1, equations (4) and (5), the amplitude of each wave for the bonded space, as considered here, is well described by equation (20), where $V$ is the volume inside the box..

$$a(\omega) = \sqrt{\frac{\hbar\omega}{\varepsilon_0 V}} \tag{20}$$

Since infinite multiples of the fundamental frequency are admitted in the box, even inside a small box ZPF will have infinite modes making the computation impossible. However, the electron in the circular orbit will absorb energy mostly from the resonance modes. Therefore, if we select a window of modes whose frequencies ($\omega$) are close to the natural frequency ($\omega_0$), we should have a good approximation of $P^{abs}$. To define this window, we must evaluate the integral of the continuum ZPF in free space for different frequency limits.

In ref. [7], before the final solution shown in equation (14), an intermediate solution was deduced, equation (21), which takes into account the integral over all the continuum frequency distribution of ZPF.

$$\langle P^{abs}\rangle_{circ} = \frac{e^2\hbar}{3\pi^2\varepsilon_0 mc^3}\int_0^\infty \frac{\Gamma\,\omega^7\,d\omega}{({\omega_0}^2 - \omega^2)^2 + \Gamma^2\omega^6} \tag{21}$$

The driven damped harmonic oscillator in the approximation of small damping ($\Gamma{\omega_0}^2 \ll \omega_0$), such as in this case[9], has a strong resonating behaviour. The FWHM (Full Width at Half Maximum) of the resonance curve (amplitude as a function of the driven frequency) is proportional to $\Gamma{\omega_0}^2$. Then we can define a window ($\Delta\omega$) between a minimum and a maximum frequencies that will contain the most significant ZPF waves that can influence the electron motion. This window must be proportional to the resonance curve FWHM, and thus it will be dynamic since it will change with $\omega_0$ and so with $r_0$.

Before computing $P^{abs}$ by the electron of the H atom inside a box, we need to define $\Delta\omega$ large enough to allow a good approximation. Since in a driven damped harmonic oscillator, as the one we are using, described by equation (13), the damping constant ($\Gamma{\omega_0}^2$) is proportional to the resonance curve FWHM, we also made $\Delta\omega$ proportional to $\Gamma{\omega_0}^2$ [32][1]. Taking as a reference the Bohr radius, $P^{abs}$ is calculated using equation (21) for different $\Delta\omega$ values, being $\Delta\omega = \mathrm{f}\,\Gamma{\omega_0}^2$, where f is an integer proportionality constant [32]. In figure 9, we can see the resonance curve of $P^{abs}$ as a function of $\omega$, according to equation (21).

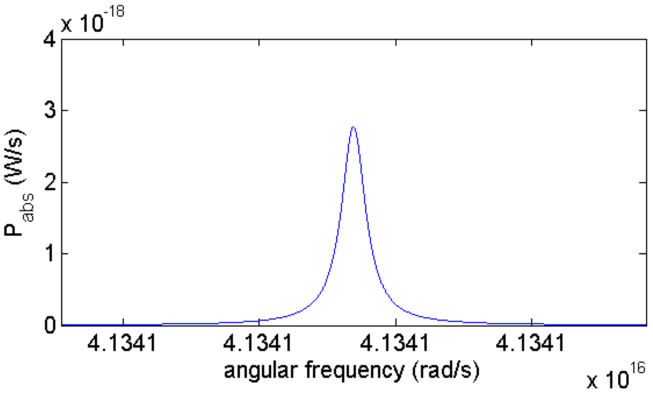

Figure 9: Power absorbed $P^{abs}$ as a function of $\omega$ for the Bohr radius, using $\mathrm{f} = 20$, which corresponds to $\omega$ between $4.134131 \times 10^{16}\ rad/s$and $4.134152 \times 10^{16}\ rad/s$.

---

[9] For the Bohr radius, we have $\Gamma{\omega_0}^2 = 1{,}071 \times 10^{10}$ $(in\ SI\ units)$ and $\omega_0 = 4{,}134 \times 10^{16}\ rad/s$.

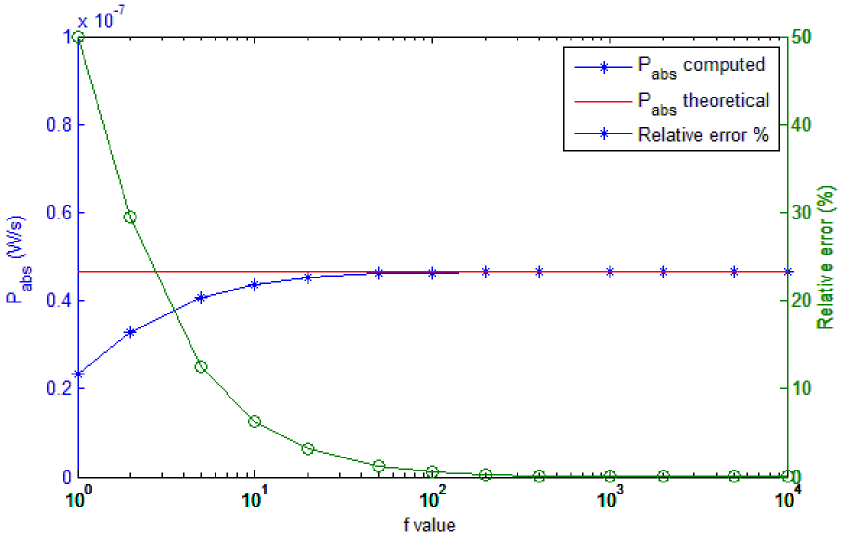

Figure 10: Power absorbed $P^{abs}$ for the Bohr radius computed from equation (21), in blue, and computed from equation (14) ($P^{abs} = 4.669311 \times 10^{-8}$ W/s), in red, and the relative deviation between the two curves, in green, as a function of f. The integration was made using the trapezoidal method with $10^7$ steps.

As we can see from figure 10, as large the window is, the smaller is the deviation in $P^{abs}$. So as further away from the resonant frequency are the wave frequencies, less significant is their influence in the electron. Therefore, we only need to consider $\Delta\omega$ large enough to have a small error. For example, with 400 times the quantity $\Gamma{\omega_0}^2$ (f = 400), we have a deviation between the computed and the theoretical values of only 0.16%, which is almost negligible.

The method proposed by us to compute the equilibrium radius ($r_{eq}$) in a box of reflective walls (considering $P^{rad}$ independent from the boundary conditions) starts with the generation of a set of radius between two limits where we suppose to exist $r_{eq}$. Then we compute the total absorbed power for each radius using equation (19), where the $k$-values and the correspondent $\omega$ values are from all the waves present in a box in all possible directions whose frequency is between the limits defined by $\Delta\omega$. The result is a curve of $P^{abs}$ as a function of the radius similar the one generated by equation (14). Since we are considering that $P^{rad}$ is independent from the box dimensions, the curve for the power radiated by the electron is the same as in the free space, described by equation (17). So the radius for which $P^{abs}$ inside the box equals $P^{rad}$ is $r_{eq}$.

### 3.4. Equilibrium radius inside a box using the spherical method

As described in annex 8.1, the Spherical Method enables an easy computational construction of the ZPF [32]. This approximation is however valid only for a large number of waves, and consequently a great density of waves in the $\boldsymbol{k}$-space. But when we decrease the box volume ($V$), the density of waves in $\boldsymbol{k}$-space ($\rho_k$) also decreases, since $\rho_k$ is related to the volume by $\rho_k = V/(2\pi)^3$ [32]. Moreover, in the spherical method there is only one wave for each frequency. Then, for the same $V$ and consecutively the same $\rho_k$, there is a small spacing between adjacent frequencies when compared to the cubic box method described before. This effect can be easily evaluated by comparison of figures (11) and (12)

In figure 11 we can see a plot of several $P^{abs}$ distributions of several $\boldsymbol{k}$ modes for a specific $\Delta\omega$ and for the Bohr radius. To compute the total $P^{abs}$ for this specific radius, we only need to sum all the points according to equation (19). We notice that the random character of the spherical method[10] results in a fluctuation of $P^{abs}$, so to compute $P^{abs}$ for each radius we make the average of a set of computations for the same conditions and radius.

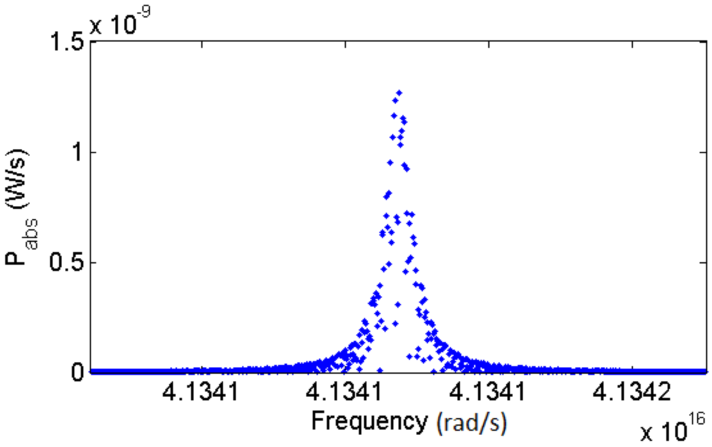

Figure 11: $P^{abs}$ distributions for 800 waves generated in a box of side $1.0514 \times 10^{-5}\ m$, for the Bohr radius and for $f = 20$, which corresponds to $\omega$ between $4.13413112 \times 10^{16}\ rad/s$ and $4.134152543 \times 10^{16}\ rad/s$.

The goal is to compute the variation of $P^{abs}$ with the radius in order to find the radius for which $P^{abs}$ equals $P^{rad}$, so first we need to compute $P^{abs}$ for a set of radius using equation (19). Then we can make a fit of these points in order to search for the interception of the fitting curve and the $P^{rad}$ theoretical curve. The fitting function should be similar

---

[10] Each $\boldsymbol{k}$ wave is generated with a random direction that in the limit of an infinite number of waves generated yields an isotropic distribution of the waves direction.

to the theoretical function, equation (16), but should allow also some freedom in the fitting. Therefore, we chose for fitting equation 22,

$$P^{abs} = ax^b \tag{22}$$

where $x$ is the independent variable and $a$ and $b$ the fitting freedom parameters. In the limit of $V \rightarrow \infty$ these parameters should take the values $b = -4.5$ and $a = \frac{e^5 \hbar}{48\, c^3 (\pi m \varepsilon_0)^{\frac{5}{2}}} = 2.663522 \times 10^{-54}$ (both in SI units), according to equation (16).

However, the fitting method (also used in the perfect box method) is subject of some discussion because the points from which we make the fit don't have a statistical behaviour, they are exactly the power absorbed by the electron in a circular orbit with a specific radius. We know that the smaller the box is, the sparser will be the frequencies of the ZPF. In the case of very small boxes, this effect results in some radius for which the electron doesn't absorb energy and in other radius for which the absorbed energy is colossal (an example of these differences of the box-$P^{abs}$ for adjacent radius are shown in figure 14), resulting in violent fluctuation in the box-$P^{abs}$ curve that is no more the smooth curve of figure 8. Therefore, there are a lot of interceptions of this box-$P^{abs}$ curve and the curve of $P^{rad}$ in free space. In other words, there are multiple $r_{eq}$ very close to each other. However, the force induced on the electron by the random ZPF makes it traveling distances larger than the interval between adjacent equilibrium radius. So, we intuitively expect that in this random motion the box-$P^{abs}$ (the one which have violent fluctuations) will contribute with an average component to the net motion of the electron for longer time scales, being the presence of this multi-$r_{eq}$ masked. Thus we can compute an average curve (this one will already be smooth) by fitting some points of the box-$P^{abs}$ and search the intersection (which correspond to an averaged unique $r_{eq}$) of this average curve with the $P^{rad}$ in free space.

The fitting method for equation (22) is the non-linear least squares. In some cases, mainly for smaller boxes, there will be points extremely high (for which a resonance wave coincides with the radius), so a robust fitting could be more adequate, like the LAR fit that will minimize the least absolute residuals.

The effect of the $P^{abs}$ fluctuations for adjacent radius could have some periodicity and the choice of the set of radius could compromise our understanding of the phenomena. Therefore, to look for this $P^{abs}$ variation as an average behaviour, the radius should be chosen randomly in the interest interval. The number of random radius will be denoted by $rs$ and the number of generated waves by $N$. As explained in annex 8.1, for the spherical method the number of waves and the maximum and minimum frequencies allow us to compute an estimate of the box volume and, consequently, of the box side (denoted by $L$) [32].

The spherical method has success to estimate the free space $r_{eq}$ (equal to the Bohr radius), however for a small cavity the results are questionable. These results and its discussion are presented in annex 8.2.

## 3.5. Equilibrium radius inside a box using the Perfect Box Method

Since the previous method seems to be not reliable, we repeated the same simulations using the Perfect Box Method. This new method has two major advantages: no need of multiple computations of $P^{abs}$ for the same radius since the method doesn't have a random character in the direction of $\boldsymbol{k}$-vectors, opposite to the spherical method, and no need of estimating the box dimensions from the frequency window and number of waves since in this new method the box dimension is an input parameter defined a priori.

For big boxes, even between close values of $\omega_{max}$ and $\omega_{min}$, the number of $\boldsymbol{k}$-vectors generated for each radius is colossal, so it is necessary to compute and save different files with different sets of $\boldsymbol{k}$-vectors. Then the algorithm that computes $P^{abs}$ for each radius iteratively opens the saved files containing the different sets of $\boldsymbol{k}$-vectors, computing the sum of equation (19) for each file and adding always the previous value so that in the end $P^{abs}$ is obtained for that specific radius.

Once again, the frequencies generated for each radius are discrete, however differently from the Spherical Method for the same conditions. In the Spherical Method, each $\boldsymbol{k}$-vector has a distinct frequency, however in a cubic box there are a lot of $\boldsymbol{k}$-vectors with the same frequency[11]. This feature is shown in figure 12, where the box size is larger than the one used with the Spherical Method (figure 11) and even then, the discreetness is bigger than in the Spherical Method.

---

[11] Since $\omega = c|\boldsymbol{k}|$ and, in a cubic 3D mesh in the Cartesian space, there are a lot of points ($\boldsymbol{k}$-vectors) equidistant from the origin.

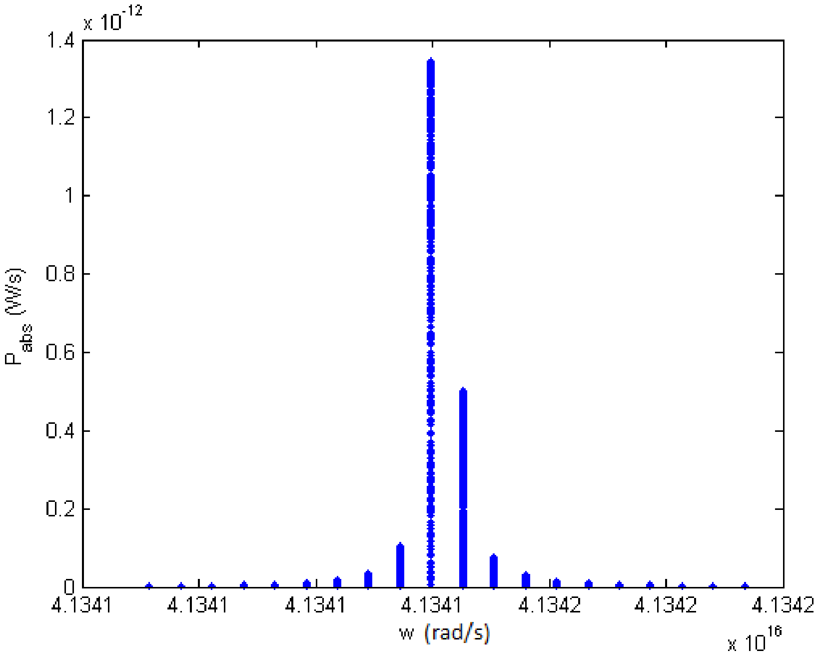

Figure 12: Power absorbed $P^{abs}$ for each wave in a box, for the Bohr radius and for f = 100, which corresponds to $\omega_{min} = 4.13408828 \times 10^{16}\ rad/s$ and $\omega_{max} = 4.13419538 \times 10^{16}\ rad/s$. The box size is $L = 4 \times 10^{-5}\ m$.

Once again the sum of $P^{abs}$ is computed, using equation (19), for each radius as described in annex 8.2. Here we apply the Spherical Method. We also use the fitting method of equation (22) in the same way as described in section 3.4. The terminology defined before in the Spherical Method has the same meaning.

$P^{abs}$ was computed by this new method for the Bohr radius, using f = 400 and $L = 9 \times 10^{-5}\ m$, where we obtained $P^{abs} = 4.663982 \times 10^{-8}\ W/s$, very similar to the analytic value ($4.669311 \times 10^{-8}\ W/s$) obtained from equation (21). This gives us some positive feedback about the reliability of this method.

Now we can estimate $r_{eq}$ for a big box (free space approximation). The power absorbed for a set of random radius chosen between $4{,}97 \times 10^{-11}$ and $5{,}82 \times 10^{-11}\ m$ is shown in figure 13.

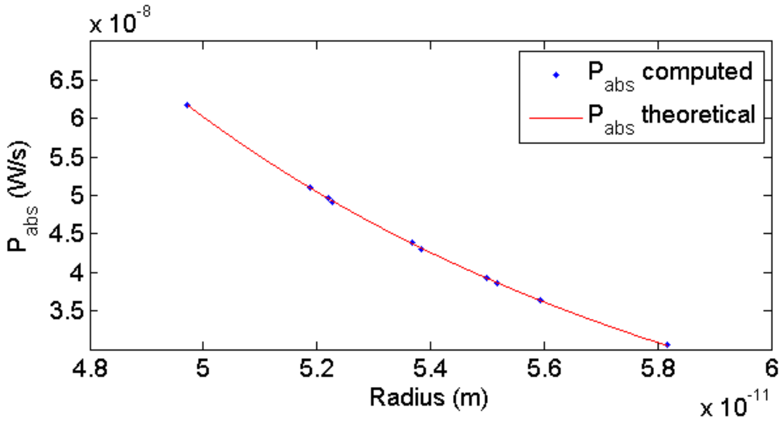

Figure 13: Computed $P^{abs}$ (blue points) from the Perfect Box method for different random radius, and theoretical curve (red line) of $P^{abs}$ for the free space, according to equation (16) . The computation of $P^{abs}$ was performed for a big box with *rs = 10, f = 400* and $L = 8 \times 10^{-4}\, m$.

As we can see from figure 13, there is an agreement between the computed $P^{abs}$ and the theoretical curves. The value of $r_{eq}$ was estimated by the interception between the fitted curve (robust LAR method) and $P^{abs}$ in free space, yielding $r_{eq} = 5.282 \times 10^{-11}$, very close to the Bohr radius $r_b$ (that plot and calculus are not shown in this document). We can then conclude that the algorithm and the code are functional and provide accurate results, at least for the free space approximation. This validation is important for future simulations where a trusty generation of ZPF is required.

We computed the fitting curve of $P^{abs}$ for smaller boxes. In figure 14 we can see an example of $P^{abs}$ as a function of the radius for a small box, together with the theoretical free space curve.

From figure 14 we can observe that, opposite to the Spherical Method, no splitting behaviour is visible (as shown in annex 8.2). This suggests that the Perfect Box method is more reliable for small boxes. It is also shown in figure 14 the expected pronounced scattering. This accentuated difference between $P^{abs}$ for neighbouring radii is originated by the discreteness of $\omega$. As smaller the box used is, the bigger will be the differences on $P^{abs}$ for neighbouring radii.

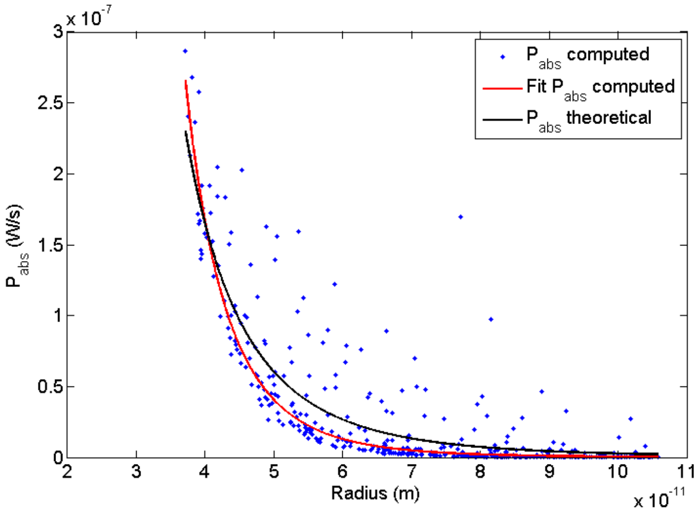

Figure 14: Computed $P^{abs}$ (blue points) using the Perfect Box method for different random radius in a small box, theoretical curve (black line) of $P^{abs}$ for the free space, and fitted curve (red line) using the Robust LAR method to the blue points. The computation of $P^{abs}$ was performed with *rs = 400*, *f = 400* and $L = 5 \times 10^{-5}\ m$.

Once the fiting of the computed data is made, we can find the intersection between $P^{rad}$ and the $P^{abs}$ fitted curve, as in figure 6. The intersection is our estimation of $r_{eq}$. As expected, the $r_{eq}$ for the Hydrogen atom in a small box (at least according with our approximation) is smaller than the value in the free space ($r_b$).

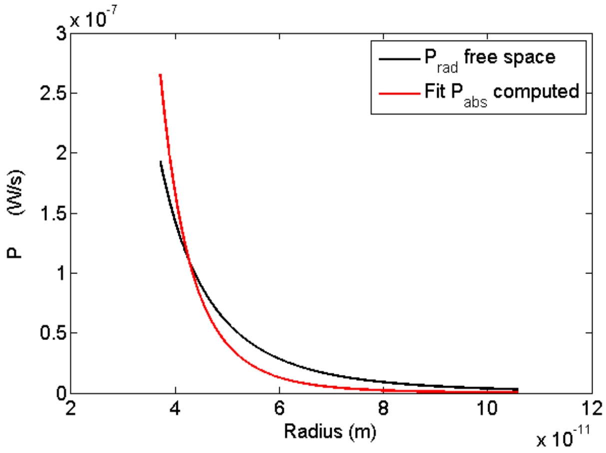

Figure 15: Theoretical curve (black line) of $P^{rad}$ in the free space and fitted curve (Robust LAR method) for a small box (red line). The computation of the $P^{abs}$ was performed with *rs = 400*, *f = 400* and $L = 5 \times 10^{-5}\ m$. The $r_{eq}$ was found to be $4{,}265 \times 10^{-11} m$.

We made some computations as in the previous example (where we used $L = 5 \times 10^{-5}\ m$) but for different box sizes. The results are presented in figure 16. We made fits using the robust LAR method and a non-robust method, however for smaller boxes (L $\ll 10^{-3}\ m$) the non-robust method often produced an extremely low $R^2$, and sometimes the solution did not converge. Thereby we prefer not to pay much attention to the results of the non-robust fit. Still in figure 16 we present both fitting methods for each $L$ value used. Note that there are points from the robust method in figure 16 that don't have correspondent result from the non-robust method, for such L values the fitting curve doesn't intercept the $P^{rad}$ curve. The reason for this failure may be due to the poor fitting quality of the non-robust method, or the interception point could be outside of the radius window used to generate the computed $P^{abs}$ points.

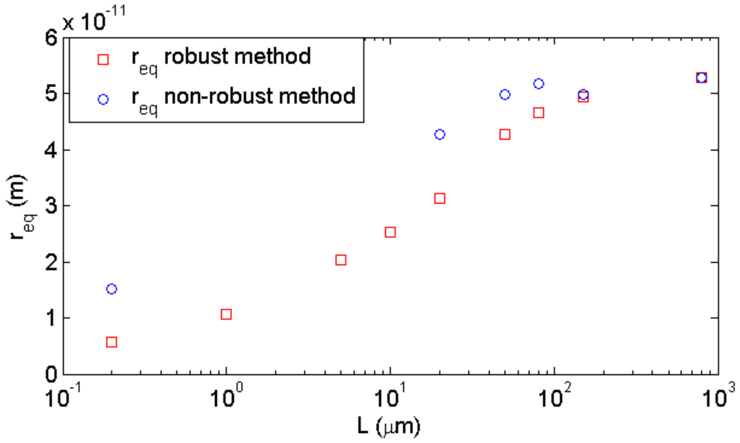

Figure 16: Equilibrium radius $r_{eq}$ of the H atom for different box sizes ($L$). The red squares and blue circles represent $r_{eq}$ computed using the robust method and the non-robust method fittings, respectively. Some computations with the non-robust fitting didn't produce a result, thus some red squares don't have the corresponding blue circle.

As we initially suggested, the H atom equilibrium radius seems to decrease as we suppress more and more ZPF modes, at least if we consider (as we did) that, in a Casmir cavity, the radiated power is not changed and the atom radiates as in free space.

### 3.5.1. Number of absorbed modes

As the radius of the electron in the H atom decreases, its angular frequency increases, as from equation (15). So the damping constant ($\Gamma{\omega_0}^2$) in equation (13) is larger for smaller radius, resulting in a broadening of the resonance curve (figure 9) since the FWHM of a resonance curve of this type is proportional to the damping constant. Thus, according to our approximations, an atom will absorb much more energy from the ZPF modes for smaller electron radius. As an example, we computed the number of modes ($N_{mode}$) transferring energy to the electron in a specific frequency range ($f = 100$) for a box with $L = 4 \times 10^{-5}\, m$, for two different radii, the Bohr radius ($r_b$) and 1.2 $r_b$, resulting respectively in $N_{mode} = 76680$ and $N_{mode} = 22276$. In conclusion, as smaller the electron radius is, the larger will be the number of different ZPF modes transferring energy to the electron.

Now we can evaluate how $N_{mode}$ changes with the box size. We made the same calculations for two boxes sizes, $L = 4 \times 10^{-5}\ m$ and $L = 3 \times 10^{-5}\ m$. As expected, $N_{mode}$ decreases from the bigger box to the smaller one (since the small box has fewer modes), either for the small orbit or for the larger orbit. However, for $r = 1{,}2\ \times r_b$ the decrease in $N_{mode}$ was 64 %, while for $r = r_b$ the decrease was 57 %. This allows us to conclude that a difference in the box size induces a larger perturbation to larger radius orbits than to smaller radius orbits. So, inside a cavity, larger shifts are expected for higher principal quantum number (n), considering the H atom described by the Bohr model.

### 3.5.2. An energetic evaluation

As we are working in the realm of classic mechanics, we will evaluate the energy from that point of view. To compute the energy of the ground state in free space of the Hydrogen atom, we use simple mechanics such as the Newton's second law, to describe the electron motion. Thus, the centripetal force ($F_c$) acting in the electron is given by equation (23) [39].

$$F_c = \frac{mv^2}{r} = \frac{e^2}{4\pi\varepsilon_0 r^2} \tag{23}$$

The kinetic energy of the electron is given by equation (24).

$$T = \frac{mv^2}{2} = \frac{e^2}{8\pi\varepsilon_0 r} \tag{24}$$

Finally, knowing the potential energy ($U$) of the electron in the Coulomb potential, we can sum the electron kinetic and potential energies and compute the total energy ($E$) for the Bohr radius, given by equation (25) [39].

$$E = T + U = \frac{e^2}{8\pi\varepsilon_0 r} - \frac{e^2}{4\pi\varepsilon_0 r} = -\frac{e^2}{8\pi\varepsilon_0 r} = -13.6\ eV \tag{25}$$

Assuming that equation (25) is applicable to a H atom in a reflective box, we computed the energy difference between the ground state of the H atom in the free space and in a reflective box. As an example, we will use $r_{eq}$ obtained for a box with $L = 5 \times 10^{-5}\ m$, as the one of figure 6. For this radius value, the ground state energy is $-14.4584\ eV$, and the expected shift relative to the free space is $0.86\ eV$.

We conclude that there is an energy shift in the ground state of the H atom when it is inside a cubic box of perfectly reflective walls. However, this attempt to estimate the shift of $r_{eq}$ for the H atom inside a cavity was made according with some important considerations, from which we highlight:

- The H atom is described by two harmonic oscillators in quadrature only valid for circular orbits.
- The radiated power rate is not affected by the boundary conditions imposed by the Casimir cavity.
- It is valid to use a robust fitting of equation (22) in the computed $P^{abs}$ to predict the average $P^{abs}$ of an electron in a random motion induced by the ZPF.

## 3.6. Three-dimensional electron motion in the H atom

As an attempt to improve our previous work and the works performed by others [35][36], we developed a full three-dimensional model of the H atom in the SED framework. We implemented here the basic ideas and algorithm used in the previous simulations, described in section 2.2, and included some modifications discussed below.

According to our model, the electron can move in all directions, with no fixed plane restriction. The ZPF in our model is also fully generated in 3D, the **k**-vectors being distributed in a perfect cubic mesh according to the SED requirements in the case of a cubic cavity. This ZPF can be generated using the perfect box method described in section 3.1. Other innovation of this model is the inclusion of the magnetic part of the ZPF and its influence in the electron orbit, which may cause new features never seen before.

Besides that, this new model has a smaller number of approximations than the methods previously described. Still, we had to make some approximations. For example, the computational impossibility of generating an infinite number of waves forced us to generated only the waves resonating with all the radii between two limits, $R_{min}$ and $R_{max}$. Since we are running the code in a personal computer, which limits the computation time, we were forced to use again a window approximation. The frequency window ($\Delta\omega$) was however differently computed in comparison with the previous work. At this time, we made $\Delta\omega = f\Gamma{\omega_0}^2$, where $f$ is the proportionality constant and $\omega_0$ is the electron instantaneous angular frequency computed from its radius for a circular orbit, as from equation (15). $\Gamma$ is the same damping constant used in the harmonic damping oscillator described in section 3.2 by equation (12). $\Delta\omega$ here defined, contrarily to $\Delta\omega$ defined in 2.2.2, preserves the real resonance behaviour of the energy absorbed by the electron from the ZPF. $\Delta\omega$ was calculated assuming only circular orbits, however we also deduced $\Delta\omega$ based in the real damping constant of the differential equation (2). Nevertheless, our tests demonstrated that the difference in $\Delta\omega$ was minimal, so we maintain the circular orbit approximation for the $\Delta\omega$ computation. An example of a 3D plot of the electron position variation with time is shown in figure 17.

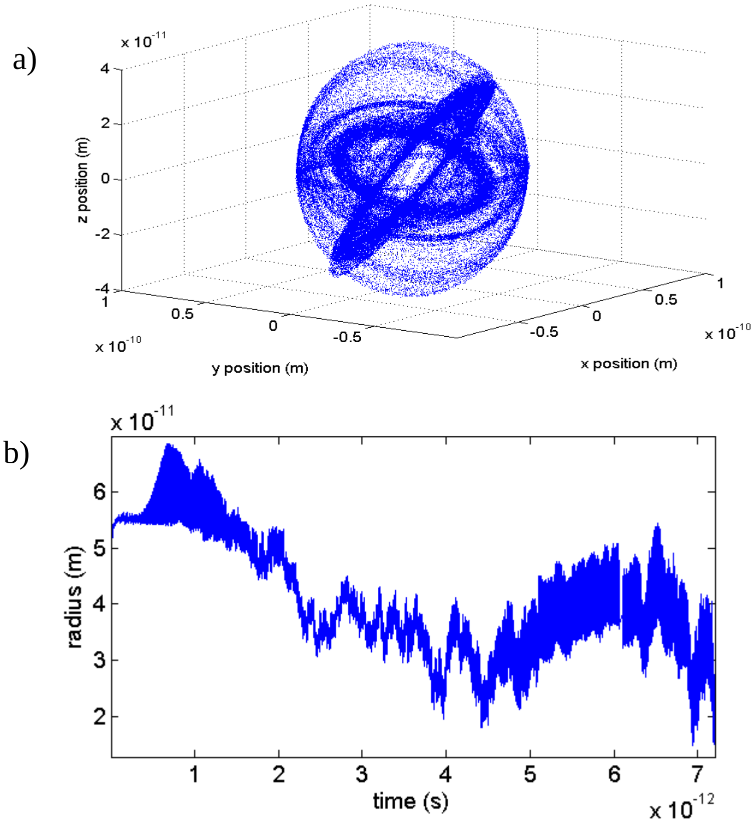

Figure 17: Plots of the electron motion behaviour simulated with our method. In this case the cavity was a cube of side = 200 nm, the simulated electron motion time was $7.1928 \times 10^{-12} s$. The $\Delta\omega$ used corresponds to $f = 2 \times 10^5$, $R_{min} = 10^{11}\ m$ and $R_{min} = 40 \times 10^{11}\ m$. a) Electron position distribution along time plotted in a 3D Cartesian space. Each blue point represents the electron position at each $6 \times 10^{-17} s$. b) Electron orbit radius as a function of time.

Although this method is more realistic, it is also computationally heavier. For big cavities, the code was almost impossible to run (in a personal computer) since the number of ZPF waves is huge. For small boxes ($L$ below a few microns), the code was possible to run according with our computational limitations, however taking a lot of time.

Our goal was first to have a coherent result (the electron radius distribution for the H atom similar to the one predicted by the Schrodinger equation) for the free space, validating this code. Next, we would like to compute the electron radius distribution inside cavities and estimate the ground state shift for different cavities. However, the enormous computational resources required by our model made impossible to run the code for the free space, and also impossible to accumulate enough statistics. Even so, our 8 simulations in small cavities have in common the tendency for the electron to be at a radius shorter than the Bohr radius for most of the simulation time. This seems to suggest that there is a shift induced by the small cavity.

In a time scale in the order of $10^{-12}s,$ we observed only a small deviation from the electron initial orbit plane. However, we believe that for longer time scales the position distribution would be aspheric like in the QM case.

We also evaluated the influence of the chosen $\Delta\omega$ in the electron behaviour. For this purpose, we used our model for three different frequency windows $\Delta\omega$. The corresponding plots of the electron radius as a function of time are shown in figure 18.

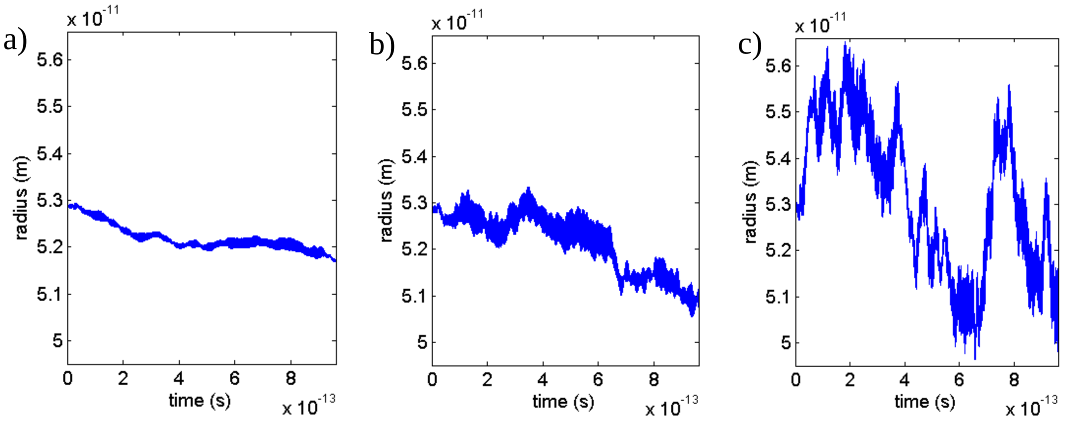

Figure 18: Plots of the electron orbit radius as a function of time, generated by our algorithm. The simulation was performed for $L = 1300 \times 10^{-9}\ m$, $R_{min} = 2 \times 10^{-11}\ m$ and $R_{max} = 40 \times 10^{-11}\ m$ . Three frequency windows $\Delta\omega$ were used, corresponding to: a) $f = 5 \times 10^2$; b) $f = 5 \times 10^3$; c) $f = 5 \times 10^4$.

As we can see, $\Delta\omega$ seems to play an important role since the fluctuation amplitude in the radius seems to increase as $f$ is increased. Even $\Delta\omega$ being thousands of times greater than the FWHM of the absorbed power resonance curve, the waves beyond the electron resonance frequency seem to have an important influence on the electron behaviour. This observation made us rethink the $\Delta\omega$ utilization. We demonstrated (in section 3.3) that the waves with frequencies away from the resonance frequency do not have a significant influence on the total power absorbed by the electron, at least for the classic harmonic oscillator. However, with this new approach, we suggest not using the window approximation in the future or using a wider window. Yet, it is possible that this strong influence of $\Delta\omega$ is only present for small cavities. This hypothesis arises from the fact that, in small cavities, the density of ZPF modes is lower, so near the resonance frequency there are only a few modes, whose influence is too small so that the influence of the farther modes begins to be more important.

## 3.7. Concluding remarks

In the present work we don’t consider the influence of the cavity on the atom radiated power. However, it is possible that the reflective walls of the cavity will reflect the emitted waves which may interfere with their self and also with the orbiting electron. The simulations we have made so far are valid for systems immersed in a modified ZPF. However, they may not be valid for a cavity since we don’t take into account the perturbations in the radiation emitted that is induced by the cavity. The paper of ref. [37] studied the spontaneous emission of the harmonic oscillator inside cavities in the SED realm. The paper suggests that the radiation damping term, $\Gamma{\omega_0}^2$ in equation (13), is affected by the reflective cavity walls. This conclusion was deduced for a harmonic oscillator inside two parallel conductor plates resulting in two modified damping constants, one for the perpendicular orientation between the oscillator and the plates and the other for the parallel orientation. It was also suggested that, taking into account the modifications induced in the damping term and in the ZPF, the ground state harmonic oscillator between two mirrors would preserve its free-space energy. However, excited states would acquire different cavity-induced properties. It is even affirmed: “If the atom stays for a long time inside the cavity some states are "eliminated" because they become more unstable, while other states acquire the status of "stable states".”. This supports our hypothesis (better explained in the following chapter) of radiative shifts between the ground and modified exited states.

Both methods used by us (discussed in sections 2.2 and 3.6), in addition to not taking into account the waves reflected back from the cavity walls, have shown some instability problems, mainly the ones discussed in section 2.2.3. Therefore, as suggested in 2.2.3, something else could be necessary to achieve the atom stability, for example to account for the inner structure of the particles as suggested in ref. [28]. This inner structure will allow storing energy in the freedom degrees of this subatomic structure. The stored energy is dynamically exchanged between the electron and the inner structure, leading to a feed-back mechanism capable of maintaining the atomic stability. We are also working in collaboration with Rodríguez (author of ref. [28]) to adapt our algorithm in order to accomplish this substructure. However no relevant results were achieved so far.

# 4. Method to extract energy from ZPF

At this stage the reader could still be a little sceptical about the idea of extracting energy from the vacuum. “If the vacuum is the lower state found in the universe how is it possible to extract energy from it?” However, as the reader should already understand, the vacuum is not all the same, and it’s possible to create a region in the space where the vacuum energy is lower than in the free space. This region could be a Casimir cavity, where some electromagnetic modes are vanished. From general physics it is known that, in order to have an energy flow, there must be an unbalance between two regions, and thus the energy can flow from the most to the least energetic region. Even so, most of the times it is needed to provide some kind of circuit for the energy to flow. For example, if we place a Casimir cavity in the space, nothing will happen because the excess of modes in the outside does not flow to the inside as they are not allowed there. We need a mechanism to transport the outside energy to the inside. This mechanism must in equilibrium with the vacuum outside, exchanging energy with it continuously. If we pull this mechanism inside it will drag some of the outside energy. However, inside the Casimir cavity, the equilibrium with the inside vacuum is no longer present and consequently the excess of energy will be released and the equilibrium with the medium will be restored. Finally, in the energy releasing process, the energy will be transmuted in a form that could be distinguishable of the ZPF and then collected and used by our apparatus.

In this chapter, we start by presenting the basic concept to measure the atomic energy shift induced by a Casimir cavity and review the state of the art, describing a method available in the literature. We then consider new improvements to the method, and finish with some considerations needed to apply the initial concept to an experiment in the real word.

## 4.1. The Proposed Method

### 4.1.1. Earlier work

Recently (2012), a paper by Dmitriyeva and Moddel [8] reports an experimental work where different gases are passed through Casimir cavities and the emitted radiation is collected. To simulate the Casimir cavities, they used nano-porous membranes (Whatman polycarbonate Nuclepore track-etched flexible membranes with pore sizes of 0.1, 0.2, and 0.4 μm) coated with gold by thermal evaporation. These membranes were mounted in a stainless-steel vacuum system where a wide bandwidth SPH-49 pyroelectric detector from Spectrum Detectors Inc. was used for the radiative output measurements. This detector has a sensitivity of $1{,}9 \times 10^4\ V/W$ almost constant in the wavelength range from 0.6 to 5 μm, so mostly in the infrared (IR) region. The flow was also modulated (at 0.5 Hz) by closing and opening a valve connected to a mechanical vacuum pump. The pressure inside the chamber was kept in the range 1-10 torr. Different gases (Ar, Xe, He and $N_2$) were used with gold-coated and uncoated membranes, with the flow rate also changed. Data have shown that, as the flow rate increases, the radiation collected also increases, as expected. However, more radiation emitted was expected to be observed for the coated membranes[12] and these experiments revealed more radiation intensity for the uncoated membranes. The authors expected more radiation to be emitted for heavier atoms (such as Xe) since the valence electrons have more external orbits and consequently their orbit frequencies should be lower, and so inside the cavities the modes closer to the resonant frequencies of these orbits are more suppressed relative to the case of lighter atoms, as discussed in section 3.5.1. Nevertheless, and contrary to expectations, the experimental results obtained in [8] have shown that more radiation was emitted for lighter atoms.

### 4.1.2. Improvements to the earlier work

The present work can be seen as an attempt to continue and improve the study presented by Dmitriyeva and Moddel [8]. In this section, we will point out some possible problems present in the earlier work and propose some modifications:

1. First of all, as discussed in ref. [8], the main problem was the impossibility to separate the background from the hypothetical radiation emission caused by the ground state shift of the atoms. A variety of possible physical effects may origin emission of radiation in the infrared region at room temperature. In this way, we propose to make a spectroscopic study of the radiation emitted. If all the cavities have the same diameter, the ZPF inside the cavities will be equal (the same suppressed modes), then we would expect the shift in the ground state to be roughly

---

[12] The metal coated membranes constitute a better approximation to the Casimir condition. However, Lifshitz has shown that the fundamental effect exists also for any dielectric materials [25].

the same, and for the same gas and membrane we would observe in a spectroscopic analysis a Gaussian distribution with centroid in the wavelength corresponding to the energy shift characteristic of this specific atom and cavity diameter[13].

2. Second, if necessary we can try to use membranes with pores of smaller diameter to increase the energy shift of the ground state and so decrease the emitted light wavelength towards the visible or UV region, making it easier to distinguish this radiation from the background.
3. Another improvement that should increase the irradiated energy is the use of excited states instead of ground states. In the classical realm, the excited electrons travel in the outermost orbits, corresponding to lower angular frequencies. So the same cavity could induce a bigger shift for excited-state electrons than for ground-state electrons. We expect this behaviour because inside a cavity there is a smaller number of modes near the orbital frequency for an excited-state atom. This hypothesis is sustained by the study made in section 3.5.1.
4. It is possible that the radiation correspondent to the ground state shift is also a forbidden mode inside the cavity. So if the atom cannot radiate, it could persist in the energy level of the ground state outside the cavity, which would correspond to an excited (of infinite lifetime) state inside the cavity. To solve this failure we propose a more complex method. We need then to give to the system some energy so that the system will release the supplied energy plus the shift. A more detailed explanation of this method is presented in section 4.1.3.

### 4.1.3. Discussion of the two possible scenarios for the level shift mechanism

If our main hypothesis of the atoms undergoing an energy level shift (in the ground or excited state) inside Casimir cavities is correct, then a crucial question persists: Is this shift instantaneous (progressive in a small time scale) or will the atom remain in an excited state until it decays by some mechanism (such as spontaneous emission)? This question influences the experiment that we will carry out and we consider here two different options:

1. The ground state of the atom in the free space can behave as an excited state inside the cavity, thus it would keep the outside ground state for a period of time and

---

[13] However, here we discriminate the wall-atom interaction. Since the Casimir-Polder and van der Waals interactions also induce energy shifts and these shifts have a great dependence on the wall distance, a narrower spectrum can be observed from the radiation emitted from atoms at different distances to the walls.

only then decay to the cavity ground state (similar to the spontaneous emission). In Ref. [8] it is suggested that the ground state atoms could enter the porous cavity and undergo a level shift to the cavity ground state only when they interact with the walls. This applies also to the excited states, so when the atom in an excited state enters the cavity, it decays by spontaneous emission, from the outside excited state to the cavity ground state, emitting radiation with energy equal to the ground state shift plus the energy of the excited state in the free space transition.

2. If we look close to the SED theory, and consider an electron in a planetary-like orbit, in the absence of resonant ZPF modes it will decay in spiral as a consequence of the Abraham–Lorentz force, releasing radiation according to its instantaneous radius. This argument leads us to think that a change in the atomic level will be progressive when the resonant modes disappear, still it will look like an instantaneous reaction[14]. This applies to both ground and excited states. Then, if an atom in an existing state enters the cavity, its excited state undergoes a shift and, when the atom decays by spontaneous emission to the cavity ground state, it will emit radiation with energy equal to the difference between the cavity excited state and the cavity ground state. This energy will be smaller than the correspondent free space transition, since the energy shift of the excited level is higher than the energy shift of the ground state.

### 4.1.4. Our concept to extract energy from the ZPF

The first and the simplest experimental study we suggest is to pass atoms in the ground state through Casimir cavities and to analyse the radiation emitted. We propose to make a spectroscopic analysis for a fixed cavity size to test the hypothesis that the spectroscopic emission has a specific pattern resulting from the constant ground state shift. To compare and subtract the background, we should study the effect without cavities, with non-coated cavities and with metal-coated cavities. This spectroscopic analysis could be done in the IR region, however the problems described in 4.1.3 could interfere. So a spectral analysis in the visible and ultra-violet (UV) regions for different cavity sizes will be preferential. In our experiment, we intend to make a UV-visible analysis (160 to 550 nm) of monoatomic and polyatomic gases passing through aluminium coated porous membranes (0.4, 0.1 and 0.05 μm).

---

[14] If we remove the ZPF of an electron in the H atom at the Bohr radius, it takes approximately $1.2 \times 10^{-11}\ s$ to reach the nucleus, so we consider these decays as instantaneous.

According to classic mechanics, an electron in an excited state (where we consider planetary-like orbits) has a bigger orbit, and so a lower angular frequency relative to its ground state. Thus, for the same cavity, we expect a larger shift in the excited state than in the ground state, since there are more suppressed modes near the resonant frequency in the case of the bigger orbit as demonstrated in section 3.5.1. Hence there will be a negative shift in the transition energy.

For each of the two possible decay channels suggested in section 4.1.3, we propose a different method to extract the energy from the vacuum.

For hypothesis 1, the atom is first excited to a resonance state, then goes inside a Casimir cavity in such a way that it decays there by spontaneous emission. As we expect the final state to be the shifted ground state, the energy of the radiation released would be the free space resonance transition energy plus the energy difference between the outside ground state and the cavity ground state. Once the atom goes out the cavity the ZPF reenergises the cavity ground state back again to the outside ground state. An exemplifying scheme of the concept is presented in figure 19. An important aspect in this scenario has to be taken into account, the spontaneous emission rate inside a Casimir cavity, or close to a reflective wall, is modified. This interesting behaviour related with the van der Waals and Casimir-Polder forces was predicted by QED [25] and SED [37], and was also observed experimentally [41]. An excited state can acquire a lifetime 20 times longer than the lifetime in the free space [37], so the atoms will need to stay longer inside the cavity to decay. There is also a hypothesis that the outside excited state decays to the cavity excited state by spontaneous emission, releasing an energy equal to the energy difference between the states. This emitted radiation would be much less energetic, so harder to detect.

For hypothesis 2, where we consider the decay to be instantaneous, the atom goes inside the cavity, where its ground and excited states undergo an energy shift, the excited state shift being larger than the ground state shift. Then we can excite a specific state inside the cavity with a small amount of energy relative to the energy needed in the free space. Once excited, the atom goes out the cavity and the ground and the excited states undergo again an energetic shift. When the atom decays by spontaneous emission in the free space, it releases an amount of energy larger than the one used to excite it. When the atom enters the cavity, it radiates the energy difference between the shifts, either if it enters in the ground state or in the excited state. Figure 20 exemplifies this process.

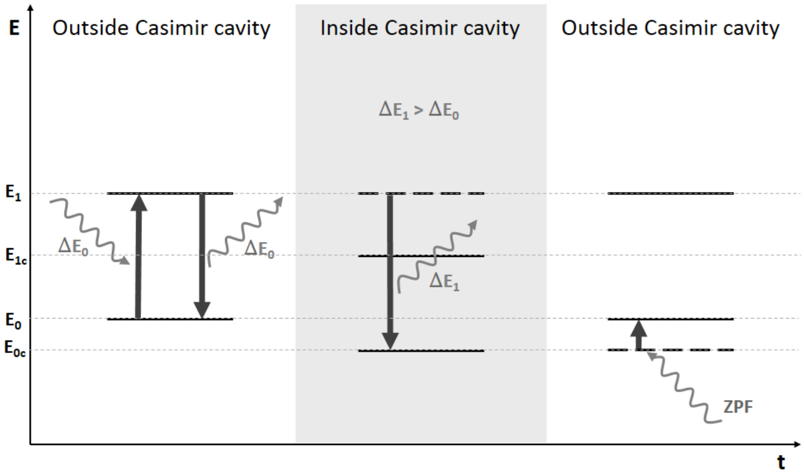

Figure 19: A two-level atom in the free space has a characteristic transition energy $\boldsymbol{\Delta E_0}$. Inside the cavity, the ground state undergoes an energy shift from $\boldsymbol{E_0}$ to $\boldsymbol{E_{0c}}$, releasing by spontaneous emission an energy $\boldsymbol{\Delta E_1}$ greater that $\boldsymbol{\Delta E_0}$. Again in the free space, the ZPF reenergises $\boldsymbol{E_{0c}}$ back again to $\boldsymbol{E_0}$. Considering the hypothesis of the transition between the excited states outside and inside the cavity, the energy released will be $\boldsymbol{E_1 - E_{1c}}$.

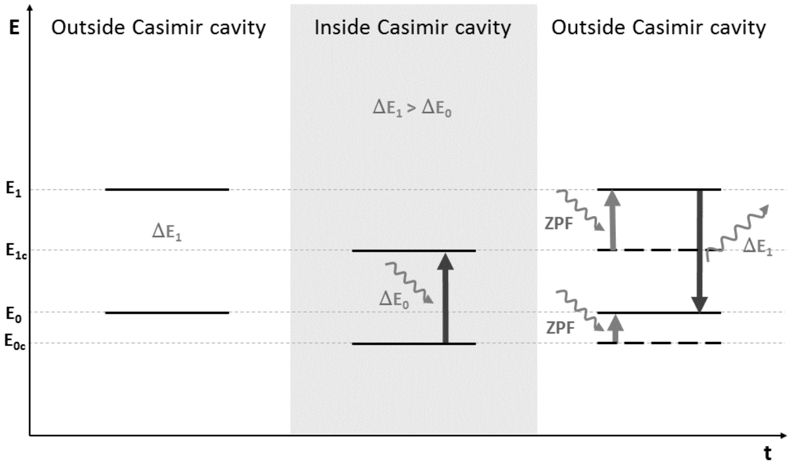

Figure 20: A two-level atom in the free space has a characteristic transition energy $\Delta E_1$. If we irradiate the atom with an energy $\Delta E_0$ lower than $\Delta E_1$, the atom is not excited and remains in the ground state. However, inside the cavity, the ground and excited states undergo an energy shift from $E_0$ to $E_{0c}$ and from $E_1$ to $E_{1c}$, respectively. Thus it is possible to excite the atom with $\Delta E_0$. When the atom goes outside the cavity, the ZPF reenergises both the excited and ground states, and by spontaneous emission the atom releases an energy $\Delta E_1$ greater than $\Delta E_0$.

In any of these two cases, we observe a gain of energy between the energy provided and the one released, the ZPF being the source of the excess energy.

Another interesting method related to the one proposed by Puthoff [29], and addressed in section 1.3, is based on the ionization and molecular dissociation energy shift. According to SED (at least with the approximation made in the present work), an atom in the ground state (or in an excited state) should have ionization energy larger inside a cavity than in the free space. So the idea would be to first ionize the atom and then, when it goes inside the cavity and captures a free electron, it would emit an amount of energy larger than the one used to ionize it in the beginning.

The use of molecules instead of single atoms would be maybe more accessible experimentally. If the molecules in the ground state were inside the cavity, where the vibrational resonant modes are suppressed (all or some of them), we would expect that the molecule dissociation energy would be greater than in free space. Thus we could dissociate the molecules before they enter the cavity and, once inside, if they recombine they could emit radiation more energetic than the one used to dissociate it in the beginning.

## 4.2. Considerations for the implementation in the real world

Until now, we made a series of proposals and estimations, but unfortunately they are, together with the computations of the energy shifts for the H atom performed in chapter 3, difficult to transpose to the real world. The reader should understand that we are working somewhat blind, since SED is still a very immature theory. In the literature, the works in this area are scarce and the few that exist are essentially conceptual and don’t have in consideration the limitations imposed by the materials or the instrumentation properties. Hence in this section we try to point out some facts that could influence our theoretical assumptions.

In chapters 2 and 3, we have studied the H atom, which is the simplest case. The heavier atoms have more electrons, thus one more term to account, the Coulomb force between the electrons. Consequently, the orbits will be more complex, with the possible arising of very exotic geometries, like in the case of the orbitals predicted by QM (orbitals p, d, f, etc.). Furthermore, the model discussed here does not take into account the electron spin (as in the SEDS case), which could change our actual scenario.

### 4.2.1. Reflectance of Casimir cavity walls

Metals are not perfectly reflective to the electromagnetic radiation and the reflectance is also dependent on the angle of the incidence and on the wavelength [42]. The penetration depth[15] is an important parameter and also varies with frequency, being

---

[15] Depth in a material for which the intensity of an incident wave decays to 1/e of its original value [42].

around 20 nm for an incident wave of wavelength 200 nm, for typical metals [42]. These parameters will influence our theoretical model, where we considered a perfectly reflective cavity.

The Casimir condition (a small cavity with perfectly conductive walls) is hard to accomplish in the real world, still we should try to make the best approximation.

In typical metals, if we treat the electrons as free particles, they will move according to the frequency of the incoming electromagnetic wave and then this wave will be reflected. However, above the metal plasma frequency, the electrons cannot move quickly enough to reflect this incoming wave [42]. So the metals are not good reflectors for higher frequencies, which could propagate inside a cavity even if its size is small enough to suppress them. Thus, even if we continue decreasing the cavity size, the metal reflectivity will impose a limit (related to the metal plasma frequency) on the perturbation caused by the ZPF.

In order to suppress the largest amount of normal modes inside the cavity we should use for the Casimir cavity wall a highly reflective metal whose reflectance extends to higher frequencies. The reflectance as a function of the incident radiation wavelength for various films made of gold, silver, aluminium, copper, rhodium and titanium is presented in figure 21.

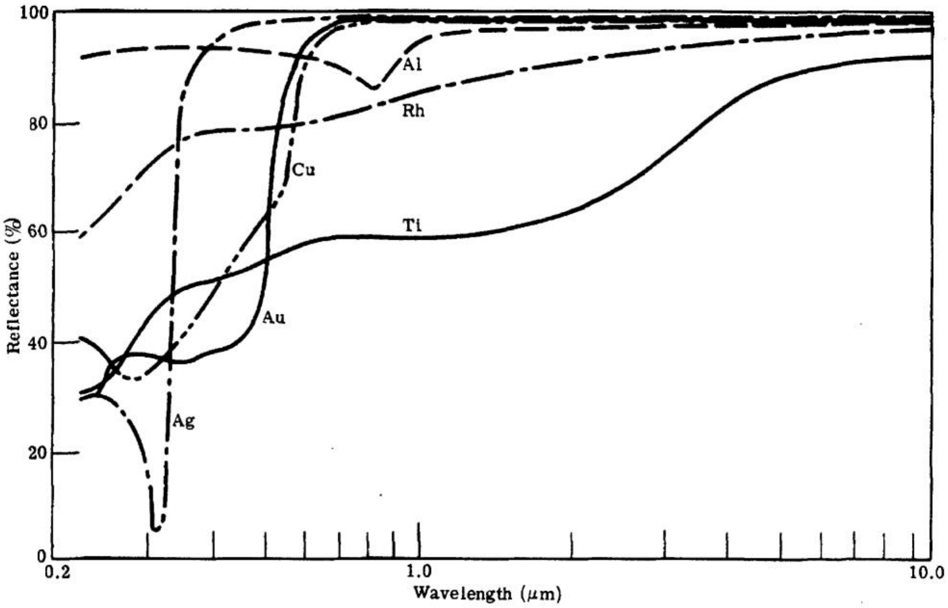

Figure 21: Reflectance of films of gold (Au), silver (Ag), aluminium (Al), copper (Cu), rhodium (Rh) and titanium (Ti) as a function of the incident radiation wavelength [43].

Aluminium is the best choice for the cavity wall since it is the most reflective metal in the UV region[16]. Gold is often used in Casimir experiments (for example refs. [18] [19]) since it has a high reflectance, almost 100%, but only for lower frequencies. As these experiments made studies with walls of thicknesses in the μm range, which suppress only the wavelengths longer than the ones in the IR region, the gold coating was a good option. However, for the nanometre scale that we intend to explore in this work, Al is the most suitable choice.

### 4.2.2. Geometry and orientation issues

The computer simulations of chapter 3 were performed for cubic cavities. However it is more practical to pass gas atoms through a structure with a small aperture or by a narrow tube. In these cases, the ZPF is only perturbed for the modes that travel in directions orthogonal to the walls. In this way, the influence in the average atomic orbit will depend on the orbit orientation. As we have seen in section 3.6, the deviation of an electron from the initial motion plane is almost negligible, at least in the time scale investigated. So, if we consider its orbit restricted to a fixed plane, the atom self-rotation will define the orbit orientation.

An atom in random linear and rotational motions, as in a gas molecular flow, will be affected by the ZPF perturbations according to its instantaneous orientation. This scenario is hard to predict; however, we expect that there will be an observable average energy level shift even inside a narrow Casimir tube, instead of a box.

---

[16] In addition to figure 21, the Aluminium reflectance is approximately constant down to $\sim 80\ nm$, where it drops abruptly. Other metals such as Copper, Platinum, Chromium, Silver and Gold already have a reflectance lower than 20% at $\sim 90\ nm$.

# 5. Experimental apparatus

In this chapter we start by describing the basic concept of our experiment and then we give technical information about each component of our system and about the data acquisition instrumentation.

## 5.1. General Description

In section 4.1 we suggested and described some methods for extraction of energy from the ZPF. Now we propose an experimental apparatus to implement some of these methods.

The main idea of the methods proposed is interchanging atoms between the free space and a Casimir cavity. To materialise this concept, we flow gases (monoatomic and molecular) through a nano-porous membrane coated with aluminium. Since we are using gases, to reach an appropriate level of purity we designed and built a vacuum stainless steel system. Besides providing the necessary vacuum, this system allows the gas flow through the porous membrane. To analyse the spectrum of the radiation emitted we use a monochromator coupled to a Photomultiplier Tube (PMT). For the tests where we need to radiate a specific wavelength, we use another monochromator coupled to a lamp that emits in a continuous spectrum. This apparatus allow us to study almost all the hypotheses proposed in section 4.1.4. Figure 22 shows a simple schematic of our apparatus.

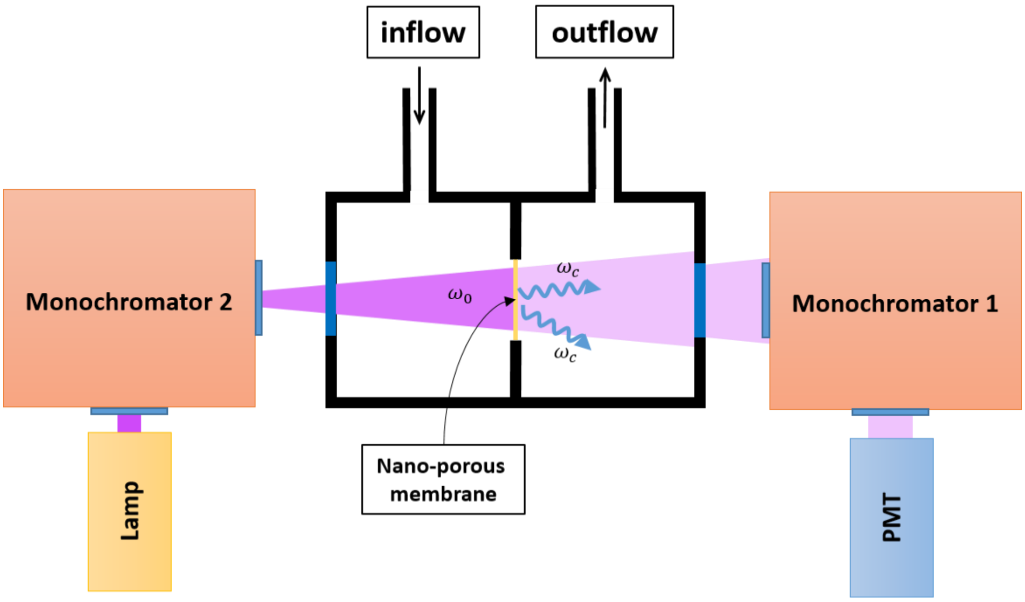

Figure 22: Simplistic schematic of our experimental apparatus. The black lines represent the main chamber where the gases are circulated. The blue rectangles represent optical interfaces. Two $MgF_2$ windows, 3 mm thick, were used between the main chamber and the monochromators . $\omega_0$ is the central frequency at the output of Monochromator 2 and $\omega_c$ represents the frequencies of the radiation emitted by the atoms which undergo a cavity-induced level shift, which can have origin inside the cavities or at the exit.

### 5.1.1. The nano-porous membranes

A Casimir cavity is a region in space where some of the ZPF modes are suppressed. Modifying the ZPF is trivial, in fact all the matter induces local perturbations on the ZPF, however between two conductive and neutral walls the perturbation in the ZPF is greater, mainly for the ZPF waves that propagate orthogonally to the walls. Pores with a cylindrical form are even better than a pair of walls, since they suppress the modes that propagate in two perpendicular directions. Hence, the use of a membrane with numerous holes whose internal walls are coated with a metallic layer could be a good choice.

We used in our experiment Nuclepore Track-Etched Polycarbonate membranes from Whatman (supplied by GE Healthcare Life Sciences). These membranes, mostly used as filters for fluids, have discrete pores sharply defined, high flow rates, and excellent chemical and thermal resistances. They are fabricated from a thin film of polycarbonate through a combination of charged particle bombardment (or irradiation) and chemical etching. They have a thickness of only 7 to 20 μm but burst strength larger than 10 psi (0,69 bar), which is more than enough for our applied differential pressure. The maximum operation temperature is 140 °C, which allows for thermal evaporation without deformation risk. Its porosity (void volume) lies in the 4-20% range, and the pore density lies in the range of $10^5$ up to $6 \times 10^8\ \mathrm{pores/cm^2}$.

We got three different types of membranes, with pore diameters of 0.05, 0.1 and 0.4 μm. We assembled them in copper supports using a low outgassing epoxy glue to prevent any gas flow other than the one flowing through the pores. In figure 23 we can see a picture of a membrane glued to the copper holder.

The process used to coat the membranes is thermal evaporation with aluminium. To coat the maximum depth into the pores we made four evaporations, placing the membrane in four different angles of 45º. The faces of these membranes are slight different, one is perfectly planar and the other is rougher, and we coated only the planar face.

Figure 23: Uncoated membrane glued onto a copper support which is itself mounted on a vacuum system piece (center-ring support KF-25).

To verify the existence of nano-pores, to confirm its size, uniformity and density, we analysed a membrane of pores with 100 nm diameters with a scanning electron microscope (SEM). The results are shown in figure 24.

As expected, the membrane has well distributed pores with a large density, and their sizes are according to the specifications.

### 5.1.2. Monochromators

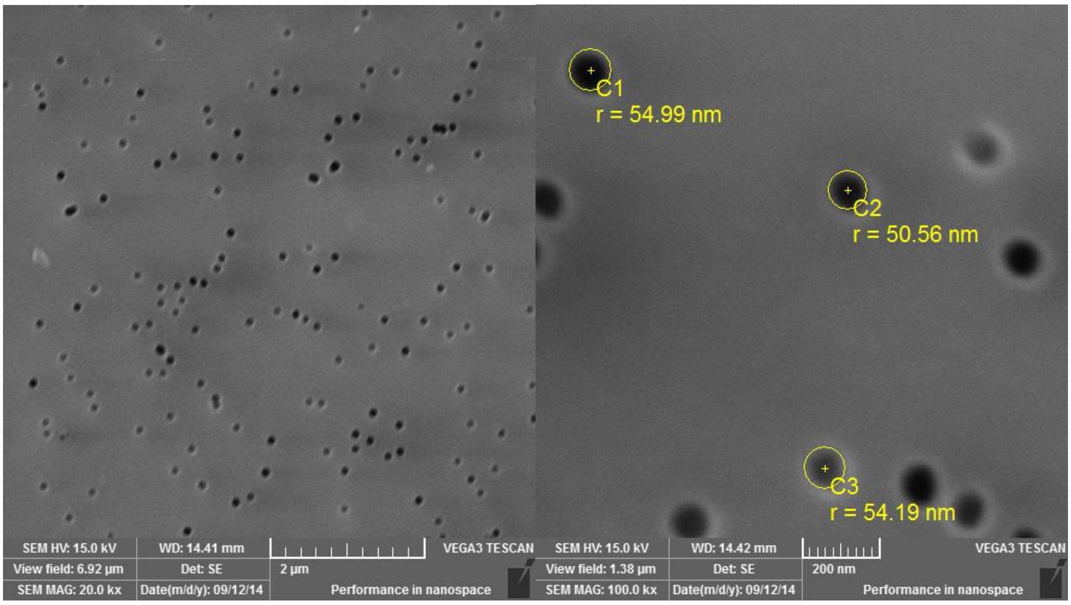

Figure 24: SEM photos from a membrane of pores with diameter = 100 nm. The planar face of the membrane, coated with 40 nm of palladium, is shown. The right photo was taken with a magnification of 20000× and the left photo with a magnification of 100000×.

To irradiate the main chamber and to analyse the radiation emitted two monochromators (MC) were used, both of them from ACTON ARC, Model VM-502. They are nominal 0.2 meter evacuable monochromators with an optimum wavelength range in the vacuum ultraviolet region. The grating mounted in both the MCs is a standard 1200 G/mm, which allows a wavelength range 30 - 546 nm (approximated values). The focal length is 0.2 meters, the aperture ratio f/4.5 and the grating coating is made of Aluminium and $MgF_2$.

One MC (from now on named MC1) was used as spectrum analyser and its step-motor controlled by the ACTON SpectraDriver-SD3. This controlling device allows the MC operation to be controlled by software, which is very practical. The other MC (named MC2) was used to irradiate the membrane and is controlled by the ACTON SpectraDrive-SD, equipped with a display and a keypad allowing the MC operation. Both the controllers allow specifying the scanning rate and the wavelength range.

It is recommended by the manufacturer that for spectroscopy in the VUV region (less than 200 nm wavelengths) the MC should be evacuated at least down to a pressure of $6.7 \times 10^{-4}$ mbar.

The light entrance and exit flanges of the MCs have slits, vertical (internally adjustable) and horizontal (adjustable outside by a micrometre scaled knob). The horizontal slits have the important task of controlling the MC resolution. The narrower this slit is the better will be the MC resolution. However the light intensity is also smaller and for our purposes it may be necessary to maximize the light collected or emitted. Thus we needed to find the best compromise between the light collection/emission and the resolution required. The entrance and the exit slits have influence on the resolution, and the best compromise was found to be when they are the two equally open. So, whatever the required resolution is, the entrance and the exit slits must have the same gap, this is true for both the horizontal and vertical slits. Although less significant, the vertical slits also influence the MC resolution. Preliminary tests with our system have shown that the better compromise for the vertical slits is achieved for MC1 and MC2 entrance and exit slits with $2\ cm$.

### 5.1.3. The gaseous chamber and the vacuum system

The main chamber, where the membrane is mounted, is made of stainless steel and is composed of three parts. Two of them are symmetric in order to adapt to the entrance/exit of the MCs. Each of these pieces was designed by us (using Autodesk Inventor software) and is formed by a flange (that couples to the MC) soldered to a KF25 tube with the respective flange in the opposite side.

The KF25 tubes were made the shortest possible ($\sim 35\ mm$) in order to minimise the membrane-MC distance and therefore maximize the solid angle. The flanges that couple to the MC have an opening ($26\ mm$ diameter) that allows the light to pass through. In order to hermetically isolate the MC from the chamber, we used an $MgF_2$ window sealed with two Viton o-rings placed between each MC and the chamber. We chose this material ($MgF_2$) because it has a transparency above 80% for wavelengths down to 160 nm, where it starts to slightly decrease, reaching 60% at 120 nm.  To each of the symmetric pieces that compose the chamber we soldered a Swagelok flange (VCR ¼ inch) that will couple to the vacuum and the gas flow system. The third piece of the main chamber is a bellows or flexible coupling tube (minimum length $\sim 5\ cm$), which helps the assembling and alignment between the two MCs. The bellows is connected between the other two pieces by centring-rings. The membrane, assembled in the KF25 centring-rings shown in figure 26, is pressed between the flexible coupling tube and the KF25 flange of one of symmetric pieces (the one closer to MC1). A schematic representation of our system is shown in figure 26 and a photo of the system is shown in figure 25.

Figure 25: Photo of part of our experimental system, showing the two MCs, the main chamber, part of the data acquisition instrumentation and part of the vacuum system. The vacuum gauges and pumps are not visible.

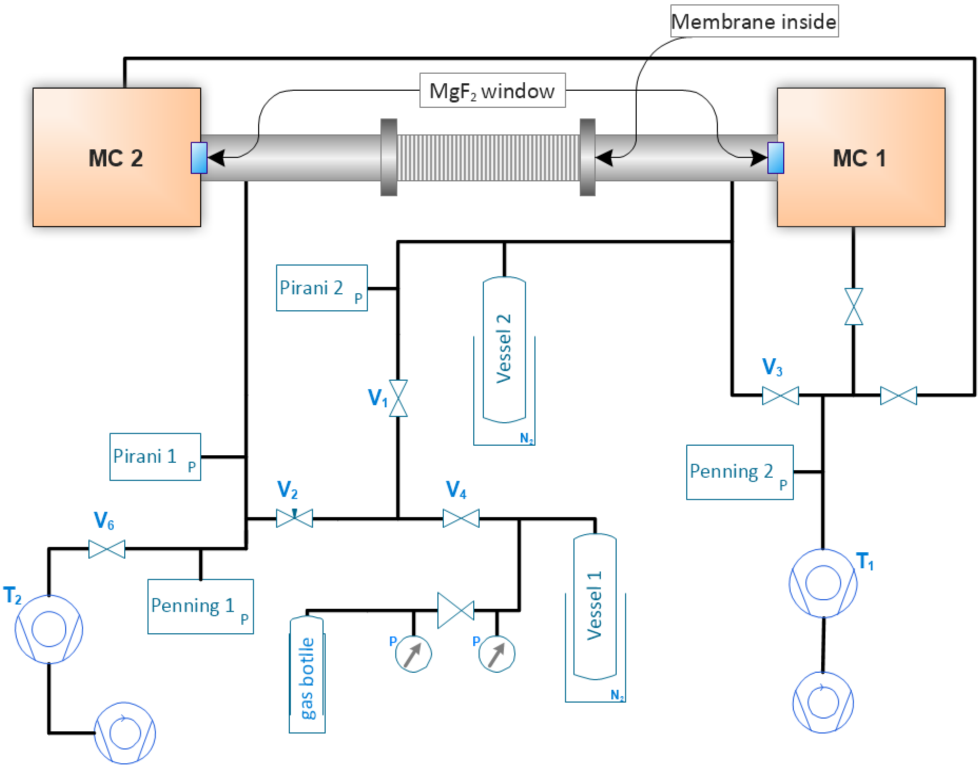

Figure 26: Scheme of the vacuum and gas flow system. In grey, the main chamber is shown (composed by the two symmetric parts and the bellows described before), while the orange boxes are the monochromators MC1 and MC2. In blue, we show the vacuum equipment and the black lines are vacuum tubes. The distance between the two MCs is 14 cm. The distances from the membrane to MC1 and MC2 are respectively4.5 and 9.5 cm.

The vacuum system is composed by two turbo-molecular vacuum pumps ($T_1$ and $T_2$, each one coupled to a rotary pump). $T_1$ evacuates the two MCs and a part of the remaining vacuum system. Before filling the gas, the vacuum system is first evacuated with the two pumps simultaneously pumping. For this purpose, the reduction-valve (at the exit of the bottle) is closed and the rest of the valves in the system are open. This task requires some caution since the differential pressure between the two sides of the membrane can damage it.

To place the gas inside the system valve $V_4$ is closed and, through the reduction valve (the one immediately following to the gas bottle), the volume between these two valves is filled (including vessel 1).

To make the gas flow through the membrane, the valves connecting the vacuum system to the pumps ($V_6$ and $V_3$) are closed. Note that the two MCs can continue being evacuated by $T_1$, which is crucial to keep low levels of air inside the MCs during our experiment. Then, to isolate the two sides of the membrane, valve $V_1$ is also closed. To collect the gas after it passes through the membrane, vessel 2 is submersed in liquid nitrogen ($LN_2$). $V_4$ is also completely open and the needle valve ($V_2$) allows controlling the gas flow through the membrane. Pirani 1 and pirani 2 give us information about the differential pressure between the two sides of the membrane. We use this information to estimate the relative[17] gas flow through the membrane. Finally, to recollect the gas in vessel 1, valve $V_1$ is open and the nitrogen is changed from vessel 2 to vessel 1, leading to gas liquefaction in vessel 1. The gas can be stored in this volume by closing valve $V_4$.

### 5.1.4. The Light source

The light source used is an ACTON product, ARC Model DS-775 Deuterium Light Source. The useful wavelength range of this source is from 115 nm to 370 nm, with a continuum from 165 nm to 370 nm and many lines from 115 nm to 165 nm. Physically this device is very compact and couples perfectly to MC2. The beam section is approximately 1 mm in diameter and is located 10.16 cm away from the MC2 entry flange. The source has a typical Lyman-alpha radiance of over one miliwatt per $mm^2$-nm-steradian. In figure 27, the lamp output spectrum is plotted, as given by the manufacturer. The highest line corresponds to the Lyman-alpha line of deuterium (the theoretical value

---

[17] We are not capable of measure with precision the nominal flux rate since our pressure gauges are not precise neither properly calibrated for the gases used.

is 1215.31 Å [44]). This resonance line will be used to calibrate the offset of the MC grating

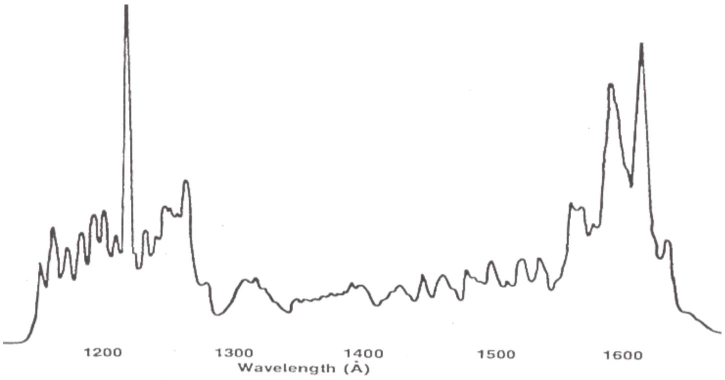

Figure 27: Relative throughput (uncorrected) of the ARC VUV Deuterium Source, through the VM-502 MC (100 micron slits) and the RSC-100 Vacuum Reflectometer, as a function of wavelength. This image comes from the device manual.

### 5.1.5. PMT and data acquisition

The PMT used is model R8020-06SEL manufactured by Hamamatsu Photonics. It is equipped with a bialkali photocathode and it has low radioactivity, active area of 26 mm$^2$, 10 stage dynodes and a head-on type synthetic silica window. Its spectroscopic response lies in the range from 160 to 650 nm. The cathode sensitivity is typically 100 μA/lm and the quantum efficiency at 175 nm is 30%. It was assembled in an E10411MOD Hamamatsu socket with maximum voltage +1000 V and a divider current of 364 μA (at +1000 V).

The PMT was polarized by a HV-board (NHQ-206L). The PMT signal was collected by a Canberra 2005 pre-amplifier and then amplified in a Tennelec TC 243 linear amplifier and digitalized in a Nucleus multi-channel analyser (MCA) connected to a computer, where a graphical interface allows to visualise the pulse height distribution. The best choice of the amplifier parameters to distinguish photons counted from the noise level was found by visualizing the plots in the MCA. The coarse and fine gains were respectively 100 and 5 and the peaking time was 1 μs, while the PMT socket polarization was 950V. The pulses were also visualized in a Tektronix TDS 210 oscilloscope.

Nucleus is the native MCA software and it is possible to program it for continuous multi-acquisition. For example, Nucleus can acquire without interruption 1000 spectra of 1 second each (the minimum acquisition time). These spectra were saved in independent files (*.spm* extension). These files can then be converted to ASCII format (using the software Specon 2000 v1.3) and thus easily handled using MATLAB. The number of acquisitions and the acquisition time should be chosen according with the MC scanning range and rate in such a way that the MC and the Nucleus start and finish at the same time. Subsequently an algorithm (SpeGen) was developed in MATLAB that, for each file, countsthe number of photons collected,  and plots the spectrum of the light collected as function of the wavelength.

This method requires the perfect synchronization between the start of the Nucleus acquisition and the MC operation. However, even if the two systems start with a delay of for example half of a second, in the worst scenario (when the scan speed is the highest, 10 nm/s) the error in the spectrum will be 0.083 nm, which would mean a constant shift of 0.0083 nm in the entire spectrum relative to the true values.

### 5.1.6. Gases choice

The gas used in a first stage should be a noble gas for two reasons: noble gases are inert so they won't react with other materials and, therefore, their handling is very simple; usually they are monoatomic gases so at proper pressures we have a clean line-type absorption/emission atomic spectrum.

Since we intend to study some specific atomic transitions, we must eliminate all the possible light emission in other wavelengths. Then we must reduce any decay channel other than the resonance fluorescence. This can be accomplished by reducing the gas pressure to a few mbar [45].

In a next stage polyatomic gases may also be used to study the molecular bound energy shifts induced by Casimir cavities.

## 5.2. COMSOL Multiphysics simulations

To better understand the behaviour of the electromagnetic radiation incidence in the porous membrane and the flow of gas molecules through the membrane, we made some simulations using the COMSOL Multiphysics software.

### 5.2.1. Gas flow dynamics

As we intend to use low pressures (up to a few mbar), for nanometric pores we believe that the gas flow will always stay in the molecular flow regime. Our membranes have 50, 100 and 400 nm pore-diameters, so we will consider the bigger ones to estimate the maximum pressure at which it is still valid to consider a molecular flow. We want to confirm if in our system we will always have a molecular flow and then make the simulations accordingly. In agreement with ref. [46], we can use the Knudsen number (which relates the molecule mean free path with the pipe diameter) to estimate if a flux is in the molecular or viscous regime. Considering the pores as pipes of diameter 400 nm and the gas molecules with diameter 216 pm (xenon atomic diameter [47]) at room temperature, we found out the maximum pressure at which the molecular flow regime is still valid to be ~496 mbar. As we will use much lower pressures, we will consider the gas flow through the membrane to be in the molecular regime.

Hence we simulated the gas atoms considering them as free particles and tracking each atom. Thus, they obey to the Newton classic laws of motion with initial and after-collision random velocities and orientations (Monte Carlo method). Some other approximations were made: the model follows the Kinetic Molecular Theory, the particles don´t collide with each others and the simulation was made in two dimensions. The molar mass of the gas is 28 g/mol, the temperature is 25ºC and the pressure 100 Pa (1 mbar).

Our main purpose here is to estimate the average time for an atom to cross the membrane, so we idealize the worst porosity scenario, a highly irregular porous distribution (with broader time distribution of the crossing atoms), as shown in figure 28. We made the membrane with average pore size of 200 nm, and thickness of 1700 nm, which is thinner than our membranes.

A great number of particles (few tens of thousands) were emitted against the membrane; the ones that have returned back or have gone outside the model limits are considered frozen. We tracked the remaining particles until they reach the opposite membrane side.

In figure 28 we can see the path of each atom when the simulation is finished (a), in this particular example only two of them being able to cross the membrane, and the actual position of the particles while the simulation is still running (b).

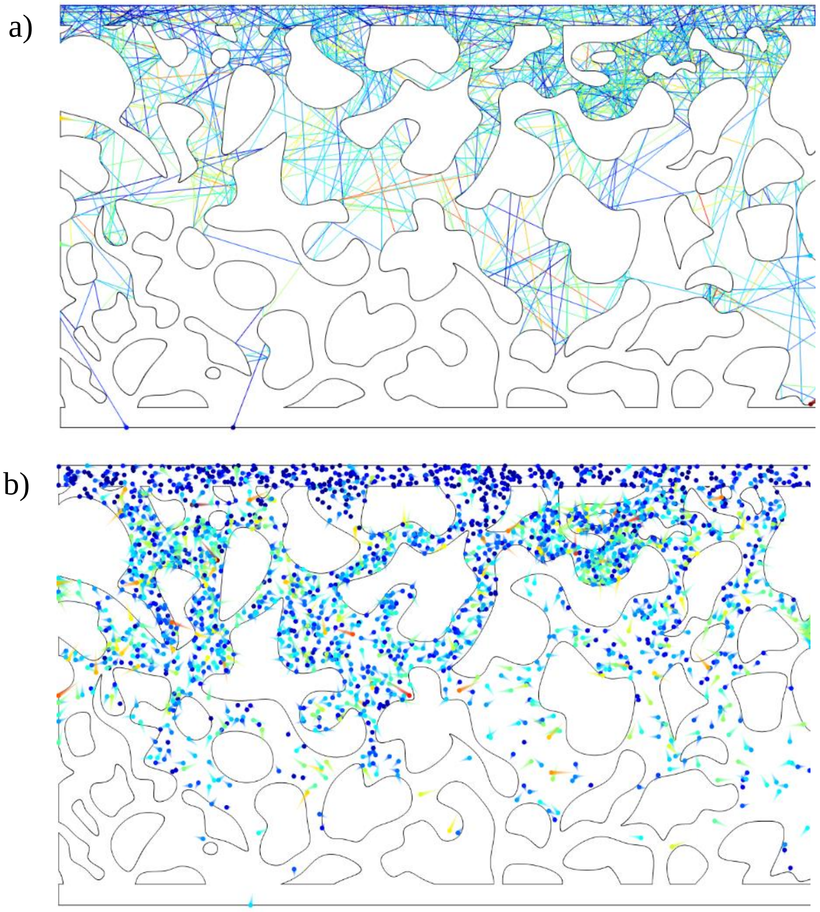

Figure 28: Plots from COMSOL simulations showing particles flowing through a porous membrane with 1700 nm thickness and an averaged pore side of 200 nm. The particles are initially emitted from the top boundary and collected in the bottom. a) Particle path after the simulation stops, for an initial number of particles of 500 and a total time of $10^{-7}\ s$. b) Particle position while the simulation is still running, for an initial number of particles of 50000 and a total time of $10^{-8}\ s$. The colours of the paths and particles are related to their velocity, in a rainbow scale, the blue ones are the slower and the red ones the faster.

This simulation allows computing the number of particles that crossed the membrane as a function of time. In this way, we can estimate the average time to cross the membrane. In figure 29 we present (blue dots) the time distribution of the particles crossing the membrane and a smoothed curve (red) of this data to better understand its behaviour since our data have poor statistics.

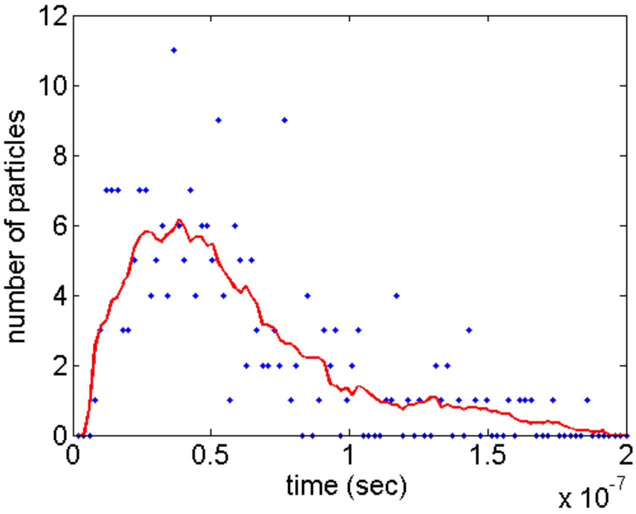

Figure 29: Number of particles arriving at the bottom of the membrane as a function of time. In blue, we show the results of the simulation; in red, a smooth curve following the blue points. The smooth curve peak is approximately at $3.5 \times 10^{-8}\ s$.

Now we have a more clear idea about the typical times that the gas atoms take to cross a porous membrane.

To know if an excited atom can cross the membrane without decaying by spontaneous emission, we will compare the typical lifetime of the resonant states with the travel time through a membrane. The first resonance states that decay by spontaneous emission have typical lifetimes of a few nanoseconds [48][49]. As an example, for two resonance states of Xe, $^3P_1$ (we intend to use it in our experiment) and $^1P_1$, the lifetimes were experimentally measured, being respectively $(3.79 \pm 1.12)\ \times 10^{-9}\ s$ and $(3.17 \pm 0.19)\ \times 10^{-9}\ s$ [50]. As seen, these values are at least one order of magnitude shorter than the average time for an atom to cross a 1700 nm membrane. So we can conclude that, if an excited atom enters the membrane, most likely it will decay inside, and if an atom gets excited inside the membrane it can only decay outside if it gets excited near the exit.

We should still note that we do not consider the lifetime modification induced by the Casimir cavity. As we also did not consider how deep inward the pores we can coat using the metal evaporation technique. So the membrane effective thickness will be different from the original thickness.

### 5.2.2. Electromagnetic dynamics through the pores

As the wavelengths used in the experiment (VUV region) are of the same order of magnitude than the pore size, we expect a wave-like behaviour. To have a clear idea about the light propagation through the pores, we made some simulations with the COMSOL software using classic electrodynamics. For simplicity and due to computer limitations, we performed the simulation again in two dimensions.

The membrane pores were represented by 3 small holes (in 2D) crossing an aluminium block. The remaining area of our simulation was filled with air. The electromagnetic waves were generated by electric oscillating dipoles whose frequency gives us the desired radiation wavelength. To simulate all radiation polarizations, the dipoles have perpendicular directions between each other.

First we put a set of dipoles in one side of the membrane and analysed the radiation crossing the pores. Then we vary the diameter (D) of the pores and their thickness (L). Some results are shown in figure 30.

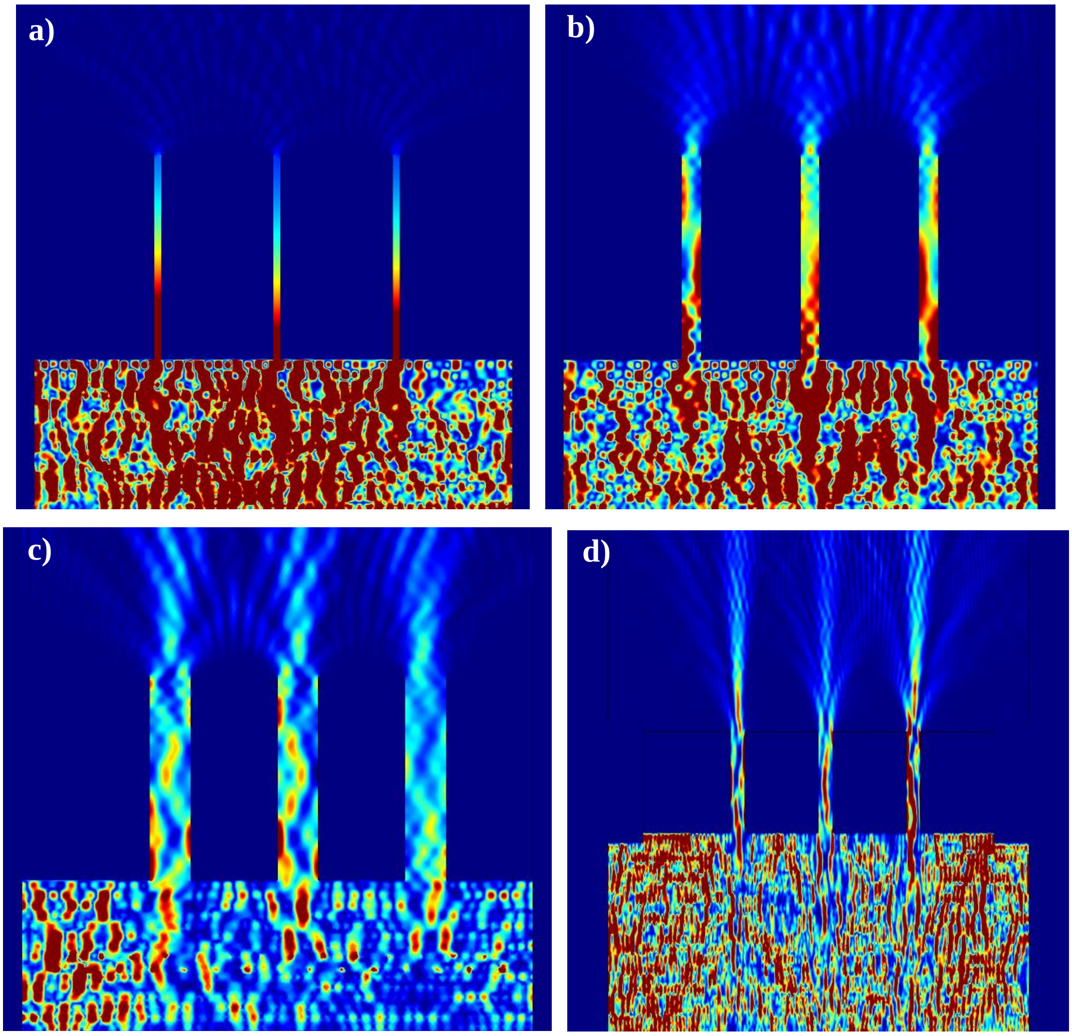

Figure 30: Two-dimensional view of the power per unit of area ($W/m^2$) of the radiation crossing the membrane for different membrane sizes: a) D = 75 nm and L = 2000 nm; b) D = 200 nm and L = 2000 nm; c) D = 400 nm and L = 2000 nm; d) D = 400 nm and L = 1000 nm. The radiation wavelength was 200 nm for all the plots. The colours are related to the power

intensity so that in the rainbow scale the red is the higher power and the blue the lower. The colour scale is similar in all the plots.

As expected, for pore diameters much smaller than the radiation wavelength there is a great attenuation, as we can see in figure 30 a). It is also evident the wave-like behaviour of the light for pore sizes with the same order of magnitude than the wavelength. For example, in figure 30 a) and b), we can see that the light has an interference pattern and comes out from the pores in all directions. In figure 30 c) and d), the immerging light has a behaviour more similar to a beam since the holes have already a size twice the wavelength. It is also clear that the shorter holes, shown in figure 30 d), allow more light to pass through them than the longer ones, shown in figure 30 c).

Subsequently we computed the radiation transmittance through the membrane as a function of the hole diameter. The radiation wavelength was fixed at 200 nm and we computed the total power collected at the membrane exit. The power transmittance is shown in figure 31. As expected the transmittance is higher for larger pores and almost zero for pore sizes smaller than half of the radiation wavelength.

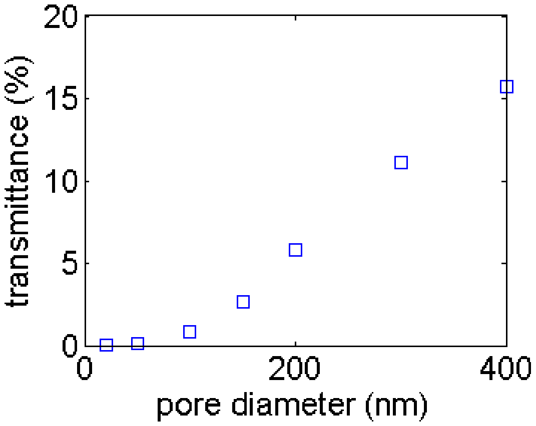

Figure 31: Radiation transmittance as a function of the pore diameter. The radiation wavelength is 200 nm and the pore thickness is 2000 nm.

To have a clear idea of the radiation propagation when emitted from inside the pores, we simulated the electric dipoles inside them. For that, we placed two dipoles in the centre of each pore, one with the same orientation of the pore walls (P1) and the other one with orientation perpendicular to the walls (P2).

First, we studied the differences in the dipole orientations and noticed that, for small diameters (L = 40 nm) the radiation is almost fully suppressed for P1 but not for P2. This behaviour was expected since the electric dipoles emit mostly in its perpendicular direction, thus for P1 the radiation is reflected in the walls and then suppressed (Casimir condition).

Next, we made several simulations varying the pore dimensions with the two internal dipoles (P1 and P2). Two examples of the results are shown in figure 32, where it is possible to note, in a) and b), that for larger D values there is much more radiation coming out of the largest holes, an evident effect of the suppressive influence of the cavities when they are shorter than the radiation wavelength.

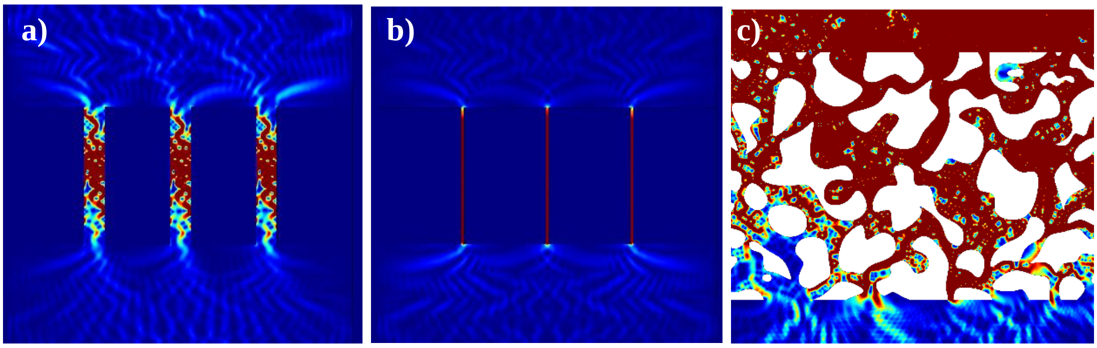

Figure 32: a) and b) two dimensional views of the power per unit of area ($W/m^2$) of the radiation emitted from inside the membrane for different membrane sizes: a) D = 300 nm and L = 2000 nm; b) D = 40 nm and L = 2000 nm. c) two dimensional view of the power per unit of area of the radiation emitted from the top against the membrane, with the same highly porous material used in section 5.2.1. The radiation wavelength is 200 nm for a) and b), and 100 nm for c). The colours in a rainbow scale, where the red is the higher power and the blue the lower. The colour scales of a) and b) are not the same as the scale of c).

We also made some simulations for the highly porous membrane model used in section 5.2.1 by varying the radiation wavelength. We noticed that, for shorter radiation wavelengths, the penetration in the membrane and its transmittance is higher. An example is shown in figure 32 c), where it is perceptible the light preferential paths and some zones where the light was mostly suppressed.

# 6. Results and discussion

## 6.1. Preliminary tests and calibration

Before we started our experiments it was necessary to perform some tests and calibrations, particularly of the MCs. These are described in the following sections.

### 6.1.1. Delay correction of the Nucleus multi-spectrum utility

After we've acquired some spectrum we noticed an annoying problem in the Nucleus multi-spectrum utility. When we started the MC driver at the same time that the Nucleus software we observed that the Nucleus always continued the acquisition (and generated new files) a few seconds after the MC stopped. The origin of the problem was a small (much less than 1 second) delay every time the program saved a file. We performed a test for different conditions and concluded that the delay was related with the file name length. We then operated the Nucleus so that it saved all the files with the same filename length and observed that the delay was always the same.

In order to solve this Nucleus feature, we improved our MATLAB code (SpeGen) so that it would take into account this delay and make the corrections.

### 6.1.2. Choice of the MCA counting window

Each pulse height distribution recorded by the Nucleus PCA has a considerable amount of noise which can attributed to several phenomena. Therefore, integrating the counts in all channels is not the best option. Instead we've used a window of channels which corresponds to the photon counts. In figure 33 there is an example of a typical pulse height distribution spectrum when the PMT is irradiated directly by the lamp. The prominent peak corresponds to the pulse amplitude distribution of typical photon counts which adopts the expected Gaussian distribution. To determine if the centroid of this distribution changes with the counting rating we've taken a set of spectra with distinct counting rates and fit a gauss function superimposed on a linear background to each one. Lastly, with the fitting output information we plot the variation of the Gaussian centroid as a function of its amplitude. The As result we've observed a very evident non variation, showing that we can use a fixed channel interval to analyse our spectrum. This interval goes from the channel 100 to the channel 240. This range was chosen, taking into account the centroid and FWHM of the gauss and also the shape of the background noise distribution.

In figure 33 a second structure at the right side of the gauss curve is also visible. This structure becomes similar to the main peak when the incident photon rate is increased. In such cases we noticed that the channel corresponding to the centroid of this peak is exactly the double of the main peak. This lead us to conclude that this second peak was generated when two photons reached the photocathode with a small time difference being the resulting primary charge doubled relatively to when only a single photon reaches the photocathode. The resulting output pulse is also doubled. We notice also that, when the incident photon rate is much greater, several peaks started to appear. The centroids channel of these peaks were integer multiples of the main peak. These peaks are almost impossible to distinguish since they overlap with each other and with a giant background noise. For this reason we will avoid working in such high rate conditions. This is possible since we can control the amount of light collected by closing the horizontal MC slits (which also increases its resolution).

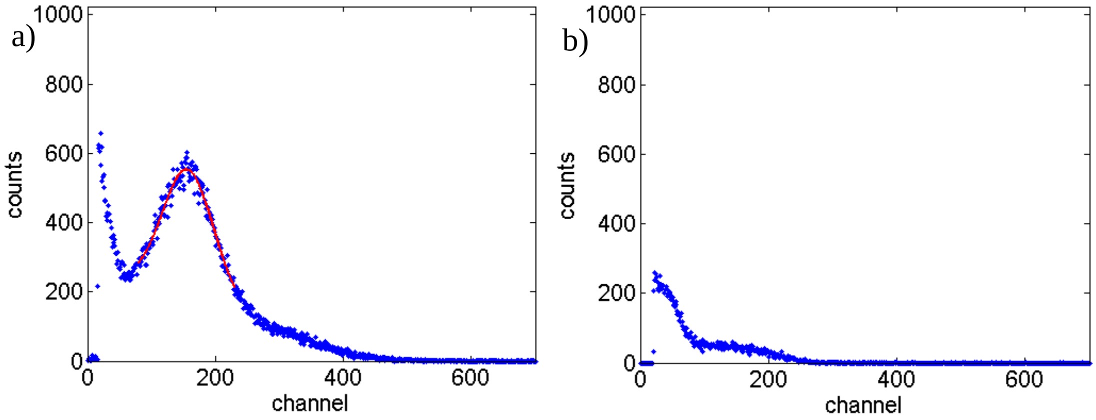

Figure 33: a) PMT pulse height distribution as recorded by the MCA when the PMT was irradiated with ~92 nm light. In blue, number of counts as a function of the channel and in red the fit of a gauss function superimposed on a linear background. Acquisition time 3 sec. b) PMT pulse height distribution recorded by the MCA without light irradiation; in blue, number of counts as a function of the channel. Acquisition time 3 sec.

In figure 33 we also plotted a typical MCA spectra recorded without PMT irradiation were a considerable amount of noise is visible, even in the channel window that we've selected (channel 100 to 240). This background is not subtracted since we are not interested in absolute values but only in relative ones and the pulse height distribution (related to the intensity[18] of the collected radiation) doesn't change its form due to the background (which is constant for all the wavelengths).

### 6.1.3. Light attenuation with the pressure

The wavelengths below 200 nm are strongly absorbed by the matter, including the air [51] and, to allow its transmission in a closed apparatus, it must be evacuated. This is the reason why this range of the electromagnetic spectrum is called Vacuum UV (VUV). At shorter wavelengths (until $\sim 150\,nm$) the main absorber present in the air is the oxygen, being possible to use nitrogen atmospheres to transmit these wavelengths. However for shorter wavelengths even nitrogen becomes an absorber.

To ensure that the vacuum achievable inside the MCs does not affect their functionality we've performed a simple test and measured the radiation attenuation across the MC optical path, as a function of the pressure inside the MC.

For this we've used MC2 (it has demonstrated to have the poorest vacuum quality) and assembled the PMT at the MC output flange and the deuterium lamp at the input, while evacuating the setup using $T_1$.

To measure the pressure inside the MC we've used a pirani and a penning vacuum gauges assembled directly in a third MC vacuum flange. These monochromators are equipped with 3 input/output flanges. Two of them are used in our measurements as input and output for the radiation. The third flange was not used in our main experiment and is only used when different geometrical MC configurations are necessary.

To figure the relative light intensity we've summed all the counts between the channels 100 and 220 of the pulse height distribution, without any background subtraction. To change the pressure inside the MC we've closed the vacuum pump valve for a while and, to achieve higher pressures, we slightly opened the air inlet valve (there is a valve embedded in the MC which connects directly with the atmospheric pressure). The wavelength was fixed at 170 nm and the two slits were adjusted to 45 μm. The light intensity as a function of the pressure inside the MC is shown in figure 34.

---

[18] Every time we refer to light intensity this is not an absolute quantity. Since in our experiment we are not interested in measure absolute values but only its variation with some other parameter, our light intensity is just a quantity proportional to the number of photons which the PMT collects.

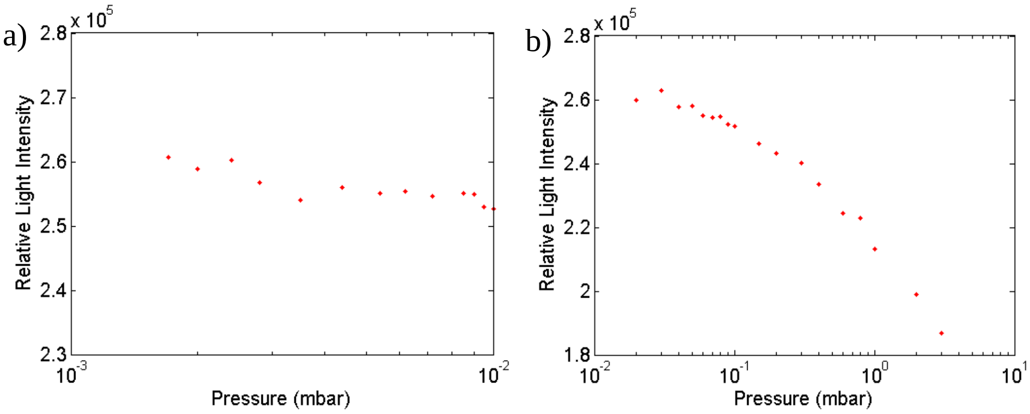

Figure 34: Relative light intensity as a function of the MC pressure, data recorded using: a) a penning vacuum gauge; b) a pirani vacuum gauge. These two tests are independent. Acquisition time of each spectrum = $15\ s$

We can now conclude that in fact there is some attenuation when the pressure inside the MC is increased. However it only happens at higher pressures, for lower pressures the variation is almost inexistent. For the pressures at which we will operate at (less than $2 \times 10^{-3}\ mbar$) the attenuation is negligible and thus we conclude that the residual air absorption in our system does not play an important role, at least for the wavelength that we've used in this measurement (170 nm).

It's important to refer that the vacuum gauges used are not perfectly calibrated and some of these measurements were done in the limits of their sensitivity range. These factors make the absolute values measured doubtful; however as we've used these same vacuum gauges in our main experiment, this study was enough to estimate the required vacuum (measured with these gauges) in order to minimize the light attenuation.

### 6.1.4. MCs calibration

For the calibration of the MC we've used the Lyman-alpha line of the deuterium whose theoretical value is 1215.31 Å [44] since we don't have the exact information relative to the other lines observed in the spectrum. As the reader may notice, this wavelength is outside of our PMT working range (160 - 650 nm). However we observed that, even with reduced quantum efficiency, the PMT was able to detect light under its lower limit. Then, for each of the MCs, we've assembled the lamp on their input flange and the PMT directly on the output flange. We then made a scan in a range were we would expect to find the 1215.31 Å resonant line. A typical spectrum (already offset corrected) obtained for MC1 is shown in figure 35. We can now compare our spectrum with the one provided in the ARC VUV Deuterium Source manual (figure 27) and conclude that our instrumentation is working accordingly with the manufacturer specifications.

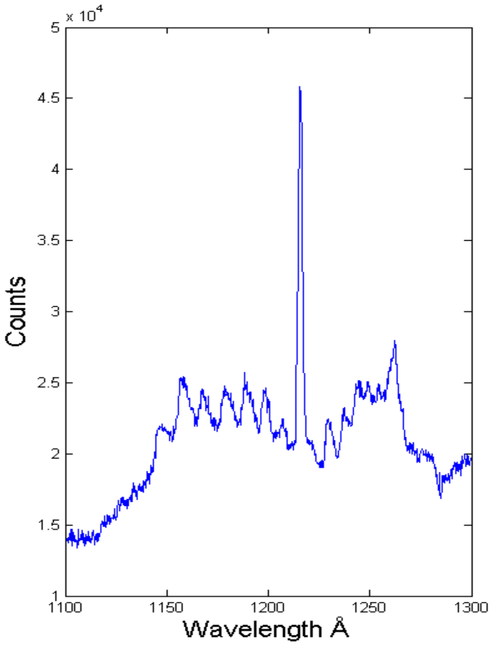

Figure 35: Deuterium lamp spectrum obtained by scanning the wavelength range from 1100 to 1300 Å with MC1. . Both horizontal slits were adjusted at 45 μm and the vertical ones at 3 mm. Acquisition time at each wavelenght $= 3\ s$. Scanning rate = 4 Å/min.

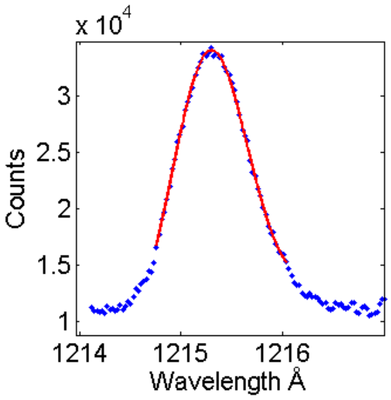

Figure 36: Spectrum obtained by scanning the wavelength range from 1100 to 1300 Å with MC1. Scanning rate of 0.5 Å/min. Acquisition time at each wavelength$= 3\ s$. Horizontal slits were adjusted at 35 μm and the vertical ones at 3 mm. The graphic represents the counts as a function of the wavelength. At blue the number of counts for each wavelength and at red a fit of a gauss function superimposed on a linear function. The centroid and FWMH are respectively ~1215.30 Å and ~0.86 Å which corresponds to an energy resolution of 0.07 %.

In order to accurately determine the offset of the monochromators, we made a new scan (for MC1 and for MC2) focused in the range where we found the Lyman-alpha line. This new scan had a slower scan rate and more data points per wavelength unit. Lastly we made a fit of a Gaussian plus a linear function to the Lyman-alpha peak. The fitting parameters allowed us to compute the MC offset and FHWM, figure36.

The MC1 driver allowed the automatic offset correction by inserting in the software a specific value; however for the MC2 driver the only solution is the operator to manually insert the desired wavelength taking in account the offset.

## 6.2. Experimental results and discussion

After calibrating all the instrumentation and confirming that the system is working properly we continued for the main experience.

We've used two membranes with pore diameter of 0.1 μm, one uncoated and the other coated with Aluminium. The membrane was evaporated four times in two perpendicular directions for two opposite 45º angles (relatively to the path of the evaporated Al). Taking into account the size of the pores, in order to avoid obstructing them, the thickness of each film was of 5 nm. This value was read from a plane surface orthogonal to the evaporation path, and at the same distance from the source as the membrane. We've only coated one side of the membrane, the less roughened. After the evaporation we've assembled the membrane with the coated side facing the MC2 light exit (which also corresponded to the gas inlet on the main chamber).

In all the spectra of this section, we've considered only the events between the channels 100 and 240 (from the Nucleus MCA pulse height distribution files). For each wavelength, the counts in these channels were summed, being this sum a point in the following spectra, which present the radiation intensity as a function of the wavelength. For some of the spectrums the acquisition time for each wavelength was longer than 1 second. In these cases the number of events was normalised to 1 second.

We start by studying the shifts in the atomic ground state using only the MC1 connected to the PMT, which analysed the radiation emitted from the main chamber. In our preliminary tests we observed that the PMT sensitivity starts to rise abruptly for wavelengths above 1500 nm and, since the MC upper wavelength limit is 5500 nm we have scanned the range going from 1500 nm to 5500 nm. In another preliminary test we've confirmed that if we closed the MC1 entrance the background was the same that when the main chamber was evacuated and the MC1 was open. Therefore we conclude that there is no radiation in the main chamber when it is in vacuum and that, in our measurements, we can consider as background the signal recorded when the MC1 entrance is closed.

We then made a set of scans for different conditions: 1) background scan: before the principal measurements with the MC1 entrance closed, measuring the signals from the PMT + MC1; 2) with Xe flowing through the uncoated membrane; 3) with Xe flowing through the Al-coated membrane; 4) with a greater Xe flow rate through the Al-coated membrane; 5) background scan, taken after the data taking, again with the MC1 entrance closed.

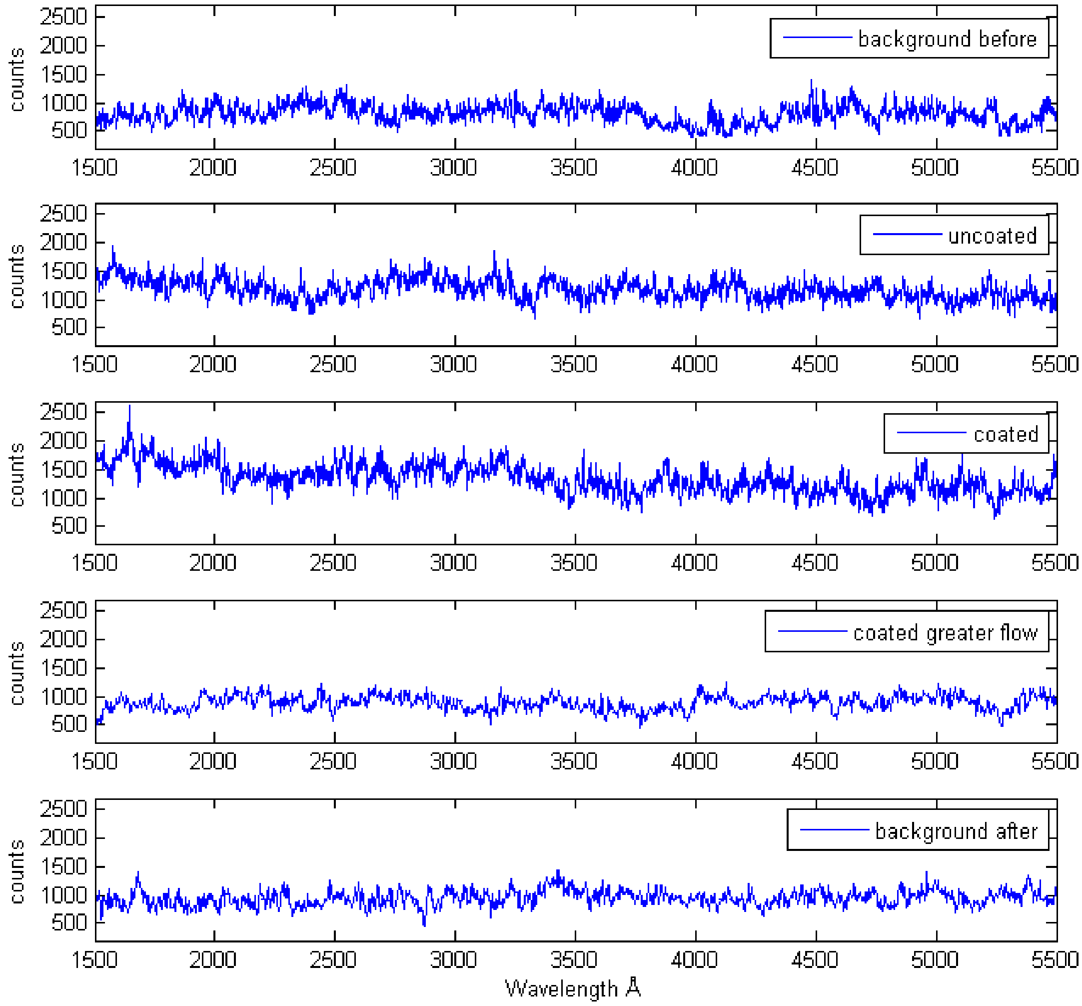

Figure 34: Photon intensity as a function of the wavelength for different conditions: 1) background at the beginning of the experiment – taken with the MC1 entrance closed; slits = 505 μm; scan rate = 100 Å/min; MCA acquisition time = 1 s. 2) scan with the uncoated membrane with Xe flowing; differential pressure of ~0.3 *mbar*; slits = 505 μm; scan rate = 100 Å/min; MCA acquisition time = 1 s. 3) scan with the Al-coated membrane with Xe flowing; differential pressure of ~0.3 *mbar*; slits = 505 μm; scan rate = 100 Å/min; MCA acquisition time = 1 s. 4) scan with the Al-coated membrane with higher Xe flowing; differential pressure of ~0.4 *mbar*;slits = 5005 μm; scan rate = 200 Å/min; MCA acquisition time = 1 s. 5) background at the end of the experiment; MC2 entrance closed; slits = 5005 μm; scan rate = 200 Å/min; MCA acquisition time = 1 s.

The results of these scans are plotted in figure 34. For each case the entrance and exit slits aperture was the same, for some of the measurements the slits aperture was larger to allow a greater light entrance, and for other cases the aperture was smaller to improve the resolution. For the cases when there was Xe flowing through the chamber, we controlled the flow by adjusting a needle valve (located at the gas inlet of the main chamber). The differential pressure between the two sides of the membrane allowed to estimate the gas flow through the membrane.

Since it's difficult to observe the differences between the individual plots of figure 34 we made a smooth curve to each spectrum and compared them in the same plot (figure 35). Without the smooth curve it would be visually very confuse to present all the data in the same plot.

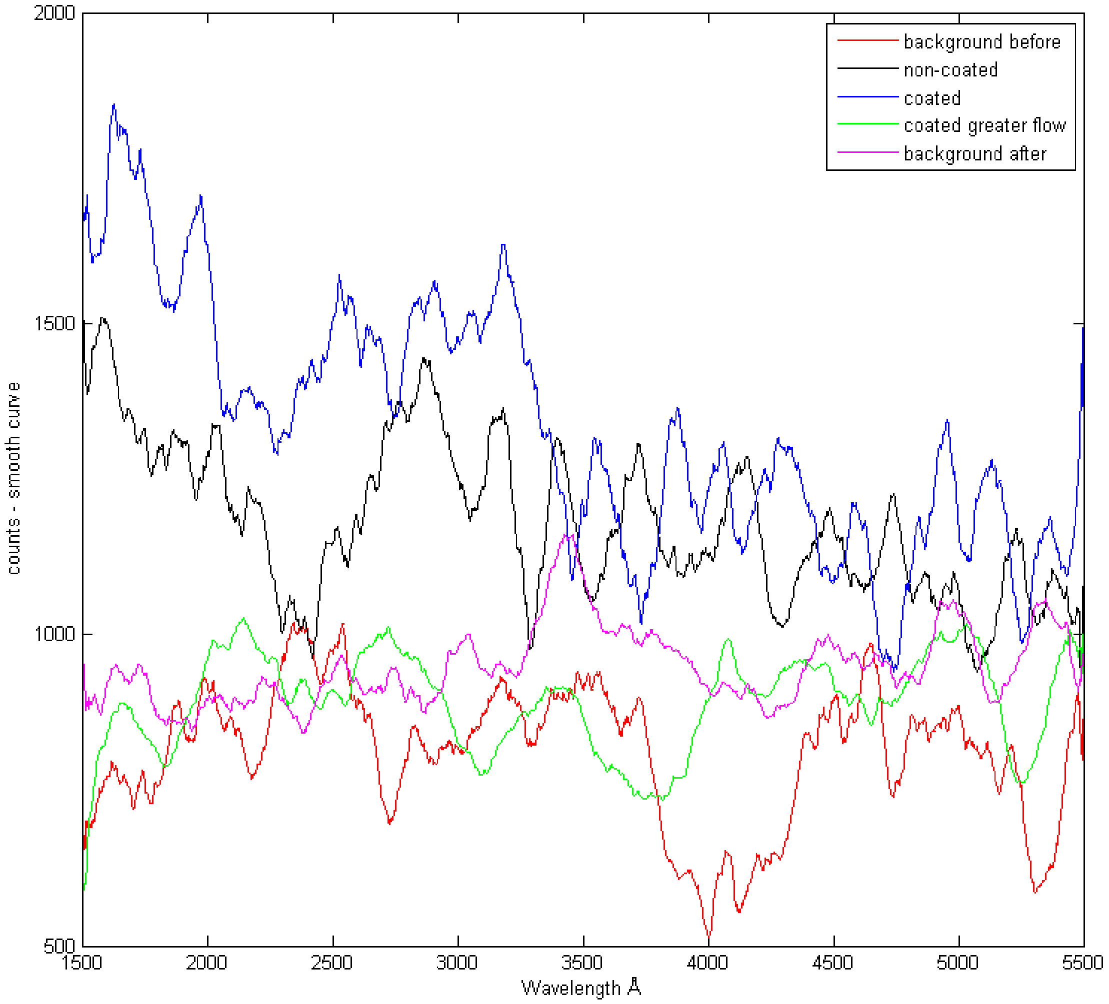

Figure 35: Smoothing of the curves presented in figure 34. The smoothing was the same for all the curves. The legends and axis have the same meaning as in figure 34.

We can see some interesting differences between the curves presented in figure 35. For the coated membrane it is possible to see a photon intensity greater at shorter wavelengths and, while for the uncoated membrane the same behaviour is present, it is not so noticeable. Moreover these two spectrum are globally slightly higher than the two background spectrums. However we made another scan were we’ve used the coated membrane but for a greater flow rate and greater slits aperture (coated greater flow series in figures 34 and 35) but in this we’ve recorded a photon intensity similar to the one of the background. This last test suggests that the difference in the two other scans can be attributed to a fluctuation of the instrumentation and not to the radiation detected by our PMT. Nevertheless the two first tests with Xe flowing are coherent with our proposals, since more radiation it was observed for the coated (for which the ZPF modes are more effectively suppressed) than for the uncoated membrane. However a more careful study is required in the future, since we cannot conclude for now if there was radiation emitted from the main chamber, or not.

In another measurement we’ve used the MC2 to irradiate the main chamber with a selected wavelength. The Xe is the noble gas which has the lowest energy resonance transition of the noble gases [45], which is an advantage for our purposes, since our PMT was designed for a relatively low energy range (160 - 650 nm). The lower resonance energy level of Xe is the $^3P_1$, whose transition energy relatively to the ground state is 8.43 eV ($\sim$147.1 nm), hence we used that transition. Unfortunately this transition wavelength is outside the PMT working range but, since we were able to perform spectroscopy measurements for wavelengths much lower (for example until 110 nm, figure 27 ) then, if there is enough radiation reaching the PMT, it could be possible to distinguish the Xe emission from the noise and to make a reliable spectroscopic analysis.

One of the methods proposed in section 4.1 suggests that if we excited the atoms with some characteristic wavelength, once inside the Casimir-cavity they could radiate and emit a lower wavelength that the one with which the atoms were excited. To study this effect we irradiated the Xe atoms outside of the membrane with using a wavelength of 147.1 nm (first resonance transition of Xe) and, then made the gas flow thought the nano-pores, while in other side of the membrane we analysed the radiation emitted using MC1. The resulting spectrum is shown in figure 36.

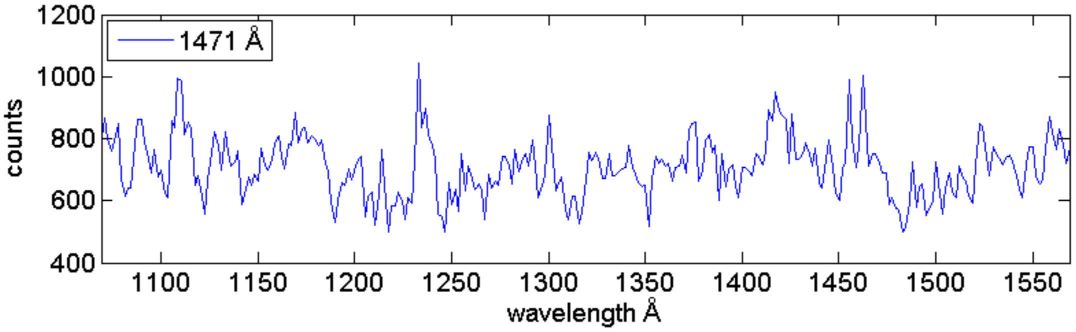

Figure 36: Spectrum recorded with MC1 when the main chamber was irradiated using photons with wavelength of 147.1 nm. The Al-coated membrane was inside the main chamber and Xe was flowing. The differential pressure on both sides of the membrane was $\sim 0.35\,mbar$; slits MC2 = 5005 μm; slits MC1 = 2005 μm; scan rate = 50 Å/min; MCA acquisition time = 2 s.

We cannot see in figure 36 the expected radiation emitted for wavelengths shorter than 147.1 nm, however we cannot also see the excitation wavelength (147.1 nm). This last observation suggests that system is not sensitive enough for this wavelength range. It is also possible that the wavelength emitted is shorter than the analysed range lower limit, which would be observed in the case a larger than expected ground state shift would occur.

We then proceeded to other method, also proposed in section 4.1.4, according to which if we irradiate the atoms with a wavelength greater than their characteristic transition (in this case 147.1 nm), they could be successfully excited if inside the Casimir cavity the (since the shift in the excited state would be greater than the shift in the ground state). Consecutively, when the atoms returned to the free space, they would emit their characteristic transition wavelength (in this case 147.1 nm), since the ZPF would re-energised its ground and exited states back to the normal energies. In our system we made three spectral analyses (using the MC1) for three different excitation wavelength ranges. The photon intensity distribution of the excitation beam has a Gaussian form with centroid at the wavelength inserted in the MC2 controller and with the width defined by the MC2 slits aperture. We regulated the entrance and exit slits of MC2 to 5.005 mm (the maximum slit aperture) since in this step it was required to irradiate as much as possible in wavelengths longer than 147.1 nm. The results for the three different irradiation wavelength ranges are shown in figures 37, 38 and 39.

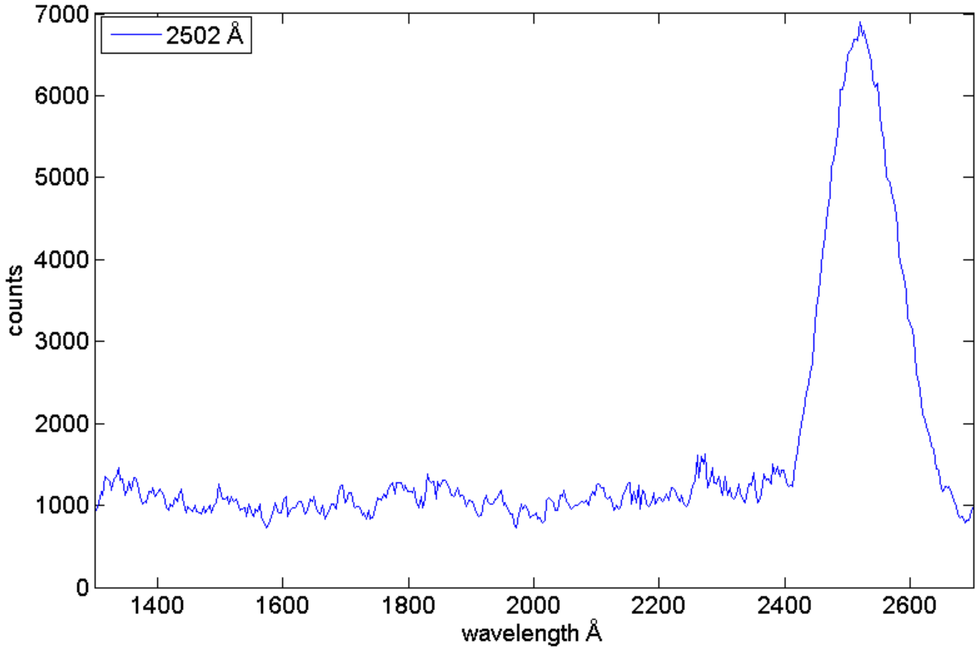

Figure 37: Spectrum recorded with MC1 when the Al-coated membrane was irradiated with 250.2 nm light and Xe flowing with a differential pressure of ~0.35 $mbar$;slits MC2 = 5005 μm; slits MC1 = 5005 μm; scan rate = 50 Å/min; MCA acquisition time = 1 s.

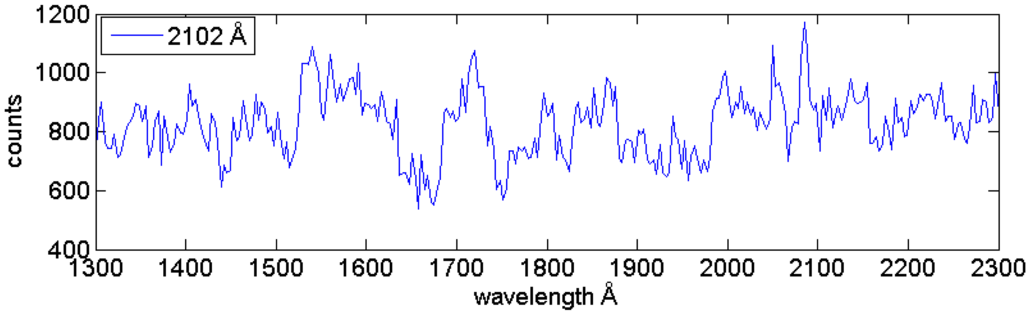

Figure 38: Spectrum recorded with MC1 when the Al-coated membrane was irradiated with 200.1 nm light and Xe flowing with a differential pressure of ~0.35 $mbar$; slits MC2 5005 μm; slits MC1 = 5005 μm; scan rate = 100 Å/min; MCA acquisition time = 2 s.

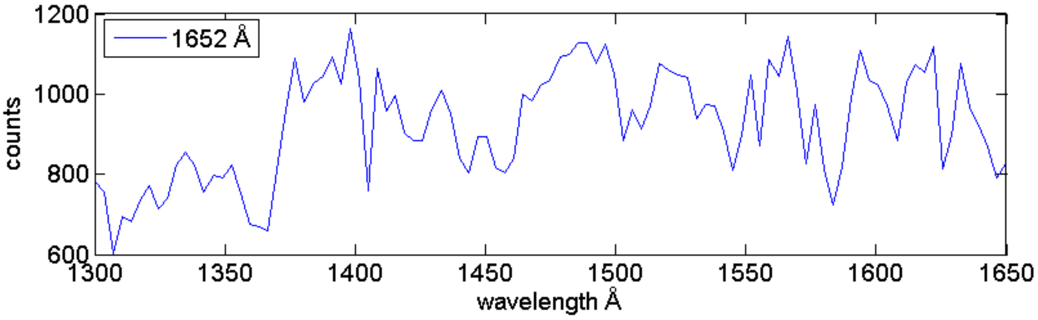

Figure 39: Spectrum recorded with MC1 when the Al-coated membrane was irradiated with 165.2 nm light and Xe flowing with a differential pressure of ~0.35 $mbar$; slits MC2 5005 µm; slits MC1 = 5005 µm; scan rate = 100 Å/min; MCA acquisition time = 2 s.

In the first measurement, figure 37, the excitation wavelength centred on 250.2 nm is perfectly visible. To have a clear idea of the width of the excitation wavelength distribution we made a fit to the peak at 250.2 nm, figure 37. The adjusted function was a gauss superimposed on a linear background, being the FWHM = 13.5 nm. Although the FWHM would probably change with the wavelength we used this value (13.5 nm) to estimate where should be the next excitation wavelength centroid so that it could be possible to distinguish it from the Xe characteristic wavelength (147.1 nm). In the next measurements, figures 38 and 39, the excitation wavelength is not visible; this can be due to the lower light source intensity at this wavelength or to the membrane reflectivity for this wavelength, amongst other possibilities. Despite that this observation seems to suggest that for wavelengths shorter than ~250 nm our system doesn't has enough luminosity or sensitivity; it may not be the case. In fact we may have the necessary condition but the Al-film can be reflecting more for longer wavelengths, because its reflectivity depends of the wavelength. However, as we've seen before in section 4.2.1 this behaviour seems to be constant in this wavelength range. Still other factors can influence, such as the light reflected by the stainless steel chamber walls whose reflectivity will be different that the one of Al . In figures 38 and 39 it is also not visible the Xe characteristic transition wavelength (147.1 nm), as it was expected by this method. However, as we have demonstrated in the past, our instrumentation can detect radiation in these wavelengths, and therefore our results are not due to the sensitivity of our system.

Anyway, the experimental work is at its very beginning and many studies are needed to understand our system and improve its performance, e.g. using a PMT with an $MgF_2$ window, reducing the PMT noise level, amongst other aspects. Nevertheless, under the present MSc work, we leave an experimental system fully operational.

# 7. Conclusions and future work

In this document we tried to present a complete study regarding the energy extraction from the ZPF. This subject was treated with classic mechanics, specifically the SED since it is more intuitive for our proposals than QM. However we also introduced a possible interpretation of this subject in the QM realm, giving to the reader some references for a more detailed study.

The SED was here introduced with focus on the H atom. Due to the gap in the literature concerning the behaviour of the atoms when immersed in a modified ZPF, we tried to create a model of this system by means of computational simulation. We then developed a code to simulate the motion of the electron in the H atom immersed in a one-dimensional free space ZPF, and with it we were able to replicate some results of Cole et al [35] demonstrating that the electron radius distribution in the SED realm seems to converge to the one predicted by QM. We therefore validated our code, which will be important for future applications. One of these applications would be to simulate the H atom immersed in a cavity-modified ZPF. However, apart other problems with this algorithm, we concluded that the ZPF generation method is not trusty for the small cavity case. Therefore we generated a full 3D ZPF using two different methods, one of them was first presented in the bibliography [32], and the other developed by us. Both of these methods had success in the simulations related with the classic harmonic oscillator in the free space. However for the harmonic oscillator immersed in a cavity-modified ZPF only the method developed by us has shown coherent results. Thus, considering the approximation of two harmonic oscillators in quadrature for the electron orbit in the H atom, we used our method to estimate the averaged radius variation with the cavity-modified ZPF. As initially suggested the ground state H atom will undergo a level shift when immersed in a cavity-modified ZPF. However we don't take into account possible cavity-induced perturbations in the electron radiated power. Lastly we developed an algorithm to integrate the electron motion in time in a full 3D model of the H atom. This algorithm is similar to the previous; however significant improvements were made such as the inclusion of the ZPF magnetic part. Although this new method is a trustier description of the reality, our computational sources limited us so that we could not simulate the free space case or accumulate enough statistic for the cavity case. During these computational developments we also made some discovers important for future improvements of the methods studied and developed in this work. In particular, we found that: the frequency window approximation seems to be not reliable for small boxes; the one-dimensional ZPF generation is ambiguous for the free space; and for small boxes it is more suitable to use the perfect box method for an accurate ZPF generation.

After these extensive computational investigations we proceeded to the experimental investigation, giving first to the reader a clear scheme of our method to extract energy from the ZPF. We discussed some hypothesis and corresponding topologies to adopt in the experimental apparatus. However, we cannot directly apply our previous computational SED-related simulations in our experiment, since the simulations were only developed as a proof of concept. Finally we made some assumptions necessary to implement this theory in the real word.

We projected and assembled an experimental apparatus capable of satisfying our conceptual ideas. Next we calibrated all the data acquisition instrumentation, developed software to analyse the data and made some tests which proven the functionality of our system.

Finally, we were able to study some of the methods proposed and discussed in the chapter 4. For the ground state shifts of Xe, despite some strange results, we didn't find any evidence of emitted radiation inside the main chamber. We essentially observed noise from the PMT + MC1 + data acquisition instrumentation. However, there could have been some radiation which was masked by the noise. Still, there is possibility that the radiation emitted is not in the studied ranges.

For the two excited state type methods, we also could not detect any radiation in the expected wavelengths, however we suspect that our system has poor sensitivity in these wavelengths. In fact, we've also made some tests were we didn't used Xe flowing or the membrane, only the two MC's face to face in vacuum. We've irradiated the chamber with a wavelength of147.1 nm (selected by MC2) while scanning the wavelengths using MC1 and failed to detect any radiation. We also noted that if we irradiated the PMT using longer wavelengths, as for example 155 nm, the detected light was so much that it saturates the PMT. Then, we conclude that our system is strongly limited in sensitivity for these wavelengths, principally by the PMT.

It is also important to notice that, although our computational investigations and theoretical assumptions were made for the electromagnetic vacuum at zero temperature, our research was made at room temperature, so in fact we cannot distinguish the vacuum from the thermal electromagnetic fluctuations.

### 7.1.1. Future work

First of all, an intensive theoretical investigation in the SED area, particularly for cavity enclosed atoms is needed. In the future we intend to make the same simulations we made here but with the inclusion of the modifications in the electron emitted power rate induced by the cavity boundaries. These simulations should be made using the real Coloumb potential and not the harmonic oscillator approximation. For that we intend to adapt our 3D H atom model to account for the cavity-modified damping constant. Hence, we need to run the code in a cluster, first for the free space in order to validate it, and then to run it for a small cavity. In the simulations area we also intend to continue the development of an algorithm (an adaptation of our 3D algorithm for the H atom) which accounts the atomic inner structure, in collaboration with Rodríguez.

Our investigation is pioneer and consequently our experimental apparatus was the first attempt to investigate the theoretical hypothesis. Thus, after this investigation, we intend to make a lot of improvements in our apparatus. The most obvious is the need of a PMT more sensible in the region of the first resonance transitions of the heavier noble gases (100-160 nm would be enough [45]). Alternatively other atoms with less energetic atomic transitions could be used as for example carbon which has a transition of 193.1 nm [52]. However, since these atoms don't appear isolated in the nature we would have to use for example a molecular gas (as for example $CF_4$) and dissociate them first, which is not difficult since the dissociation energies are usually less than the atomic energies. Therefore, the radiation wavelength inserted in the system will dissociate the molecules and also excite the resonance state.

Other important improvement is to minimize the light wastes by optical means. In the present experiment the exit beam area was adjusted to illuminate all the membrane area and nothing more, however depending of the radiation wavelength and the gas type, part of the beam is absorbed in the gas. Then, and without changing the main chamber geometry, the gas pressure should be low enough to allow a good membrane irradiation. For this, we will study in the next step of our experience the gas transparency for the used wavelengths as a function of the pressure. We believe that, in the hypothesis which we irradiate the membrane with a wavelength equal to the gas resonance line, the light is strongly attenuated, so the gas pressure will be determinant to ensure the membrane irradiation. However when the atoms are excited for resonance states they will release by spontaneous emission the same wavelength isotropically, so this effect also plays an important role in the calculation of the membrane illuminance. To maximize the collected light we intend to use a lens assembled inside the main chamber, close to the membrane gas outlet to focus the light emitted from this zone, in the MC1 entrance slit.

A possible improvement would the use of porous-membranes integrally constructed of metal. This represents an improvement since the actual coated film depth also influences the efficiency of the cavity in suppressing the ZPF modes, being better for higher depths. However this kind of materials is harder to obtain than the ones we used.

For future experiences with our experimental apparatus we intend to try others gases such as polyatomic gases. We expect that even vibrational molecular states will undergo level shifts when immersed in a modified ZPF, so instead of atomic transitions we can apply the same method for molecular gases where the energies to explore would be lower. As discussed in this work the dissociation and ionization energies can also undergo a level shift, so we intend to use in the future our equipment with other gases. Thus we can ionize/dissociate them before entering inside the cavity, where they recombine releasing a more energetic radiation that used to ionizing/dissociate them. In the case of using the molecular dissociation process, the energies used would also be lower (as the case of $H_2$), which represents an advantage when using our PMT.

Finally, we suggest a little test less dependent of the sensibility problems shown by our present system: the PMT can be directly assembled in the main chamber exit (where is now assembled the MC1 entrance), the main chamber entrance should be closed from any light source. Then, the Xe is made to flow through the Al-coated membrane at different rates, and perform acquisition of the PMT pulse counting, for each rate. Since for greater flows it is expected to have more atoms entering into the pores, the emitted radiation rate will also be greater. Without the MC1 and for a greater solid angle, the hypothetical collected radiation will be much more intense. This approach is similar to the one used in ref. [8] however, in our case, it will be for the UV-Visible range instead of IR range.

# 8. Annexes

## 8.1. Spherical Method introduction

In this section we will introduce what we called the "Spherical Method" to describe the ZPF. We will not explain the method or the algorithm in detail since it was already introduced and fully documented in other works [33][32].

This method produces a set of $N$ $\boldsymbol{k}$-vectors so that the correspondent frequencies sit between two limits, $\omega_{min}$ and $\omega_{max}$ (the same frequency window, $\Delta\omega$, we had introduced in the section 2.2.2). The frequency spacing is imposed by the $\Delta\omega$ and $N$. For each frequency a unique $\boldsymbol{k}$-vector is generated with a random uniformly distributed direction. This $\boldsymbol{k}$-vector and its random directions are easily generated using spherical coordinates. Consecutively each $\boldsymbol{k}$-vector can take any direction from the referential origin to any point of a sphere surface associated with the $\boldsymbol{k}$-vector correspondent frequency.

For each $\boldsymbol{k}$-vector 2 perpendicular vectors are also associated, they represent the two polarizations of the electric field. 2 random numbers uniformly distributed between 0 and $2\pi$ are then generated for each of these polarizations. Except the volume $V$, we have all the information needed to create a ZPF similar to the one described by equation 4. The magnetic component of the ZPF is generated from the electric one as mentioned before in section 2.2.1.

The spherical method aims to generate an approximated ZPF inside a cubic box for that in the $\boldsymbol{k}$-space the $\boldsymbol{k}$-vectors are distributed in a perfect cubic mesh. However, as we saw the spherical method leads with random directions in spherical coordinates, thus the $\boldsymbol{k}$-vectors don't have information about the cubic grid characteristic of a cubic box. Other discrepancy between this method and the reality is the number of $\boldsymbol{k}$-vectors for the same frequency. In this method there is only one $\boldsymbol{k}$-vector to each frequency but in reality there could be much more (since in a centred cubic mesh there are a lot of symmetric points whose distance to the referential origin are the same). Nevertheless it is claimed in ref. [32] that the spherical method is a good approximation when $N$ is great and $\Delta\omega$ is small in such way the distribution of $\boldsymbol{k}$-vectors is isotropic and similar to a spherical thin layer. If there are a lot of waves between near frequencies (as in a big V which is the free space approximation) then, as the $\boldsymbol{k}$-vectors density in $\boldsymbol{k}$-space is large, the information of the box bounds is less important and the cubic grid disposition of the ***k***-vectors becomes not important [32].

We have implemented this method developing a code in MATLAB to generate this ZPF. Making a simple representation, figure 37, of ***k***-vectors for a big $N$ we visually testify the isotropy of the generated ZPF ***k***-vectors.

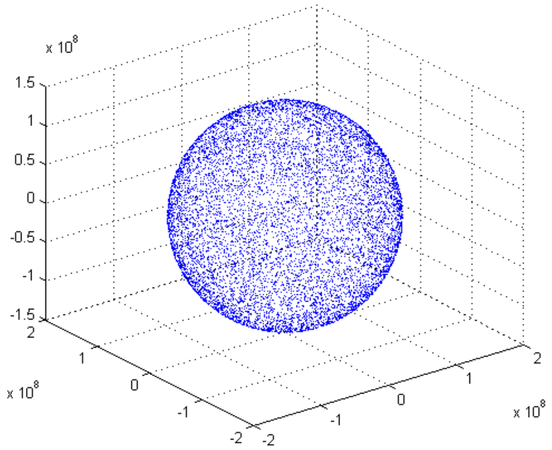

Figure 37: Three-dimensional representation of a set of ***k***-vectors generated with the spherical method, all axis are in SI wavenumber units ($m^{-1}$). The $\Delta\omega$ used is correspondent to the Bohr radius with $f = 400$ (the f number will be introduced in section 3.3). $N = 10036$ which is equivalent to a box of $L = 9 \times 10^{-6}\ m$.

Finally, for a specific N and $\Delta\omega$ it is possible to compute the correspondent $V$ [32] and thus include this value in the normalization factor $\left(\frac{1}{\sqrt{V}}\right)$.

## 8.2. $r_{eq}$ computation with the Spherical Method

In figure 38 we can see an example of a plot of the $P^{abs}$ computed by the Spherical Method and the theoretical curve of the $P^{abs}$ for the free space.

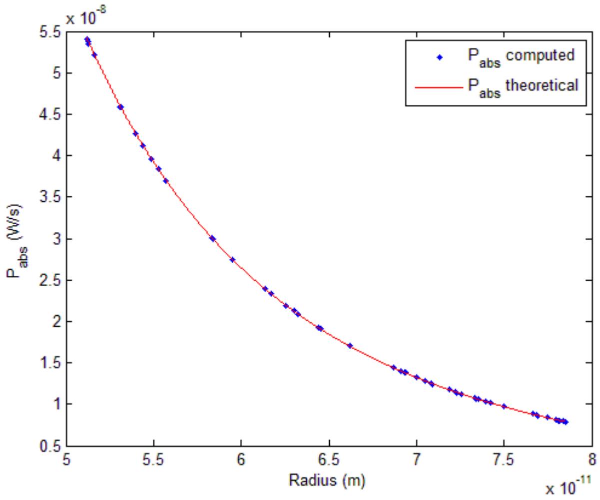

Figure 38: Computed $P^{abs}$ for different random radius and the theoretical curve of $P^{abs}$ for the free space, as given by the equation 16. The computation of the $P^{abs}$ was performed with *rs* = *50*, *ite* = *2*, f $= 400$, and $L = \sim 10 \times 10^{-5}\ m$

As we can see there is an incredible coincidence of the computed values and the analytical function. Next a non-robust fit was done with equation 22 resulting in $b = -4{,}5 \pm 0{,}003$ and $a = 2{,}65\ \times 10^{-54} \pm 2{,}00 \times 10^{-55}$ very concordant with analytic values (presented before in this section).

Finally we can compute the $r_{eq}$ finding the point of the interception between the fitted $P^{abs}$ and the theoretical $P^{rad}$ curve for the free space. In figure 39 we can see as an example this intersection for a box of $L = \sim 10 \times 10^{-5}\ m$.

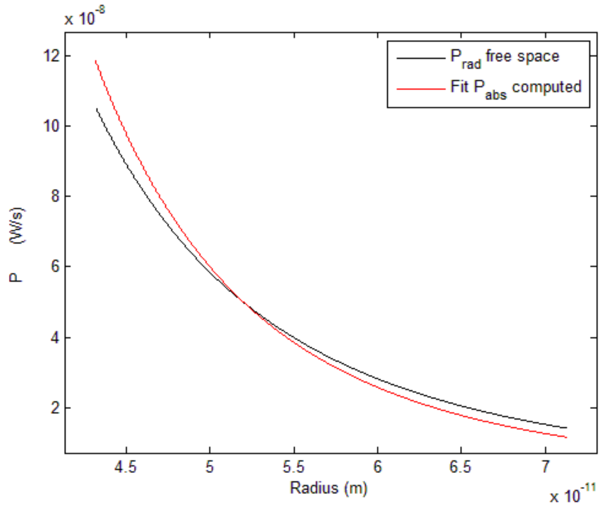

Figure 39: Fit of the computed $P^{abs}$ for different random radius and the theoretical curve of $P^{rad}$ to the free space. The $r_{eq}$ was found to be $5.2725 \times 10^{-11}\ m$. The computation of the $P^{abs}$ was performed with *rs = 50, int = 2,* $\mathrm{f} = 400$, and $L = \sim 10 \times 10^{-5}\ m$.

From figure 10 we can see that the interception point is aproximatetly the Bohr radius, this shows the success of the method and validates the code and algorithm at least for free space.

We then made the same simulation for a smaller box, with $L = \sim 5 \times 10^{-6}$. The results are showed in figure 40.

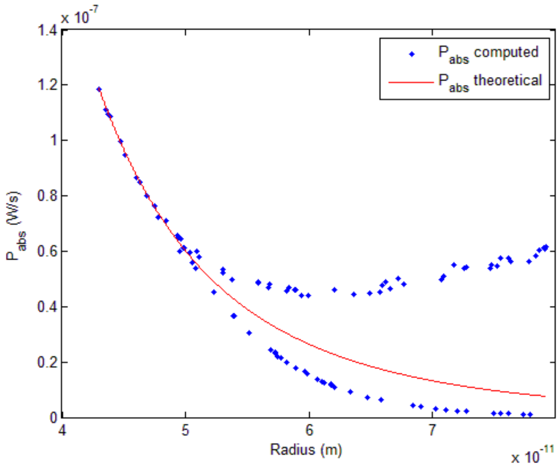

Figure 40: $P^{abs}$ computed as a function of radius and the theoretical curve to free space. To *rs = 150, int = 400,* $\mathrm{f} = 400$ and $L = \sim 5 \times 10^{-6}$.

As we can see from figure 40 there is a strange split of $P^{abs}$. This fact can indicates a failure of this method (spherical method) when the box dimensions are small. This is very probable since this method is only applicable in the limit of a great number of waves for that the geometrical $\boldsymbol{k}$-distribution in a cubic box is similar to the spherical $\boldsymbol{k}$-distribution generated in the Spherical Method.

# 9. References

[1] Valone, Thomas F. Practical Conversion of Zero-Point Energy: Feasibility Study of the Extraction of Zero-Point Energy from the Quantum Vacuum for the Performance of Useful Work. Integrity Research Institute, 2003.

[2] Davis, E. W., et al. "Review of experimental concepts for studying the quantum vacuum field." *Space Technology and Applications International Forum- Staif 2006*. Vol. 813. 2006.

[3] Ibison, Michael, and Bernhard Haisch. "Quantum and classical statistics of the electromagnetic zero-point field." *Physical Review A* 54.4 (1996): 2737.

[4] Rodriguez, Alejandro W., Federico Capasso, and Steven G. Johnson. "The Casimir effect in microstructured geometries." *Nature photonics* 5.4 (2011): 211-221.

[5] Cole, Daniel C., and Harold E. Puthoff. "Extracting energy and heat from the vacuum." *Physical Review E* 48.2 (1993): 1562.

[6] Boyer, Timothy H. "Random electrodynamics: The theory of classical electrodynamics with classical electromagnetic zero-point radiation." Physical Review D 11.4 (1975): 790.

[7] Puthoff, Harold E. "Ground state of hydrogen as a zero-point-fluctuation-determined state." Physical Review D 35.10 (1987): 3266.

[8] Dmitriyeva, Olga, and Garret Moddel. "Test of zero-point energy emission from gases flowing through Casimir cavities." *Physics Procedia* 38 (2012): 8-17.

[9] Boyer, Timothy H. "Retarded van der Waals forces at all distances derived from classical electrodynamics with classical electromagnetic zero-point radiation." *Physical Review A* 7.6 (1973): 1832.

[10] Boyer, Timothy H. "Van der Waals forces and zero-point energy for dielectric and permeable materials." *Physical Review A* 9.5 (1974): 2078.

[11] Jhe, Wonho. "Level shifts of simple atoms between parallel mirrors." *Physical Review A* 44.9 (1991): 5932.

[12] Zhu, Zhiying, and Hongwei Yu. "Modification of energy shifts of atoms by the presence of a boundary in a thermal bath and the Casimir-Polder force." *Physical Review A* 79.3 (2009): 032902.

[13] Lütken, C. A., and F. Ravndal. "Energy-level shifts in atoms between metallic planes." *Physical Review A* 31.4 (1985): 2082.

[14] Robinson, Edward J., Judah Levine, and Benjamin Bederson. "Metastable P 2 3 Rare-Gas Polarizabilities." *Physical Review* 146.1 (1966): 95.

[15] Ossicini, Stefano. "Interaction potential between rare-gas atoms and metal surfaces." *Physical Review B* 33.2 (1986): 873.

[16] Annett, James F., and P. M. Echenique. "van der Waals interaction between an atom and a surface at finite separations." *Physical Review B* 34.10 (1986): 6853.

[17] Casimir, H. B. G., and D. Polder. "The influence of retardation on the London-van der Waals forces." *Physical Review* 73.4 (1948): 360.

[18] Sandoghdar, V., et al. "Direct measurement of the van der Waals interaction between an atom and its images in a micron-sized cavity." *Physical review letters* 68.23 (1992): 3432.

[19] Sukenik, C. I., et al. "Measurement of the Casimir-Polder force." *Physical review letters* 70.5 (1993): 560.

[20] Brühl, Rüdiger, et al. "The van der Waals potential between metastable atoms and solid surfaces: Novel diffraction experiments vs. theory." *EPL (Europhysics Letters)* 59.3 (2002): 357.

[21] Grisenti, R. E., et al. "Determination of atom-surface van der Waals potentials from transmission-grating diffraction intensities." *Physical review letters* 83.9 (1999): 1755.

[22] Fouquet, P., P. K. Day, and G. Witte. "Metastable (2< sup> 3</sup>< i> S</i>) helium atom scattering from NiO (100) and Cu (100) surfaces." *Surface science* 400.1 (1998): 140-154.

[23] Fichet, Michèle, et al. "Exploring the van der Waals atom-surface attraction in the nanometric range." *EPL (Europhysics Letters)* 77.5 (2007): 54001.

[24] Heinzen, D. J., and M. S. Feld. "Vacuum radiative level shift and spontaneous-emission linewidth of an atom in an optical resonator." *Physical review letters* 59.23 (1987): 2623.

[25] Bloch, Daniel, and Martial Ducloy. "Atom-wall interaction." *Advances in atomic, molecular, and optical physics* 50 (2005): 91-154.

[26] Klimchitskaya, G. L., U. Mohideen, and V. M. Mostepanenko. "The Casimir force between real materials: experiment and theory." *Reviews of Modern Physics* 81.4 (2009): 1827.

[27] Rodriguez, David. "A classical, elementary approach to the foundations of Quantum Mechanics." *arXiv preprint arXiv:1112.3369* (2011).

[28] Rodriguez, David. "Orbital stability and the quantum atomic spectrum from Stochastic Electrodynamics." *arXiv preprint arXiv:1201.6168* (2012).

[29] Puthoff, Harold E., and S. R. Little. "Engineering the zero-point field and polarizable vacuum for interstellar flight." *arXiv preprint arXiv:1012.5264* (2010).

[30] Haisch, Bernard, and Garret Moddel. "Quantum vacuum energy extraction." U.S. Patent No. 7,379,286. 27 May 2008.

[31] Boyer, Timothy H. "Comments on Cole and Zou's Calculation of the Hydrogen Ground State in Classical Physics." *Foundations of Physics Letters* 16.6 (2003): 613-617.

[32] Huang, Wayne Cheng-Wei, and Herman Batelaan. "Dynamics Underlying the Gaussian Distribution of the Classical Harmonic Oscillator in Zero-Point Radiation." Journal of Computational Methods in Physics 2013 (2013).

[33] Huang, Wayne Cheng-Wei, and Herman Batelaan. "Quantized Excitation Spectrum of the Classical Harmonic Oscillator in Zero-Point Radiation." *arXiv preprint arXiv:1206.6891* (2012).

[34] de La Pena, Luis, and Ana Maria Cetto. *The quantum dice: an introduction to stochastic electrodynamics*. Vol. 75. Springer, 1995.

[35] Cole, Daniel C., and Yi Zou. "Quantum mechanical ground state of hydrogen obtained from classical electrodynamics." *Physics Letters A* 317.1 (2003): 14-20.

[36] Cole, Daniel C., and Yi Zou. "Simulation study of aspects of the classical hydrogen atom interacting with electromagnetic radiation: Circular orbits." Journal of Scientific Computing 20.1 (2004): 43-68.

[37] França, Humberto de Menezes, Trevor W. Marshall, and E. Santos. "Spontaneous emission in confined space according to stochastic electrodynamics." *Physical Review A* 45.9 (1992): 6436.

[38] Cavalleri, Giancarlo, et al. "Aquantitative assessment of stochastic electrodynamics with spin (SEDS): Physical principles and novel applications." *Frontiers of Physics in China* 5.1 (2010): 107-122.

[39] Nave, Carl R. "HyperPhysics. 2005." Georgia State University: http://hyperphysics. phy-astr. gsu. edu/hbase/hph. html# hph (2007).

[40] Silva, Roberto da, and Humberto M. França. "A estabilidade do átomo de hidrogênio segundo a eletrodinâmica estocástica." Revista Brasileira de Ensino de Física 24.1 (2002): 23-29.

[41] Heinzen, D. J., and M. S. Feld. "Vacuum radiative level shift and spontaneous-emission linewidth of an atom in an optical resonator." *Physical review letters* 59.23 (1987): 2623.

[42] Sanders A.W. “Optical Properties of Metallic Nanostructures.” *ProQuest* (2007).

[43] Rohsenow, Warren M., and Harry Y. Choi. *Heat, mass, and momentum transfer*. Prentice Hall, 1961.

[44] Herzberg, G. "Lamb Shift of the 1$^{2} $ S Ground State of Deuterium." *Proceedings of the Royal Society of London. Series A. Mathematical and Physical Sciences* 234.1199 (1956): 516-528.

[45] Leite, M. Salete SCP. "Radioluminescence of rare gases." *Portgal. Phys* 11 (1980): 53-73.

[46] Marquardt, Niels. "Introduction to the principles of vacuum physics." (1999).

[47] Clementi, E. T., and D-L_ Raimondi. "Atomic screening constants from SCF functions." *The Journal of Chemical Physics* 38.11 (1963): 2686-2689.

[48] Wilkinson, P. G. "Oscillator strengths of the resonance lines of the rare gases—I. Krypton." Journal of Quantitative Spectroscopy and Radiative Transfer 5.3 (1965): 503-510.

[49] Levi, Anthony Frederic John. Applied quantum mechanics. Cambridge University Press, 2006.

[50] Anderson, D. Kent. "Lifetimes of the (5 p 5 6 s) P 1 1 and P 1 3 States of Xenon." Physical Review 137.1A (1965): A21.

[51] Gorokhov E. V., ”Solar-Blind UV Flame Detector Based on Natural Diamond” Instruments and Experimental Techniques, 2008, Vol. 51, No. 2, pp. 280–283.

[52] Davis, Douglas, and Walter Braun. "Intense vacuum ultraviolet atomic line sources." *Applied optics* 7.10 (1968): 2071-2074.